Plasma Transferred Arc Coating

12

Abbreviations

CA-TIG	Cap active tungsten inert gas
CFD	Computational fluid dynamics
DC	Direct current
DE-GMAW	Double Electrode-GMAW
FC	Friction coefficient
FWHM	Full width at half maximum
GMAW	Gas Metal Arc Welding
GTAW	Gas tungsten arc welding
HAZ	Heat-affected zone
HE-PTA	High energy plasma transferred arc
HVF	High-volume fraction
HVOF	High-velocity oxy fuel
i.d.	Internal diameter
ISPC	International Symposium on Plasma Chemistry
ITSC	International Thermal Spray Conference
LHS	Left-Hand Side
LRM	Laser rapid manufacturing
MIG	Metal inert gas
MMC	Metal matrix composite
NTSC	National Thermal Spray Conference
PAC	Plasma arc cutting
PAW	Plasma arc welding
PC-TIG	Pulsed current tungsten inert gas
PP-AM	Pulsed plasma additive manufacturing
PTA	Plasma transferred arc
PWHT	Post weld heat treatment
RHS	Right-Hand Side
RT	Room temperature
SAW	Submerged arc welding
slm	Standard liters per minute
TBC	Thermal barrier coating
TIG	Tungsten inert gas
UTSC	United Thermal Spray Conference
YSZ	Yttria stabilized zirconia

12.1 Introduction

The plasma transferred arc (PTA) coating process was developed in the 1960s for the rebuilding and repair of worn parts and the hard facing of parts exposed to extreme abrasion and corrosion. Regular steel parts with an appropriate PTA coating can exhibit superior corrosion and wear-resistant behavior even compared to specialty alloys. The process is significantly different from other coating processes, including plasma spraying, as the surface of substrate is locally molten in the process creating a strong metallurgical bond between the molten coating material and the substrate if they are metallurgical compatibles.

The substrate, in most of the cases, serves as the anode for the transferred arc and only exceptionally as cathode to significantly limit the heat flux to the substrate and clean its surface. The powder to be deposited is introduced into the arc plasma through two or more orifices located on a ring surrounding the exit of the plasma torch nozzle. A further annular slot surrounding the powder injection ring provides the shield gas flow, necessary to avoid reaction of the molten metal with the environmental air. Once the molten metal cools and freezes, it creates a metal matrix composite coating, the mechanical and metallurgical properties of which can differ from those of the substrate or the coating material. The PTA process combines good control over the process with high deposition rates (typically 3–10 kg/h up to 20 kg/h) and good coating quality with practically no porosity and dilution of less than 7% (better than 5% have been reported). Feeding of multiple powders allows for a range of coating compositions to be obtained. Compared to other thermal spray processes, PTA has the major advantage that alloy formation can take place in the metal pool during the process, allowing for a wider range of combinations of metal compounds or metal matrix composite compositions than with any other spray deposition process.

In a variance of PTA coating technology, tungsten inert gas (TIG) welding, which is a free burning, un-constricted arc

M. I. Boulos et al. (ed.), *Thermal Spray Fundamentals*, https://doi.org/10.1007/978-3-030-70672-2_12

welding process, has also been used for coating applications with the filler material introduced in form of a wire. Because of the less stable arc attachment, the coating obtained has higher dilution values and larger heat affected zones compared to the standard PTA process. Deposition rates are of the order of 3 kg/h or less. Metal inert gas (MIG) welding using a wire as anode and the workpiece as the cathode is also a possible alternative to PTA. This has the advantage that oxide layers on light metals can be cleaned off before deposition. Deposition rates are in the order of 6–9 kg/h [Gebert and Bouaifi (2005)], and the dilution is somewhat less than with the TIG welding-coating process. Compared to other weld overlay processes, the coating quality is less sensitive to the torch–substrate distance.

This chapter is devoted to PTA used for coatings and hard facing, describing their basic design features, typical performance characteristics, and applications.

12.2 Basic Concept

12.2.1 General Remarks

The PTA process is closer to plasma arc welding than other plasma spray coating processes since the coating is fused to the substrate which is part of the electrical circuit serving in most of the cases serves as the anode to the transferred arc and only in a few cases as the cathode. The technique is comparable to tungsten inert gas (TIG) and metal inert gas (MIG) welding except for the feeding of the material to be deposited in the form of powder. It is also generally operated at higher power levels than TIG and MIG welding which gives rise to higher deposition rates of the order of tens of kg/h compared to 3 kg/h or less for TIG and 6 to 9 kg/h for MIG [Gebert and Bouaifi (2005)]. Laser cladding or laser weld deposition, on the other hand, involves the local melting of the substrate by a laser beam and the introduction of the cladding or welding material into the molten pool in form of powder or wire [Lewis and Schlienger (2000)]. As the cladding/coating material is injected into the molten pool, it either melts inflight or, as it enters the molten pool, bends with the pool material forming a metallurgical bond or remained is solid form, as in the case of ceramic powders, which disperses into the molten pool forming a metal matrix composite. The laser cladding/coating process, in spite of its high capital investment and low deposition rates comparable with TIG and MIG, is used advantageously, for high precision coating of small areas because of the ability to precisely control the movement of the laser beam. The same is true for electron beam overlaying, which is used for some special applications.

12.2.2 Plasma Transferred Arc Deposition

A schematic of the basic concept used in plasma transferred arc (PTA) deposition is illustrated in Fig. 12.1. The PTA torch consists of a hot, thoriated tungsten cathode surrounded by a water-cooled copper nozzle constricting the arc between the cathode and the workpiece. The plasma gas is introduced at the base of the cathode tip. The nozzle also acts as anode for the "pilot arc," i.e., there is a current supplied by a separate power supply flowing from the nozzle/pilot arc anode to the cathode. This pilot arc pre-ionizes the gap between the cathode and the workpiece and allows easy

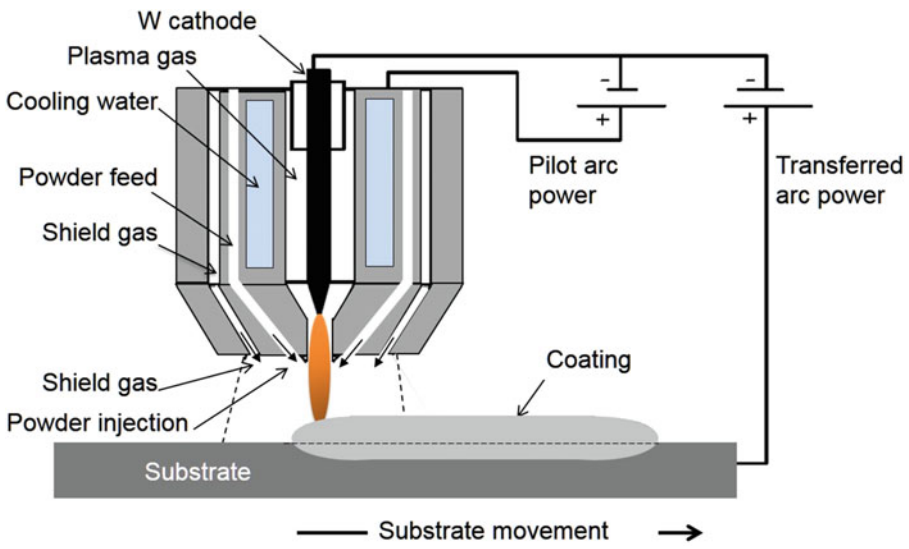

Fig. 12.1 Schematic of the basic concept of PTA deposition

establishment of the transferred arc and a good control of its arc current. The pilot arc further stabilizes the transferred arc when the plasma is cooled as a result of the injection of the feed material in the form of powder or wire and assures the correct positioning of the anode attachment and the area of powder deposition. The powder is introduced into the arc plasma through two or more orifices located on a ring surrounding the exit of the nozzle. A further annular slot surrounding the powder injection ring provides the shield gas flow, necessary to protect the molten metal from contact with the ambient air.

The coating is different from those obtained using other thermal spray coating processes because of the local melting of the substrate material at the anodic arc root attachment. The powder feed into the arc is also mostly melted, in-flight, and recovered into the molten pool of the substrate material with which it is mixed and alloyed. The consequence is that a good metallurgical bond or fusion bond is achieved between the coating and the substrate with a very low porosity. The heat penetration region and in particular the region where the coating material is mixed with the substrate material can change the properties of both the substrate and the coating. This mixing region is expressed in terms of the "dilution." As illustrated in Fig. 12.2, representing a cross section through a bead of deposited material mixed with the substrate material, the dilution (D) is defined as the ratio of the area where the substrate and coating materials are mixed (B), to the total area in which the coating material appears ($A + B$). That is:

$$D = B/(A + B)\% \tag{12.1}$$

The dilution is a major consideration when the functionality of the coating is evaluated. It is typically less than 5% for coatings of a thickness larger than 1 mm. It is also considerably lower than corresponding values obtained in TIG and MIG welding as well as submerged arc welding (SAW) in which dilution values of 15–40% are reached, requiring the deposition of several layers [Hallen et al. (1991)].

The PTA process combines good control over the process with high deposition rates (typically 3–10 kg/h, with up to 20 kg/h) and good coating quality with practically no porosity, and dilution of less than 7%. Compared to other thermal spray processes, PTA has the major advantage that alloy formation takes place in the molten metal pool during the process, provided the two metals/materials are compatible, allowing for a wider range of combinations of metal compounds or metal matrix composites compared to spray deposition process. According to DuMola and Heath (1997), PTA has the following advantages:

- High powder feed rates and deposition efficiencies (>95%).
- Tolerance to variations in feed powder quality, allowing for the use of low cost powders.
- Low porosity coatings (almost theoretical density),
- Thicker coatings in one pass can be achieved requiring fewer passes for part building.
- Metallurgical bond with strong adhesion to the substrate.
- Fine microstructure coating with smooth surfaces finish of the coating.
- Molten metal pool protected by a gas shield preventing oxidation during the deposition process.

PTA technology has, on the other hand, the following limitations:

- The requirement of a metallic substrate.
- Limitations on the substrate shape complexity.
- Dilution changing some of the coating and the substrate properties.
- High heat input into the substrate, requiring process modifications or active substrate cooling when smaller size substrates are coated.
- The process is not adapted to vertical surfaces due to the influence of gravity on the fluid flow and the coating geometry [Wilden et al. (2006)].
- Coatings are poorly adapted to complex substrate shapes including corners and grooves [Gatto et al. (2004)].
- Residual stresses can be rather high.
- Metallurgical compatibility between coating and substrate must be considered.

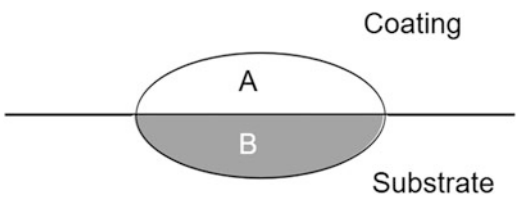

Fig. 12.2 Defining the dilution of a PTA coating

12.2.3 Arc Stabilization Mechanism

A wide range of plasma cutting/welding and coating torch designs and arc stabilization techniques have been developed and commercially used in industry. Most of these are covered by a large number of patents and proprietary information, which makes a detailed discussion of their design and performance rather limited [Colombo et al. (2011)]. Schematic representations of two typical PAC torch designs are given in Fig. 12.3. The design given in Fig. 12.3a shows a torch with a stick-type thoriated tungsten cathode with *axial* injection of the plasma forming gas. Because of the sensitivity of

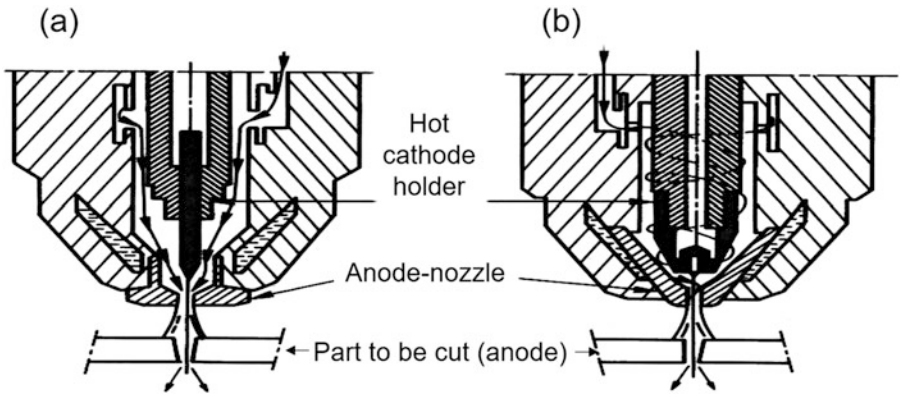

Fig. 12.3 Plasma cutting torches with (**a**) stick-type cathode, and axial plasma forming gas injection, and (**b**) button-type cathode, and vortex plasma forming gas. [Eliot (1991)]

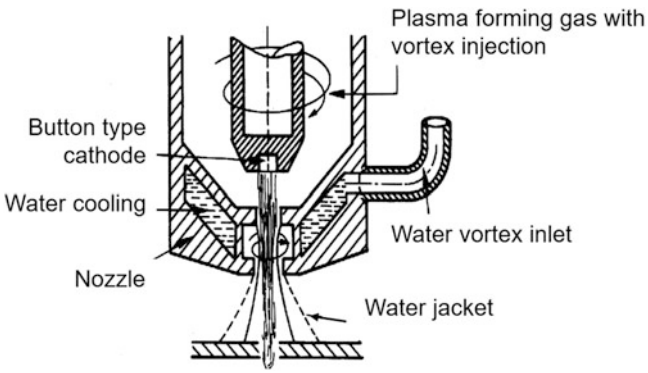

Fig. 12.4 Plasma cutting torch with button-type cathode, vortex plasma forming gas, and external water vortex [Eliot (1991)]

thoriated tungsten to the presence of oxygen in the plasma gas, these torches can only be used with non-oxidizing gases such as N_2 or Ar-H_2. The torch design given in Fig. 12.3b uses, on the other hand, a button-type cathode with *vortex* injection of the plasma-forming gas. The cathode is made in this case of either hafnium (Hf) or zirconium (Zr) for operation with air or oxygen or of thoriated tungsten for operation with non-oxidizing gases. In each of these torch designs, with axial or vortex arc stabilization, the arc is struck between the central electrode which acts as cathode, and the part to be cut which acts as anode, with currents up to 200 A or more.

In order to increase the arc constriction, decrease the fume emission, and reduce the thermally affected zone of the workpiece, a water vortex can also be added at the nozzle exit as shown schematically in Fig. 12.4. Due to additional energy losses in the water, this torch is operated at higher power levels. The arc current can vary between 15 and 640A but remains limited to 200A with Hf or Zr cathodes.

In order to keep the current density high, the nozzle orifice is kept as small as possible with its internal diameter directly dependent on the arc current. For example, with nitrogen as plasma gas, the i.d. of the cutting torch nozzle can be as small as 0.9 mm for arc currents up to 30 A, 1.2 mm for currents of 60 A, and 1.5 mm for 120 A. The gas flow rates are adjusted with the arc chamber pressure reaching up to sonic velocities in some cases.

12.2.4 Choice of Plasma Gas

The choice of the proper plasma gas for the operation of plasma arc cutting/welding or PTA deposition torches has a critical influence on the torch performance and the process economics. Gases best adapted for plasma cutting must have a high specific enthalpy and a high thermal conductivity, which is generally the case with diatomic gases such as H_2, N_2, and O_2. They should also have a high molecular mass in order to compensate for the significant drop in the specific mass of the gas at high temperatures. Pure argon is only used to start the arc, but never for cutting due to its relatively low specific enthalpy and thermal conductivity. Ar-H_2 mixtures are typically used with 20 vol. % H_2. The presence of hydrogen gives rise to a significant increase of the specific enthalpy and thermal conductivity of the mixture compared to that of pure argon. Hydrogen also helps to trap, at least partially, oxygen and provides neat and clean cutting grooves. N_2 is a good alternative plasma gas due to its high specific enthalpy and high thermal conductivity, which allows fast cutting/welding or coating without excessive oxide and slag formation. The thickness of the workpieces in this case is limited to 25–30 mm. The addition of H_2 to N_2 contributes to achieving better performance. It is to be noted, however, that nitrogen is susceptible to partial desolation in the molten metal in the cut or coating area, which could make it more difficult to weld the part in the same cut/deposited area. O_2 while commonly used in cutting operations is not acceptable in PTA deposition because of the formation of oxides which can blend into the coting structure.

The proper choice of the plasma gas has to be made taking also into account the electrode material since it will have an impact on the electrode lifetime. Zirconium or hafnium cathodes exhibit much higher wear, and consequently shorter lifetime, than that of the tungsten electrodes when working with non-oxidizing gases. Moreover, as the arc current is limited, by electrode design, to a 200–300A, the maximum power of the plasma torch will depend on the nature of the plasma gas used, which has a direct effect on the torch voltage.

12.3 Equipment Design and Operating Parameters

12.3.1 Basic Design Features

As illustrated in Fig. 12.5, the principal components of a typical PTA deposition installation are:

PTA torch is built around a central thoriated tungsten (2% ThO_2) cathode, typically 6–8 mm diameter (although smaller diameters have been used). The plasma gas is introduced into the torch at the base of the cathode and usually high purity argon or an argon-helium mixture. Downstream of the cathode tip is a water-cooled copper nozzle, typically 2–4 mm i.d., depending on the operating power of the torch. This nozzle serves as anode to the pilot arc and constricts/stabilizes the arc. Alignment of the cathode with the nozzle axis is of critical importance for obtaining quality coatings because a slight misalignment can lead to unstable or strongly asymmetric arcs, uneven powder heating, uncontrolled substrate heating, and reduced electrode life. Surrounding this nozzle is a ring with powder injection orifices. The powder is injected, depending on the process and material, either into the arc where it is fully melted or close to be melted or into the fringes of the arc to keep it only partially melted. In the first case, there is a secondary nozzle (sometimes called focusing nozzle) with a diameter of about double that of the constricting nozzle surrounding the powder injection ring. Torches that do not have this secondary nozzle have the ring surrounding the powder injection orifices at the same level as the constriction nozzle exit, and this arrangement results in powder injection into the fringes of the arc with less heating of the powders. The powder can also be fed directly into the molten metal pool by an extension of the tube that transports the powder beyond the secondary nozzle to a location close to the substrate surface. Surrounding this secondary nozzle is the ring introducing the shield gas which consists typically of argon with 5–7% hydrogen added and provides a curtain that protects the molten metal from reacting with the surrounding air atmosphere. Shield gas flow rates are multiples of the plasma gas flow rates. For deposition of metals that will react with hydrogen such as Ti or Al, pure argon can be used as shield gas.

Two independent power supplies, one for the pilot arc and the second for the transferred arc. Both power supplies are controlled in the constant current mode with relatively low open circuit voltages (<100 V). Alternately, a single two-stage DC power supply can also be used or a single DC power supply with the pilot arc anode connected to the positive power supply terminal via a resistor [Wassermann et al. (1978)]. A high-frequency starter unit in the pilot arc circuit facilitates the ignition of the pilot arc.

Closed-loop high-pressure cooling water supply for the torch; typically 6–8 l/min (1.5–2 USGPM) are required at a pressure of 0.45–0.6 MPa (66–88 psig). The heat from the

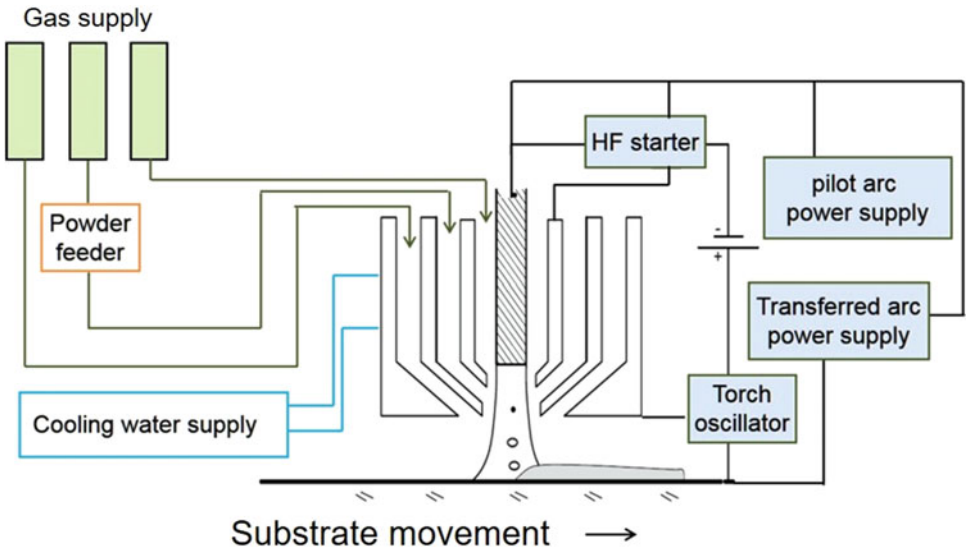

Fig. 12.5 Principal components of PTA deposition system

torch is removed by a heat exchanger which is connected to a chilled water circuit or city water circuit.

Gas supplies and flow controls for the plasma gas and the shield gas. Usually high purity argon is used as the plasma gas, helium being a possible addition. Ar/H_2 5–7 vol.% H_2 is used as the shield gas.

Powder feeder is essentially the same as in other thermal spray processes, although the use of larger size powders (typically 50–150 μm) may require some adjustments; multiple powder feeders are used for composite coatings. The powder is transported by a carrier gas (usually argon or argon with a few percent hydrogen) to the torch.

Control console allows for the selection and control of the pilot and arc currents setting, the gas flow rates, and the powder feed rates. The control console also houses the safety interlocks that prevent arc initiation under unsafe conditions such as in the absence of plasma gas or cooling water flow.

Mechanical systems as schematically illustrated in Fig. 12.6 allows for the translation of the substrate at speeds between 1 and 2 mm/s with potential additions of an oscillatory movement of the torch, at frequencies of 0.5–1.0 Hz and amplitude of about 10–40 mm in a direction perpendicular to that of the substrate motionwith. These are necessary in order to limit the local heat flux to the substrate and to produce flatter beads. The oscillation width needs to be adjusted such that the solidification of the molten metal pool during one oscillation is controlled and that exposure of a part of the molten metal pool to air outside the shield gas envelope is avoided [Hallen et al. (1992)]. A multi-axis robot could be needed for that purpose depending on the complexity of the shapes that can be coated.

Examples of the as sprayed texture of the coating obtained on different substrate shapes and configurations for a wide range of wear resistance applications are given in Fig. 12.7 [courtesy of 2017 DURM Verschleiss-Schutz GMBH].

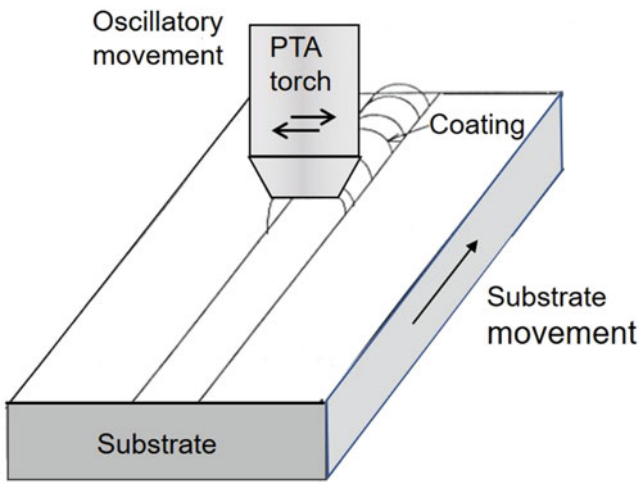

Fig. 12.6 Schematic of PTA deposition process

Depending on the size of the part to be coated and the associated power requirement, PTA deposition has been developed at the following three nominal production levels [DuMola and Heath (1997), Bouafi et al. (1996)]. The smallest level of operation of a PTA system is generally referred to as *micro-PTA* (μ-PTA). It is used at deposition rates of 0.1–2 kg/h for the coating of small parts or components with complex shapes, which can tolerate little heat [Shubert (1987), Shubert (1987), Lindland and Shubert (1988), Saltzmann et al. (1989), Saltzman and Sahoo (1991)]. The next size up is the *Regular PTA* used at deposition rates of 2–10 kg/h for the bulk of the PTA coating applications. The *High power PTA* is generally reserved for deposition rates between 10 and 20 kg/h (or even larger) for rapid coating of large surfaces or large components [Hallen et al. (1991), Hallen et al. (1992)]. A summary of the corresponding operating conditions for each of these operation levels are summarized in Table 12.1.

The properties of the coating obtained are dependent on the operating parameters and the material used. For regular PTA operation, the following represent typical values of system performance:

Bead thickness = 0.5–6 mm
Bead width = 2–40 mm, mostly around 10 mm
Coating thickness = 20 mm
Deposition efficiency = 95–98%
Dilution = 5–7%, possibly higher for coatings <1 mm thick

For micro-PTA (μ-PTA) bead widths can be as small as 0.5 mm, ranging up to 3 mm, with single pass bead thicknesses 0.5–3 mm, giving bead height to width ratios of 0.5–2 [Shubert et al. (1987)]. The dilution increases with the power. The fastest solidification and finest microstructure is obtained with the micro-PTA process.

While the majority of the equipment are automated, hand-held PTA torches are also frequently used [Kammer et al. (1991), Schreiber and Krefeld (2002)]. These are primarily used for smaller parts with complex shapes. There are also numerous modifications of the standard PTA equipments and processes principally to improve control over the powder heating, the heat flux to the substrate, and to adjust the process to specific substrate sizes and shapes. The loss of deposition material can occur through evaporation which makes the deposition of low boiling point materials such as zinc rather challenging. Homogenous condensation of the metal vapor leads to the formation of ultra-fine fume, which can be deposited on parts of the torch or on the substrate outside the bead. Avoiding injection of the powder into the center of the arc as well as using larger size particles (>60 μm), and increasing the shield gas flow rate, and the

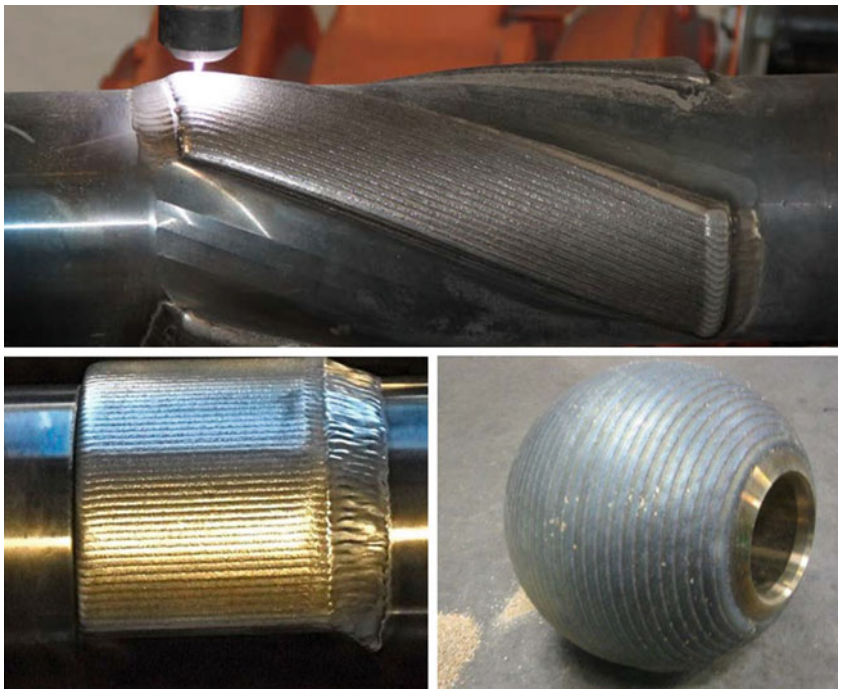

Fig. 12.7 Photographs of typical PTA process applications [2017 DURM Verschleiss-Schutz GMBH]

Table 12.1 Summary of operating conditions for different PTA scales of operation

Operating parameter	Micro-PTA (μ-PTA)	Regular PTA	High power PTA
Pilot arc current (A)	–	50–100	50–100
Pilot arc voltage (V)	–	40	40
Transferred arc current (A)	5 to 50	100–300	200–400
Transferred arc voltage (V)	20	40	40
Nozzle diameter (mm)	1–2	2–4	2–4
Torch-to-substrate dist. (mm)	5–10	10–20	15–20
Plasma gas flow rate (slm)	0.4–1.4 Ar	2–10 Ar or Ar/He	3–10 Ar or Ar/He
Shield gas flow rate (slm)	10–24 Ar or Ar + 5–7%H_2	10–40 Ar or Ar + 5–7%H_2	10–50 Ar + 5–7%H_2
Carrier gas flow rate Ar (slm)	1–3.5 Ar	1–20 Ar or Ar + 5%H_2	5–20 Ar or Ar + 5%H_2
Powder feed rate (kg/h)	0.1–2	2–10	10–20
Powder particle size (μm)	20–100	60–200	60–200
Translation speed (mm/s)	2–3.5	1–2	1–4
Oscillation frequency (Hz)	Non	0.5	0.3–1.0
Amplitude of oscillation (mm)	Non	10–20	20–40

torch-to-substrate distance can minimize the problem of the fumes.

Typical examples of commercially available PTA torches are given in Fig. 12.8 and Fig. 12.9. These vary in the details of the design configurations, power rating, and usable range of powder feed rate. These operate at pilot arc currents up to 30 A and maximum transferred arc currents up to 300 A and an open circuit voltage of 100 V DC. They vary in their duty cycle between 35% and 60% depending on the arc current. Examples of the torches shown in Fig. 12.9, by Durum GMBH, are given for a handheld torch (Fig. 12.9a) and machine-mounted, automatic or semi-automatic torches (Fig. 12.9b, c). Not included in the figure is the Durum PT-200i-80ID torch specially designed for deposition of internal surfaces with a minimum diameter of 80 mm with a maximum current rating of 200 A and powder feed rate up to 50 g/min. It should be noted that the given powder feed rate values are material and powder density defendant.

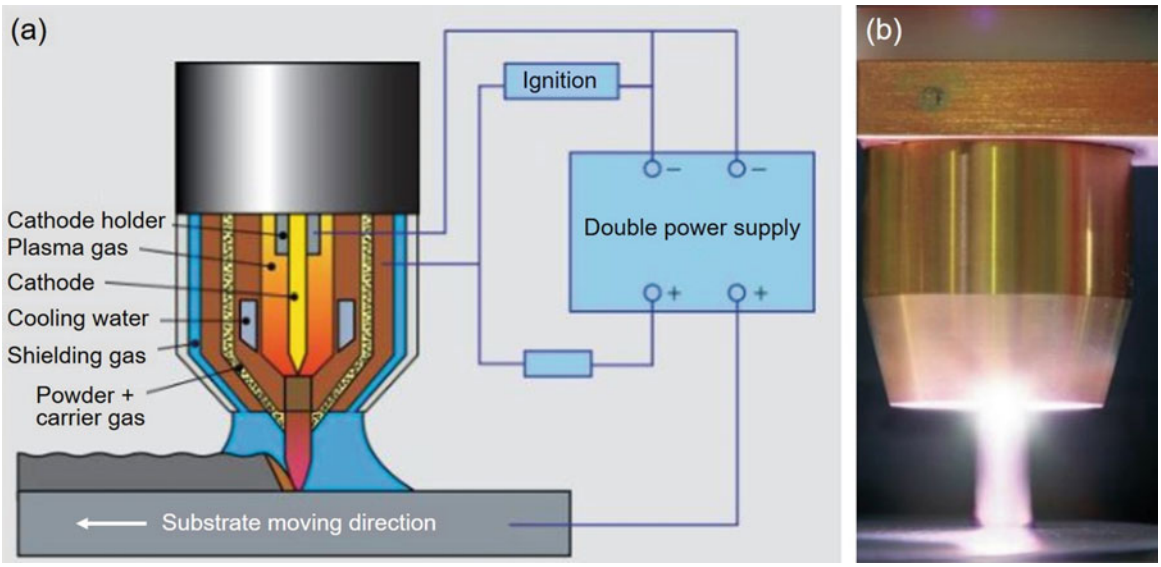

Fig. 12.8 (**a**) Schematic and (**b**) photograph of PTA welding/over laying plasma torch by Castelin Eutectic Corp. [www.eutectic.com]

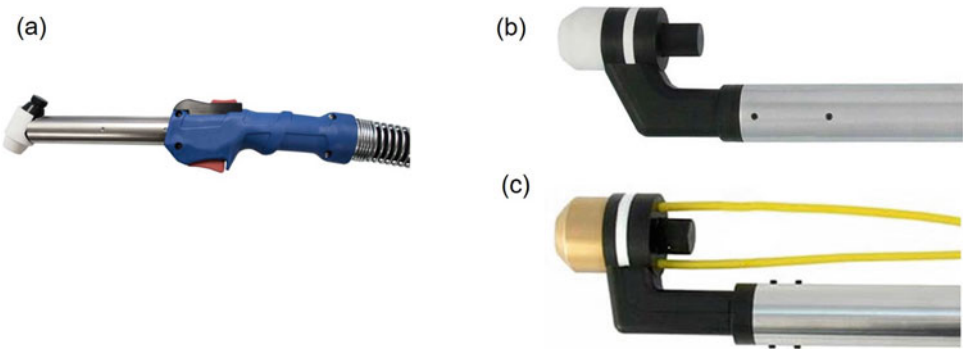

Fig. 12.9 Photograph of PTA Durmat Torches (**a**) PT-150 M manual, handheld torch, 150A, 30 g/min; (**b**) PT-300 AUT machine torch, 280 A, 75 g/min; (**c**) PT-400 machine torch 300 A, 100 g/min. [2017 DURM Verschleiss-Schutz GMBH]

12.3.2 Effect of Process Parameter Changes on Coating Properties

The primary qcuantities that are of concern are:

- Bead thickness and width
- Deposition rate, efficiency, and dilution
- Adhesion
- Functional performance such as hardness, porosity, defect density, and resistance to cracking

The functional performance parameters are usually addressed through the selection of the powder to be deposited, though they can also be influenced by the process parameters such as:

- Pilot arc and transferred arc currents
- Plasma gas, powder gas, and shield gas flow rates
- Powder feed rate
- Torch substrate distance
- Substrate translation and oscillation velocities

In the following, a brief discussion is presented on the influence of each of the principal process parameters.

12.3.2.1 Pilot Arc Current

The pilot current has little effect on the coating quality if all other parameters remain unchanged. However, it is mainly beneficial for the stability of the transferred arc and can in certain cases be used to provide added particle heating when the transferred arc current has to be reduced because of the sensitivity of the substrate to excessive heating. This condition is encountered when coating low melting point substrates or when dilution needs to be minimized, e.g., in thin coatings. The condition of high pilot arc current and low

transferred arc current approaches the situation of a plasma spray process.

12.3.2.2 Transferred Arc Current

Increasing the transferred arc current has the strongest effect on the substrate heating, the arc diameter, the plasma velocity, the heating and melting of the powder, and the movement in the molten metal pool. It also increases dilution, adhesion, bead width, and deposition efficiency, and lowers porosity, but *decreases* bead thickness, and may also reduce hardness as a consequence of increased dilution. In the case of hard surfacing involving the deposition of carbide powders for enhanced wearer resistance, high currents may lead to the partial decomposition or dissolution of the carbide phase, reducing the wear resistance. On the other hand, too low currents may lead to incomplete melting of the powder.

Typical results reported by Wang et al (2002) on the use of a microplasma PTA deposition system for free form fabrication are given in Figs. 12.10, 12.11, and 12.12 in terms of deposit bead width and thickness as function of the arc current, powder feed rate, and substrate displacement speed, respectively. The torch-to-substrate distance in this case was 3 mm, plasma gas flow rate 0.4 slm, powder gas flow rate 3.5 slm, and shield gas flow rate 10 slm.

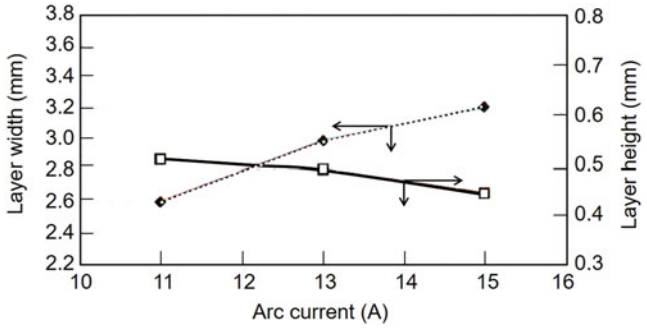

Fig. 12.10 Measured dependencies of bead width and thickness on arc current for powder feed rate of 2.3 g/min and substrate displacement speed of 0.52 mm/s [Wang et al. (2002)]

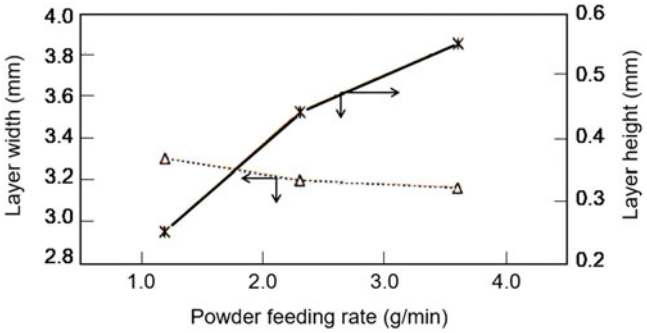

Fig. 12.11 Measured dependencies of bead width and thickness on powder feed rate for an arc current of 15 A and substrate displacement speed of 0.52 mm/s [Wang et al. (2002)]

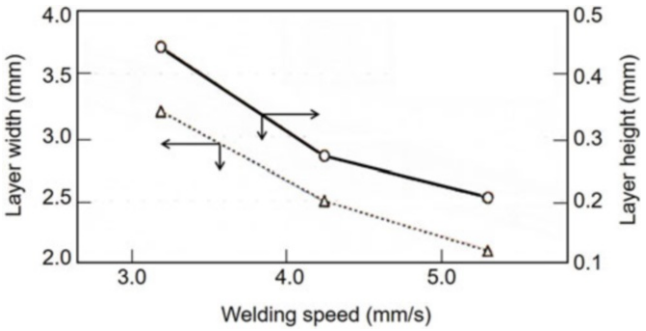

Fig. 12.12 Measured dependencies of bead width and thickness on substrate displacement speed for powder feed rate of 2.3 g/min and arc current of 15 A [Wang et al. (2002)]

12.3.2.3 Torch-to-Substrate Distance

Increasing the torch-to-substrate distance, gives rise to an increase of the arc voltage for the same current and consequently the increase of the total arc power. This would result in a corresponding, though not proportional, increase of energy transmitted to the substrate. The reverse effect is to be expected, however, on the gas velocity which decreases with the increase of the torch-to-substrate distance giving rise to a reduction of the movement of the molten metal pool and of pool dilution. The latter effect is stronger at higher arc currents. At a substrate distance of 20 mm, an increase in current from 150 A to 250 A can be balanced by an increase in powder feed rate from 6 kg/h to 10 kg/h, keeping the dilution below 10%. At a substrate distance of 15 mm, the dilution will increase with the increase of the arc current even with the increase in powder feed rate [Hallen et al. (1991)].

12.3.2.4 Plasma Gas Flow Rate

Increasing the plasma gas flow rate results in an increase of the arc width, and plasma velocity, as well as the movement in the molten metal pool. It can also result in increased heating of the substrate and increased dilution [Hallen et al. (1991), Deuis et al. (1998)]. The effect is dependent on the arc current and the traverse speed. At high heat transfer and substrate melting rates, the higher plasma gas flow rate can push the molten material toward the sides and cause turbulence and increase dilution in the molten metal pool.

12.3.2.5 Powder Feed Rate

Increasing the powder feed rate reduces the dilution, increases bead thickness, but reduces deposition efficiency. Too high powder feed rates for a given current will eventually lead to incomplete melting of the powder. Typical results by Wang et al (2002) on the effect of power feed rate on the width and height of the deposited bead is given in Fig. 12.11.

12.3.2.6 Substrate Material Properties

The nature of the substrate material has an influence on the arc voltage for a given arc current and consequently on the heat flux to the substrate. For cooled substrates, the substrate heat flux increases with the increase of the substrate thermal conductivity, while for an uncooled substrate, the heat flux increases with the increase of heat capacity of the substrate.

12.3.2.7 Substrate Motion

An increase in the translation velocity of the substrate will generally reduce dilution. The reverse effect has also been reported by Lakshminarayanan et al. (2008). It also can result in a finer microstructure in high power PTA deposition due to faster solidification of the molten metal [Hallen et al. (1992)]. At the optimal translation speed, the arc attachment is in front of the molten metal pool. Excessively high speeds will result in reduced fusion bonding, while too slow speeds will give rise to increased porosity [Hallen et al. (1992)]. The oscillation width needs to be adjusted such that the solidification of the molten metal pool during one oscillation is controlled or that exposure of a part of the molten metal pool to air outside the shield gas envelope is avoided. Typically, oscillation widths remain below 40 mm [Hallen et al. (1992)]. Experimental data by Wang et al (2002) obtained using a microplasma PTA system given in Fig. 12.12 show a steady decrease of both width and high of the deposited bead with the increase of the speed of the substrate displacement.

Special attention should be given to the dilution values in the bead because of their direct impact on the functional properties of the coating. While low dilution values improve the wear resistance of the coating, they are usually accompanied by low fusion values, i.e., small areas where a metallurgical bond is obtained. DuPont (1998) presents a correlation of the "fusion factor," i.e., the width of the dilution region over the width of the bead in a coating cross section, as function of the ratio of powder feed rate to arc power as parameter. They report a strong drop off of the fusion factor at a certain value of the ratio of the metal powder feed rate to the arc power, i.e., if the power is insufficient to melt all of the powder. A drop in the deposition efficiency usually accompanies the drop of the fusion factor. While these data were obtained for plasma arc weld overlays (no pilot arc), a similar effect can be expected for PTA coatings.

A study of the effect of the arc current, powder feed rate, and powder gas flow rate on dilution was reported by [Hallen et al. (1991)]. Typical results given in Fig. 12.13 were obtained for a workpiece St-37, 300 × 100 × 30 mm, coated using a torch-to-substrate distance of 20 mm, translation speed of 1.3 mm/s, amplitude of oscillation of 40 mm at an average oscillation speed of 1.8 mm/s, and plasma gas flow rate of 10 slm (Ar), with varying powder feed rates (6–12 kg/h) and transport gas flow rates (1–4 slm Ar). The results show

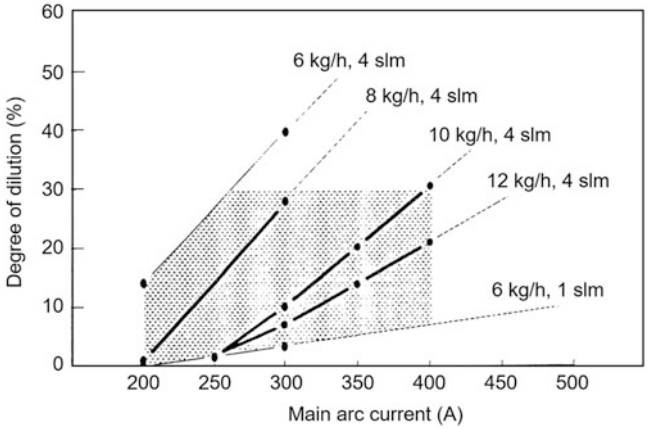

Fig. 12.13 Degree of dilution as function of arc current, powder feed rate, and powder gas flow rate. Workpiece St-37, 300 × 100 × 30 mm, plasma gas = 10 slm (Ar), amplitude of oscillation = 40 mm, oscillation speed = 1.8 mm/s, translation speed =1.38 mm/s, torch-to-substrate distance = 20 mm. [Hallen et al. (1991)]

Table 12.2 Effect of process parameters on coating properties, (+) for positive impact and (–) for negative impact [Ducos (1985)]

	I_{pilot}	I_{arc}	m_{powder}	m_{gas}	$v_{travers}$
Bead width	-	++	-		-
Thickness	+	-	++		--
Deposition efficiency		+	--		
Surface		+++	-		-
Dilution	-	+++	---	++/--	--
Hardness	+	---	+++	++	++

a steady increase of dilution with the increase of the arc current. As expected, however, the dilution drops with the increase of the powder feed rate and the powder transport gas flow rate. A discussion of operating parameter influences on dilution using a response surface analysis is presented by Lakshminarayanan et al. (2008).

[Just et al. (2010)] reported higher hardness at lower currents, faster cooling, lower dilution, higher impact resistance, but not necessarily better wear because of less bonding between the carbide and the matrix. A summary of the effect of process parameters compiled by Ducos (1985) is given in Table 12.2.

12.3.3 Process Modifications and Adaptations

The principal process modifications other than the adjustments of process parameters for high deposition rate, high power PTA, or low deposition rate micro PTA, or for adjustments for a specific coating/substrate combination, are:

- Limiting the use of the pilot arc to the arc ignition stage of operation.

- Special powder injection to avoid too overheating of the powder or substrate.
- Operating with nitrogen for surface nitriding.
- Operation of the transferred arc in reverse polarity for surface cleaning of the substrate, especially those with thin and impervious oxide layers such as Al or Mg.
- Modulating the plasma gas flow and/or the arc current, or torch design modification to affect the heat transfer to the substrate.
- Increasing the energy density at low total energies for high-velocity, small-area depositions (high energy PTA).
- Combining tape casting with PTA for complex shape coatings.
- Combining PTA with MIG or laser welding processes.

12.3.3.1 Limiting the Use of the Pilot Arc to Arc Ignition

An example of zero pilot arc current deposition (except for arc starting) in a micro-PTA deposition process is described by Wang et al. (2003) for the production of 3D free-standing parts. A transferred arc current of 10–15 A was used to deposit a 2–3 mm wide, 0.45–0.55 mm high bead with a "tool steel" powder feed rate of 2.3 g/min (0.138 kg/h). Deposition parameters were 3 mm standoff distance, plasma gas flow rate = 0.4 slm (Ar), carrier gas flow rate = 3.5 slm (Ar), shield gas flow rate = 10 slm (Ar), and substrate translation speed of 188 mm/min. Tungsten carbide powder was added with a second powder feeder, and the substrate was preheated to reduce the time for melting. Good control over the arc length was important for getting a uniform product.

12.3.3.2 Variation of Powder Feed Rate

To avoid overheating of the powders, e.g., carbides leading to their dissolution, powder injection can be limited to the fringes of the arc or directly into the molten metal pool through extended powder feeding tube [DuMola and Heath (1997), Bouaifi et al. (1996, 1997)]. Bouaifi (1997) describes the coating of industrial knife-edges with a chrome-vanadium steel, with the addition of vanadium carbide made using a separate powder feeder into the molten metal pool. The approach allowed for the increase of the VC particle loading fraction in the coating to 70 vol. %. Deposition parameters were arc current = 160–230 A, powder mass feed rate = 1.5–5.5 kg/h, and a translation velocity 0.67–2.5 mm/s. Some edges had to be ground after the coating deposition.

12.3.3.3 Nitriding of Coating

Efforts were made to increase the coating hardness through online nitriding resulting from carrying out the deposition process in a nitrogen atmosphere. Bouaifi et al. (2001) describe experiments for the deposition of Fe-Cr-V-C alloys with the addition of nitrogen to the plasma gas (Ar) and the use of pure nitrogen as powder and shield gases. Problems were encountered with nitrogen in the plasma gas since for volume concentrations above 50–70% of N_2 the arc became unstable. The stronger constriction of the arc also led to increased fume formation and shorter electrode lifetimes, as well as reduced coating adhesion at the bead edges. While the nitrogen content in the shield gas did not influence the coating properties notably, the use of 33 vol.% nitrogen in the plasma gas significantly increased the wear resistance of some the alloys deposited which contained up to 0.28 wt% nitrogen. A similar experiment is reported by Bach and Zühlsdorf (1999) using plasma weld deposition in a chamber with a nitrogen atmosphere. At 1 atm pressure in the chamber and 10 vol.% N_2 in the plasma gas, nitrogen incorporation into a Cr-Ni steel of up to 0.37 wt. % could be achieved. Increasing the chamber pressure reduced the nitrogen content and led to material evaporation and fume formation.

In an attempt to further increase the nitrogen content of the coating, Wang et al. (2009) pretreated the base metal alloy (7005 Al alloy) by depositing a TiN/Ni composite coatings on it using high-speed jet electroplating, followed by a PTA scanning process. The parts produced had a rapidly solidified microstructure consisting of uniformly distributed TiN phase and fine Al_2Ni_3 intermetallic phases. The microhardness was about HV 852 which is seven times higher than that of the Al alloy substrate. The friction coefficient for PTA scanning treated specimen was 0.25 which is significantly lower than 0.35 for TiN/Ni composite coating. The corrosion resistance of the composite coating was also significantly improved.

12.3.3.4 Modulation of Deposition Parameters

Modulation of the plasma gas flow rate or of the arc current has been the subject of numerous investigations for specialized PTA coating applications. Plasma gas modulation at frequencies between 1 and 5 Hz with an amplitude of 1–3 slm (Ar) was successfully used by Ebert et al. (2009) for the improvement of the dispersion of heavy WC particles in a Co-Alloy PTA coating containing 40 vol. % WC. The arc current in this case was 95 A, powder gas flow rate 2 slm (Ar), shield gas 10 slm (Ar), and traverse velocity of 1.67 mm/s.

Arc current modulation was used by Shubert (1987) in a micro-PTA application in which a bead is deposited as thin as 0.5 mm, with a bead height to width ratio that could be varied between 0.5 and 2 and with a ratio of bead width to substrate width of 0.5–1. An "auxiliary" current of 4–15 A is used for the arc on which high current pulses of 0.4 s duration, with a 25% duty cycle are superimposed to yield a time-averaged current between 12 and 40 A. The deposition rate was between 0.3 and 0.5 kg/h and the translation speed between 2.3 and 3.5 mm/s. This process has been applied in particular

to the refurbishing of gas turbine parts [Shubert (1987), Lindland and Shubert (1988)]. Saltzmann et al. (1989) describe the refurbishing of super-alloy parts in gas turbines with average currents of 3–20 A and with 10–40 ms long high current pulses during which the weld pool is created, while it is allowed to solidify during the low current time. The quick solidification times lead to very fine grain structure in the deposits. Very short torch-to-substrate distances are used (5–10 mm for currents from 10–50 A). The powder is delivered into the weld pool through an external feed tube.

A similar approach of pulsing the arc current was also used for the reduction of workpiece distortion for a near net-shaped application in which a stellite-6 coating was deposited on steel with an intermediate Ni alloy coating using a pulsed plasma weld coating technique [Matthes and Alaluss (1996)]. The amount of transferred arc current was periodically varied between a base current value and a pulse current value, and the effect of the current values and the duty cycle of the pulsed current investigated. Three passes were used to reach the required thickness of 8 mm. The dilution was found to be increasing with the arithmetic mean of the arc current, and with the increase of the ratio of base current to pulse current, as well as with the increase in duty cycle. All these factors influenced the heat input into the substrate, which are generally responsible not only for the dilution of the coating but also the workpiece distortion and reduction of its hardness. It was generally reported that current modulation was effective for the preparation of good coatings on small near net-shaped parts with a minimum distortion of the substrate material. D'Oliveira et al. (2005) evaluated the effect of pulsed current on a high carbon cobalt alloy deposited by PTA on carbon steel and stainless steel.

Razal Rose et al. (2012) pointed out metallurgical advantages of pulsed current tungsten inert gas welding (PC-TIG) frequently reported in literature. These include reduced width of heat-affected zone and refinement of the grain size of fusion zone. In their paper, an attempt was made to establish an empirical relationship to predict tensile strength of the PC-TIG welded AZ61A magnesium alloy by incorporating process parameters such as pulse current, base current, pulse frequency, and pulse on time. Statistical tools such as design of experiments, analysis of variance, and regression analysis were used to develop the relationships. The developed empirical relationship can be effectively used to predict the tensile strength of PC-TIG welded AZ61A magnesium alloy joints at the 95% confidence level. The results indicated that the pulsed current had the greatest influence on tensile strength, followed by pulsed on time, pulse frequency, and base current.

12.3.3.5 Pulsed Plasma Additive Manufacturing

Recently, Lin et al. (2016) developed a novel application of current-pulsed micro-PTA technology called, pulsed plasma additive manufacturing (PP-AM), in which a micro-PTA system is used for the deposition of thin coatings or standalone parts for additive manufacturing using a wire as feed material introduced into the weld pool as illustrated in Fig. 12.14a. In this research, several Ti-6Al-4V thin wall coatings or standalone parts were deposited by an optimized PP-AM process, in which the heat input was gradually decreased layer by layer. The deposited thin wall consisted of various morphologies with different microstructure, such as epitaxial growth of prior β-grains, martensite, and horizontal layer bands of Widmanstätten, which depend on the heat input, multiple thermal cycles, and gradual cooling rate in the deposition process. Both of the size and growth direction of prior β grains are affected by the gradual reduced heat input of the pulsed plasma arc. The technology offers an important potential due to its efficiency, convenience, and cost-savings comparing with other AM process.

12.3.3.6 High Energy PTA

The use of high energy PTA (HE-PTA) developed by SNMI, Avignon, France [Proner et al. (1997a, b)], was proposed for

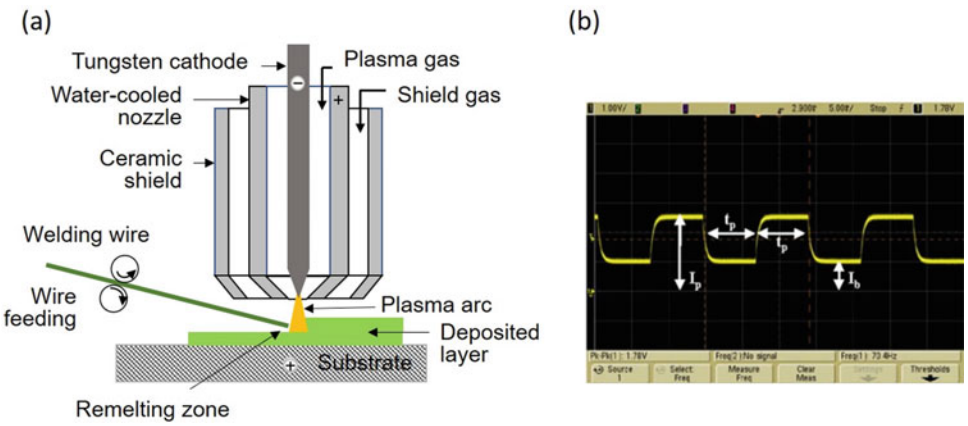

Fig. 12.14 (**a**) Schematic representation of the PP-AM process, (**b**) measured current [Lin J.J et al. (2016)]

the reduction of the heat input to small parts. The development aimed at the preparation of wear-resistant coatings of smaller parts such as internal combustion engine valves, with minimal needs for water-cooling. The arc in this case is highly constricted providing a small attachment spot diameter at the workpiece, with high current densities and high energy densities. The relative torch-to-substrate translation velocity can be very high giving rise to low heating of the substrate, low dilution values, and high cooling rates resulting in a coating with a fine microstructure. The required translation velocity, v_{tras}, is function of the attachment spot diameter D, melted layer thickness δ, and thermophysical properties of the substrate as given in Eq. 12.2:

$$v_{tras} = \left(\frac{D}{5\,\delta^2}\right)\left(\frac{\kappa}{\rho\, c_p}\right) \tag{12.2}$$

with κ, ρ, and c_p being respectively the thermal conductivity, density, and specific heat of the substrate material. The condition for the required power input at a specific velocity and melt depth is given in Eq. 12.3:

$$\left(\frac{V\,I}{v\,D}\right) \geq 10^7 \left(\frac{J}{m^2}\right) \tag{12.3}$$

High energy PTA (HE-PTA) coatings have been successfully used for the coating of steel plates with a thin layer of Co-alloy with minimal dilution [Proner et al. (1997a, b)]. Microhardness profiles of the coatings obtained are given in Fig. 12.15 which shows (HE-PTA) values significantly higher than those obtained by conventional PTA technology.

12.3.3.7 PTA Operating in Reverse Polarity Mode

A number of studies have been directed toward process development for coatings of light metals such as aluminum and magnesium alloys. These have a low melting points requiring reduced heat input to the substrate and an oxide surface layer that needs to be removed to obtain good adhesion of the coating [Gebert and Bouaifi (2005)]. They also have high thermal diffusivities resulting in rapid transfer of the heat from the arc attachment to the rest of the substrate. The consequence is that it will take a relatively long time to reach the melting point, but then a major part of the substrate may be molten. Reduction of the overall heat transfer is necessary accompanied by an increase in the local heat flux, as can be achieved by a reverse arc heating though small cathode spots. Removal of the oxide layer is also possible by thermal means, heating the substrate and melting the oxide with He as addition in the plasma gas. However, this process creates larger melt pools and movement of the molten material [Dilthey et al. (1999)]. Operating the arc in a reverse polarity mode, with the substrate serving as the cathode, will result in lower overall heat transfer to the substrate, and a high heat flux density in the continuously moving cathode spots. Cathodic arc deoxidation has been a standard practice in the metallurgical industry.

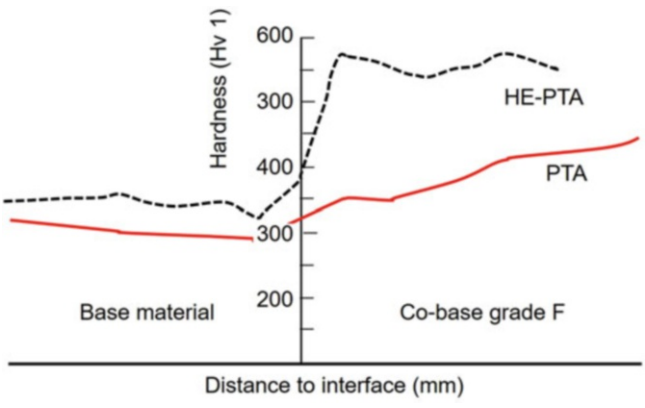

Fig. 12.15 Comparison of hardness profiles across a Co-alloy coating on steel for regular (PTA) and high energy PTA (HE-PTA) [Proner et al. (1997a, b)]

Dilthey et al. (1999) and Lugscheider et al. (1999) describe a PTA process with direct current combined polarity heating, in which the pilot arc is established between the tungsten cathode and the pilot arc anode nozzle, but the transferred arc is struck between the pilot arc anode nozzle and the workpiece as the cathode. Significant increases in wear resistance have been achieved by either dispersing a hard material such as WC/W_2C into the molten surface of a $AlMgSi_{0.5}$ alloy, depositing an aluminum alloy together with a hard material, or alloying the substrate material with a deposited material to generate hard phases. For this process, the transferred arc current was reduced and the pilot arc current increased. The pilot arc anode had been designed for improved water-cooling to reduce the erosion due to higher thermal fluxes from two arcs. The same arrangement of a DC combined polarity has been used for increasing the wear resistance of AlMg4.5Mn [Dilthey et al. (2008)]. The coating material was AlCuMg alloy reinforced by up to 70 wt % fused tungsten carbide ($WC + W_2C$) or up to 50 wt% TiC. Hard coatings were deposited using pilot arc current of 120 A, transferred arc current of 100 A, plasma gas flow rate of 0.5–1 slm, carrier gas flow rate of 4 slm, and shield gas flow rate of 10 slm, oscillation with an amplitude of 10 mm and frequency of 1.8 Hz. These had significantly improved wear characteristics compared to the base material, by a factor of 40 for the tungsten carbide and a factor 25 for the TiC-containing coatings [Dilthey et al. (2008)]. The carbide particles were uniformly distributed in the coating. Addition of Ni into the coating material further improved hardness through the formation of hard intermetallic phases which also resulted in more brittle coatings.

12.3.3.8 Hard Coatings on Magnesium

Magnesium and its alloys are attractive as structural material for a wide range of applications allowing for more weight reduction than aluminum for an equivalent strength. However, because of their poor corrosion and wear resistance properties, they require coatings as described by Gebert et al. (2002). Coatings have been obtained using a matrix material for the composite coating of either Al or $AlSi_{12}$ with the addition of up to 10 vol.% Mn or Si and reinforcing particles of TiC, SiC, or B_4C. The best coatings were obtained with the workpiece at a positive polarity and with about 30 vol.% He added to the plasma gas to increase penetration depth to 2 or 3 mm. While the TiC and SiC particles have been non-uniformly distributed in the coating, a uniform distribution with the lighter B_4C was achieved. The hardness increases, as well as the wear resistance increases were dependent on the amount of B_4C addition, with 7.5–10% carbide giving strong improvements particularly to the wear rate.

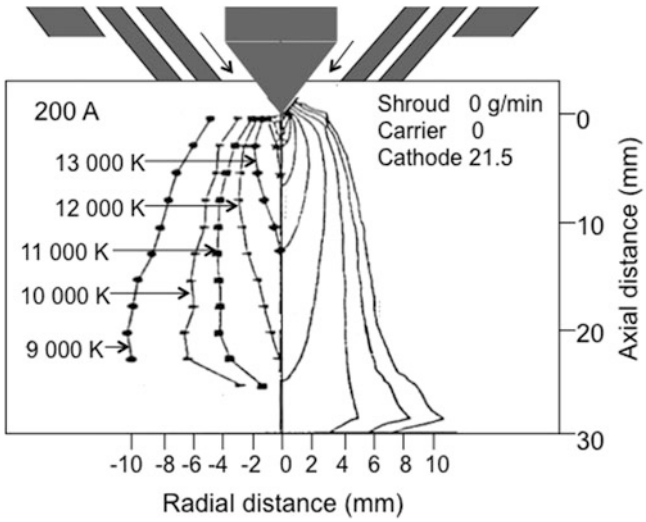

Fig. 12.16 Examples of temperature fields in an argon arc with I = 200 A, 1 atm, and torch-to-substrate distance = 30 mm, (LHS) measurements, (RHS) modeling results [Young et al. (1983)]

12.4 Gas and Particle Dynamics in Plasma Transferred Arc Coating

Compared to other plasma spray coating processes, relatively few process characterization studies have been devoted to PTA. The process, however, bears enough similarity to TIG and MIG welding, and plasma arc cutting, that some of the studies involving these processes can be used for the understanding of the basic phenomena involved in the PTA process.

12.4.1 Temperature Distributions in the Arc

The temperature distributions and heat fluxes in a TIG welding arc have been well characterized by spectroscopic temperature measurements and modeling [Hsu et al. (1983), Lowke et al. (1997), Lowke et al. (2005), Bini et al. (2007), Etemadi (1982)]. Figure 12.16 shows its LHS typical temperature distributions obtained for a 200 A argon arc at atmospheric pressure and corresponding modeling results on its RHS [Young et al. (1983)]. The constriction encountered in a PTA arc will increase the peak temperatures on the arc axis and result in higher temperature gradients. The temperature distributions in a plasma cutting arc at different axial locations between the nozzle and the workpiece (z) are given in Fig. 12.17 for an oxygen arc at a current of 200 A [Peters et al. (2007)]. Because of the smaller nozzle diameter (2 mm), the constriction in this configuration is somewhat higher than that in a typical PTA torch. The plasma gas being oxygen at a relatively higher plasma gas flow rate also gives rise to higher constriction.

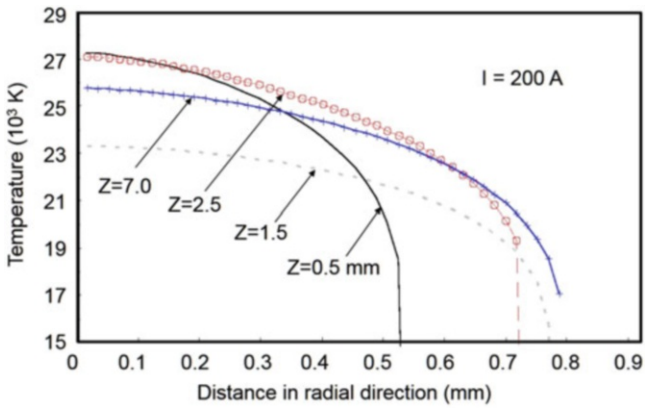

Fig. 12.17 Radial temperature distributions at different axial locations in a cutting arc derived from spectroscopic measurements, I = 200 A, nozzle i.d. = 2 mm, plasma gas flow rate = 39 slm (O2), torch-to-substrate distance = 13 mm. [Peters et al. (2007)]

Figure 12.18 shows a plasma welding torch with a nozzle i.d. = 3.45 mm, the effects of variation of the arc current (100–260 A), and plasma gas flow rate (2–8 slm Ar), on the temperature distributions between the nozzle exit and the substrate [Evrard and Blanchet (1970), Ducos (1985)]. It can be seen in Fig. 12.18a, b,c that an increase in arc current from 100 A to 260 A results in a corresponding increase of the arc diameter and of the anode attachment, giving rise to a higher temperature in front of the substrate, with hardly any increase of the peak temperature at the cathode attachment. The equivalent arc diameter, d_e (diameter of current path), can be estimated using Ohm's law according to the approximate relations:

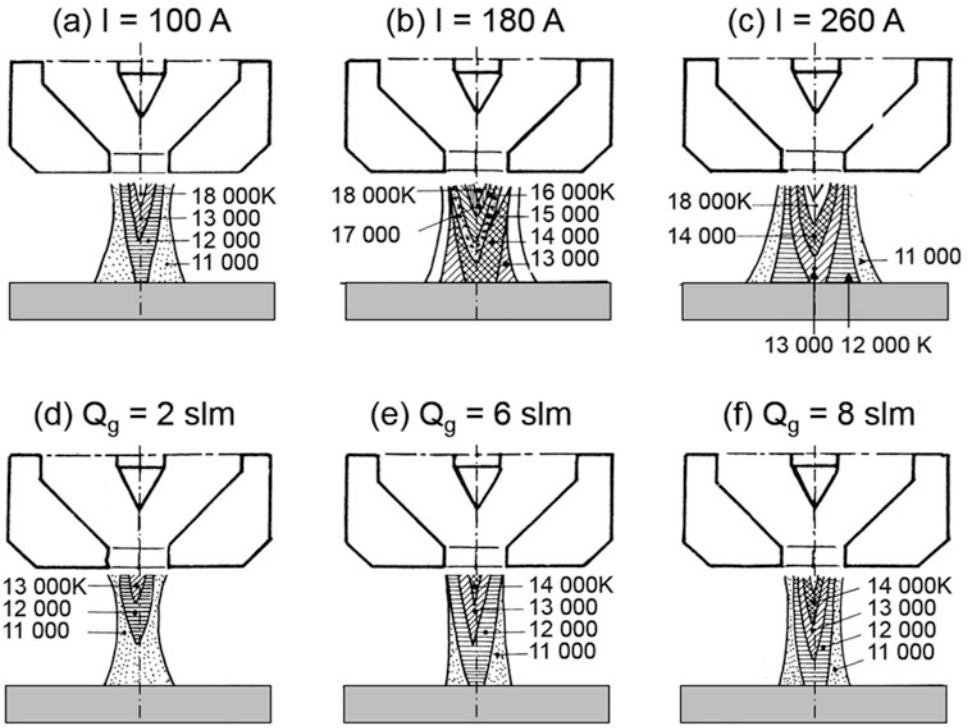

Fig. 12.18 Temperature fields in an arc struck between a plasma welding torch and the substrate for an anode nozzle i.d. = 3.45 mm (a, b, c) for different arc currents at a gas flow rate of 4 slm (Ar) and (d, e, f) for different argon gas flow rates at an arc current of 100 A [Evrard and Blanchet (1970)]

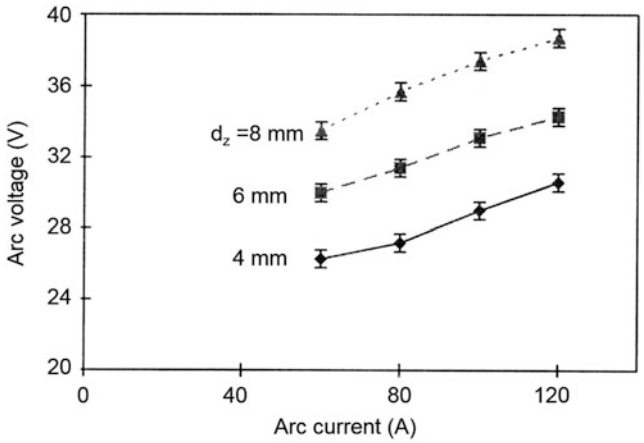

Fig. 12.19 Arc voltage as function of arc current for a PTA torch operating with 4 slm of (Ar) and Cu substrate for different torch-to-substrate distances(dz) [Leylavergne et al. (1998)]

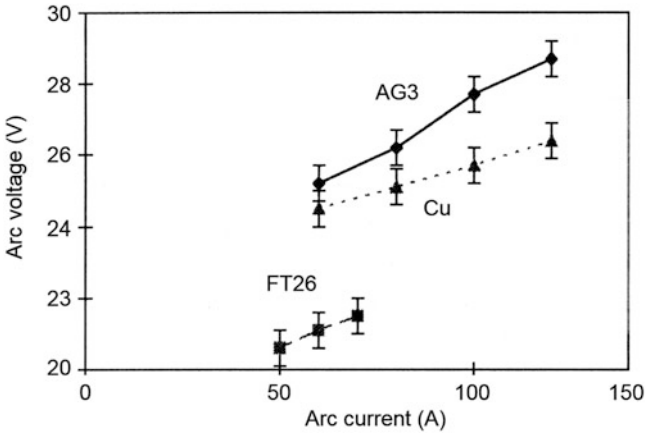

Fig. 12.20 Arc voltage as function of arc current for different anode materials for a PTA torch operating at 4 slm of (Ar) and with a torch-to-substrate distance of 6 mm, substrate materials were Al alloy (AG3), cast iron (FT 26), and copper [Leylavergne et al. (1998)]

$$I = \left(\frac{\pi d_e^2}{4}\right) \overline{\sigma_{ar}}\, E \tag{12.4}$$

$$d_e = 2 \times \sqrt{\frac{I}{\pi\, \overline{\sigma_{ar}}\, E}} \tag{12.5}$$

with I the arc current, $\overline{\sigma_{ac}}$ the electrical conductivity of argon averaged over the arc cross section, and E the electric field intensity. Increase of the plasma gas flow rate (Figs. 12.18d, e, f) has essentially a similar constricting effect on the arc giving rise to an increase of the plasma temperature in front the substrate and consequently an increase of the heat flux distribution to the substrate.

Because of the constricted nature of the arc in a PTA torch, an increase of the arc current gives rise to an almost linear increase of the arc voltage as shown in Fig. 12.19. The same trend is observed at all torch-to-substrate distances "standoff distances" with the arc voltage increasing, almost linearly, with the increase of the arc length [Leylavergne et al. (1998)]. Figure 12.20 shows the arc voltage Vs. Current relationship

depends also on the nature of the substrate material (anode). The highest voltage was observed for Al alloy (25 V at 60 A and 6 mm) and the lowest voltage for cast iron (~21 V at 60 A and 6 mm).

12.4.2 Heat Flux to the Substrate

Analytical expressions for the heat fluxes to the substrate (anode) derived by Jenista et al. (1997a) and Heberlein et al. (2007) showed that the anode heat flux reflects the contribution of a wide range of different phenomena involved as given in Eq. 12.6:

$$q_a = j_e\phi_a + q_e - \kappa_e \frac{dT_e}{dz} - \kappa_h \frac{dT_h}{dz} + j_i(E_i - \phi_a) + Q_R \quad (12.6)$$

with q_a the anode heat flux; j_e the electron current density; ϕ_a the workfunction of the anode material; q_e the electron enthalpy flux; κ_e, T_e, and κ_h, T_h the thermal conductivities and temperatures of the electrons and the heavy particles, respectively; j_i the ion current density, E_i the ionization potential of the plasma gas; and Q_R the heat transfer by radiation [Heberlein et al. (2007)]. The first term on the right-hand side is due to the incorporation of the electrons into the metal lattice (electron condensation); the second term is the enthalpy flux carried by the electrons (electron enthalpy); the third and fourth terms are the (electron conduction) and (heavy particle conduction), respectively; and the fifth term is the energy release due to recombination of ions diffusing to the anode surface (ion recombination); and the last term expresses the radiation heat flux from the plasma to the anode.

Radial profiles of the local heat flux distributions for a 100 A argon arc are given in Fig. 12.21. These show that the

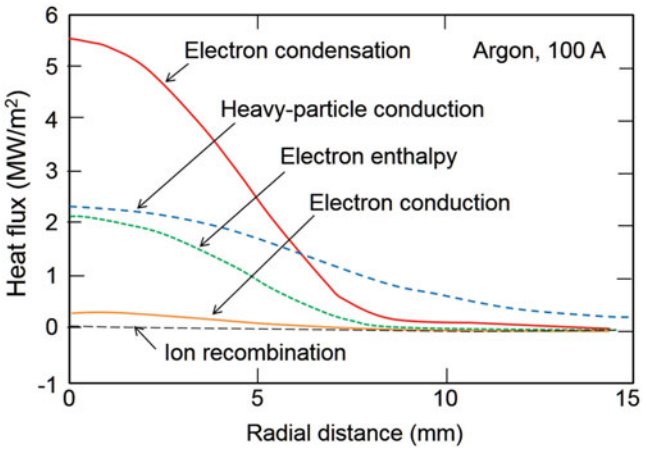

Fig. 12.21 Contributions to the heat flux to the substrate surface for a 100 A argon arc, at atmospheric pressure with a diffuse anode attachment [Jenista et al. (1997)]

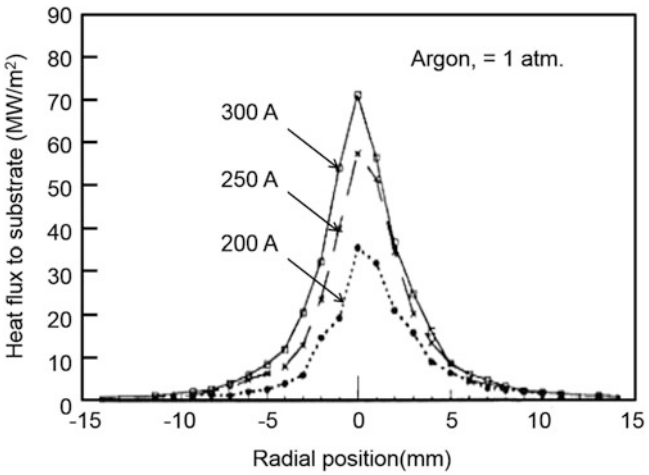

Fig. 12.22 Measured anode heat flux distributions for different arc currents in argon at 1 atm. [Menart (1996)]

electron condensation, electron enthalpy, and heavy particle conduction terms are the most important contributors to the heat transfer to the anode. [Jenista et al. (1997), Heberlein et al. (2007), Yang et al. (2008)]. The model predictions are in good agreement with experimental data obtained for plasma arc welding. Heat fluxes' distributions to the substrate measured using an especially designed heat flux probe for TIG type welding arcs for different arc currents in argon are given in Fig. 12.22 [Menart (1996)]. These show the heat flux to the substrate increases with the increase of the arc current. Higher heat fluxes in a PTA torch are expected due to the higher constriction of the arc the higher plasma gas flow rates.

Measurements of heat fluxes to the substrate were also reported by Leylavergne et al. (1998), for a PTA torch with the pilot arc off and without powder injection. These were obtained using a calorimetric method, for different arc currents (60–120 A), different torch-to-substrate distances (4, 6, 8 mm), different plasma gas flow rates (3, 4, 5 slm Ar), different shield gas flow rates (0, 20, 30, 40 slm He), and substrates consisting of Al alloy, cast iron, and copper. Typical results are given in Fig. 12.23, and Fig. 12.24 shows a practically linear increase of the heat flux to the substrate (anode) with the increase of the arc current and the torch-to-substrate distance. Assuming that only the heat transfer by convection and radiation is dependent on the anode distance, an extrapolation to a zero distance will give the heat flux due to the current transfer to the anode, which is independent of distance. The total arc power, torch efficiency, and different heat flux values are given in Fig. 12.24 and in Table 12.3 [Leylavergne et al. (1998)].

Considering that, as noted earlier, the arc voltage shows a dependence on the anode material, it is not surprising that the anode heat flux is also anode–material dependent with, for

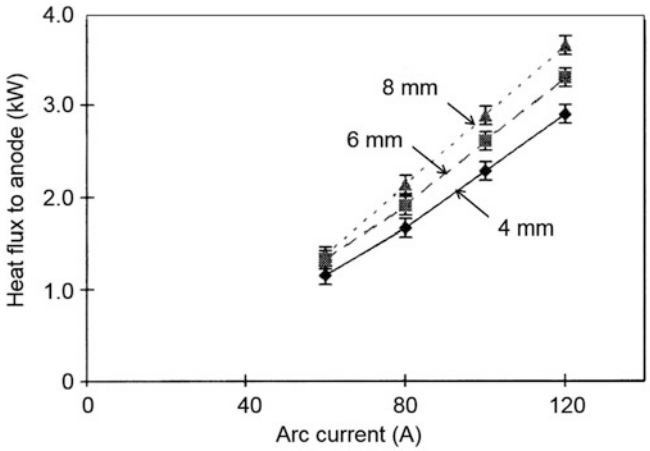

Fig. 12.23 Anode heat flux as function of arc current and arc length for a Cu anode without shield gas and 4 slm (Ar) plasma gas flow [Leylavergne et al. (1998)]

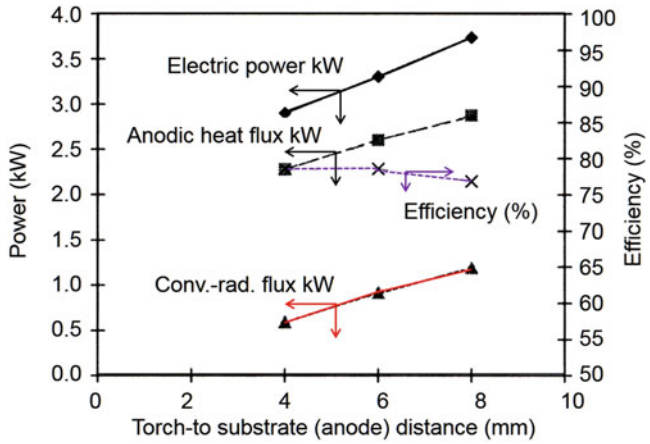

Fig. 12.24 Measured values of electric power input, anode heat flux, and derived values of convective–radiative power loss from the arc, and the arc heating efficiency for arc with plasma gas flow rate of 4 slm (Ar), arc current of 100 A and Cu substrate [Leylavergne et al. (1998)]

Table 12.3 Arc power and heat transfer to the anode for different torch-to-anode distances for Cu anode and 100 A arc current, data from Leylavergne et al. (1998)

Torch-to-anode distance (mm)	4	6	8
Arc power ($V \times I$) (kW)	2.9	3.3	3.7
Q_{an} (kW)	2.3	2.55	2.8
Q_{con} (kW)	0.6	0.9	1.2

example, the transfer to a copper anode being about 50% higher than that for a cast iron anode. While the cast iron substrate has the largest extent of evaporation and molten droplet ejection, the mechanisms could not account for the difference in the measured heat fluxes. Based on a dimensionless analysis, the following correlation between the operating parameters and the substrate heat transfer to the anode was reported by Leylavergne et al. (1998)

$$Q_{an} = 62.4\, I^{1.36} \dot{m}_g^{0.046} d_z^{0.382} \tag{12.7}$$

with Q_{an} the anode heat flux in (W), I the arc current in (A), $\dot{m}_g$ the plasma gas flow rate in (kg/s), and d_z the torch-to-anode distance in (m).

Measurements of substrate heat flux distribution in PTA system were reported by Dilthey et al. (1993) using a split anode arrangement similar to one described first by Nestor (1962). The total heat flux to the substrate was measured thanks to two halves of a copper anode, thermally insulated from each other and separately cooled. The heat flux distribution was determined calorimetrically by moving the substrate across the arc attachment. Assuming a rotational symmetry, the heat flux distribution was described by as function of a "constriction parameter, k"[Dilthey et al. (1993)] defined as:

$$q(r) = q_m \ exp\left(-kr^2\right) \tag{12.8}$$

with $q(r)$ the local heat flux to the substrate, q_m the maximum heat flux for a given condition, and r the distance in the radial coordinate. The authors reported that for a nozzle i.d. = 4 mm, the constriction parameter k varied for a nozzle diameter of 4 mm, plasma gas flow rate of 3.9 slm, without transferred arc, from 1.9 to 2.9 cm^{-2} when the pilot arc current was increased from 120 to 250 A. For a transferred arc current of 120 A, the corresponding values were 2.6 to 3.9 cm^{-2}. The associated heat fluxes are shown in Table 12.4 [Dilthey et al. (1993)]. Decreasing the nozzle i.d. to 2.5 mm, and the plasma gas flow rate to 1.5 slm, the constriction factor values ranged from 2.45 to 3.45 cm^{-2} without transferred arc for a pilot arc current variation of 100–300 A and from 4.15 to about 4.75 cm^{-2} for pilot arc current variation from 40 to about 250 A, with a transferred arc current of 120 A. The associated heat fluxes were 150–500 W and 2130 to about 2300 W, respectively.

It must be emphasized that Q_{sub} is the total heat transfer to the substrate and that these values include the contribution of the pilot arc power, i.e., are not only due to the anode heat transfer. Substrate melting and coating dilution are determined not only by the substrate heat transfer but

Table 12.4 Substrate heat transfer for different pilot arc and transferred arc currents, for nozzle diameter of 4 mm and a plasma gas flow rate of 3.9 slm(Ar) [Dilthey et al. (1993)]

I_{pilot} (A)	I_{arc} (A)	Q_{sub} (W)	k (cm^{-2})
120	0	275	1.9
200	0	500	
250	0	530	2.9
120	120	2220	2.6
200	120	2265	
250	120	2280	3.9

also by the distribution of the heat flux, expressed by the constriction parameter *k*. It can be clearly seen that substrate heating is due to the transferred arc, and the pilot arc contributes only in the order of 10–20%. About 32–48% of the electrical energy goes into heating of the substrate [Dilthey et al. (1993)].

The same authors also measured calorimetrically the heat content of the particles of the material to be deposited and derived mean particle temperatures from these values for CrNi steel particles with a diameter range from 100 to 160 μm. The results are shown in Table 12.5 [Dilthey et al. (1993)]. It is clear that most particle heating is due to the transferred arc. It can be seen from these results that the transferred arc current has the strongest effect on the process, both with respect to substrate heating/dilution and with respect to particle heating/deposition rates.

In the development of a process in which the plasma gas flow was modulated, Ebert et al. (2009) measured the stagnation pressure at the substrate surface with an orifice in the substrate connected to a pressure sensor. Moving the torch over the substrate gave radial pressure profiles which can be used to estimate the corresponding impact velocity profiles of the plasma on the substrate. Variation of the peak stagnation pressures with the plasma gas flow rate, for an arc current of 95 A, is given in Table 12.6.

The full width at half maximum (FWHM) of the stagnation pressure profile remained essentially constant between 3 and 4 mm with the increase of the gas flow rate from 1 to 4 slm. The pressure is also strongly influenced by the arc current increasing with the increase of the current and to a lesser extent by the nozzle design (decreasing with increasing diameter) and the substrate distance (decreasing with increasing distance). With higher stagnation pressure on the substrate, a displacement of the molten metal must be expected. Modulating the plasma gas flow or arc current will result in molten metal movement that will give a more uniform distribution of the particles feed into the molten metal pool.

Table 12.5 Mean temperatures for CrNi steel particles, 100–160 μm diameter with plasma gas flow rate of 1.3 slm (Ar) [Dilthey et al. (1993)]

I_{pilot} [A]	I_{arc} [A]	Mean particle temperature [K]
150	0	848
0	120	1641
150	120	1845

Table 12.6 Stagnation pressure on the substrate as function of the plasma gas flow rate for an arc current of 95 A [Ebert et al. (2009)]

Plasma gas flow rate (slm) Ar	1.0	2.0	3.0	4.0
Stagnation pressure (Pa)	330	430	525	620

12.4.3 Process Modeling

12.4.3.1 Arc Gas Dynamics and Heat Transfer

While numerous models and simulations exist for tungsten inert gas (TIG) and metal inert gas (MIG) welding arcs, very little modeling effort of the PTA process has been dedicated to the PTA deposition process. Because of the similarity between the PAC deposition process and arc welding processes, a few examples of modeling studies of arc constriction and weld pool profile in gas tungsten arc welding (GTAW) are given.

Particularly relevant is the study by Toropchin et al. (2014) of arc constriction due to the ceramic nozzle surrounding the tungsten electrode in TIG or GTAW. Schematics of some of the configurations studied are given in Fig. 12.25, showing a straight ceramic nozzle Fig. 12.25a, b, and a converging nozzle Fig. 12.25c. The corresponding shape of the arcs obtained with pure argon with each of these nozzle designs is superposed on the figure. It may be noted that the convergent nozzle design gives rise to a more constricted arc compared to that of the other two design options. While it is relatively easy to calculate the temperature and velocity distributions for the arc with pure argon as plasma gas, the problem is considerably more complex once the workpiece starts melting and vaporizing. The metal vapors evolving from the molten metal pool diffuse into the arc modifying significantly the thermodynamic, transport and radiative properties of the plasma. Moreover, in order to model the weld pool, one must also consider the different forces acting on the melt, which gives rise to internal recirculation of the molten metal. Among the forces that need to be considered are:

- ***The Marangoni effect*** by which the presence of a gradient in surface tension of the melt induces the liquid to flow away from regions of low surface tension
- ***The drag force*** acting opposite to the direction of the flow on the surface of the pool
- ***The electromagnetic forces*** due to the arc current
- ***The buoyancy effects*** which gives rise to an upward force exerted by the molten metal in an opposition to the weight of an immersed object

The conservation equations of fluid dynamics and heat transfer are used to derive the flow and temperature fields in the arc and weld profile of the molten metal pool. Typical results obtained for each of the geometries identified in Fig. 12.25 are given in Fig. 12.26 for an argon plasma with arc currents of 200 A (Fig. 12.26a) and 150 A (Fig. 12.26b, c). These show temperatures as high as 18,000 to 20,000 K near the cathode tip, with strong temperature gradients in the radial direction specially in the presence of the constricted

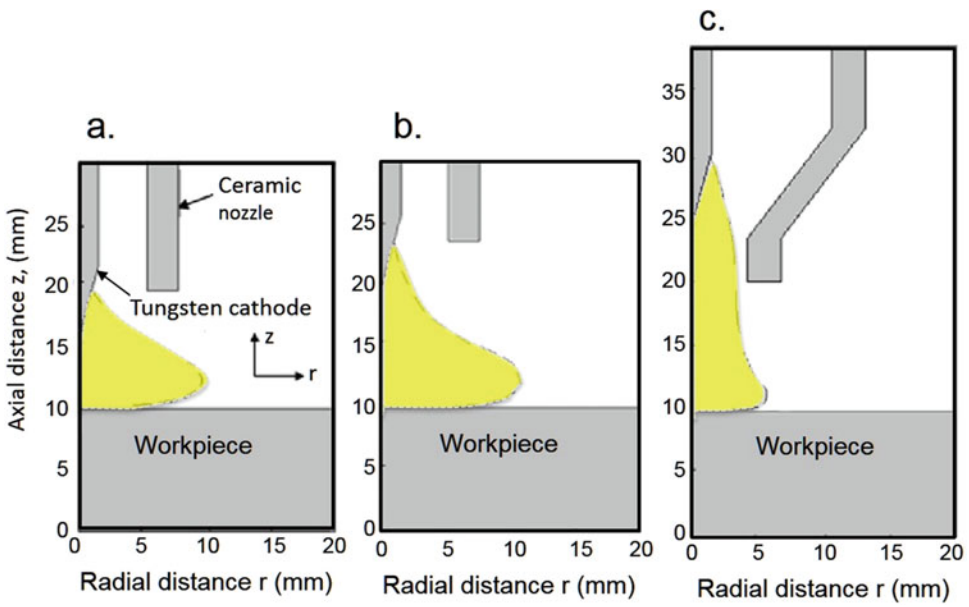

Fig. 12.25 Geometric configurations of the arc confinement nozzle with different internal diameters of the nozzle, locations of the cathode tip (Δz is the distances between the cathode tip and the anode) and the nozzle exit (**a**) i.d. = 11 mm, Δz = 6 mm (**b**) i.d. = 11 mm, Δz = 10 mm (**c**) i.d. =8.1 mm, Δz = 16 mm [Toropchin et al. (2014)]

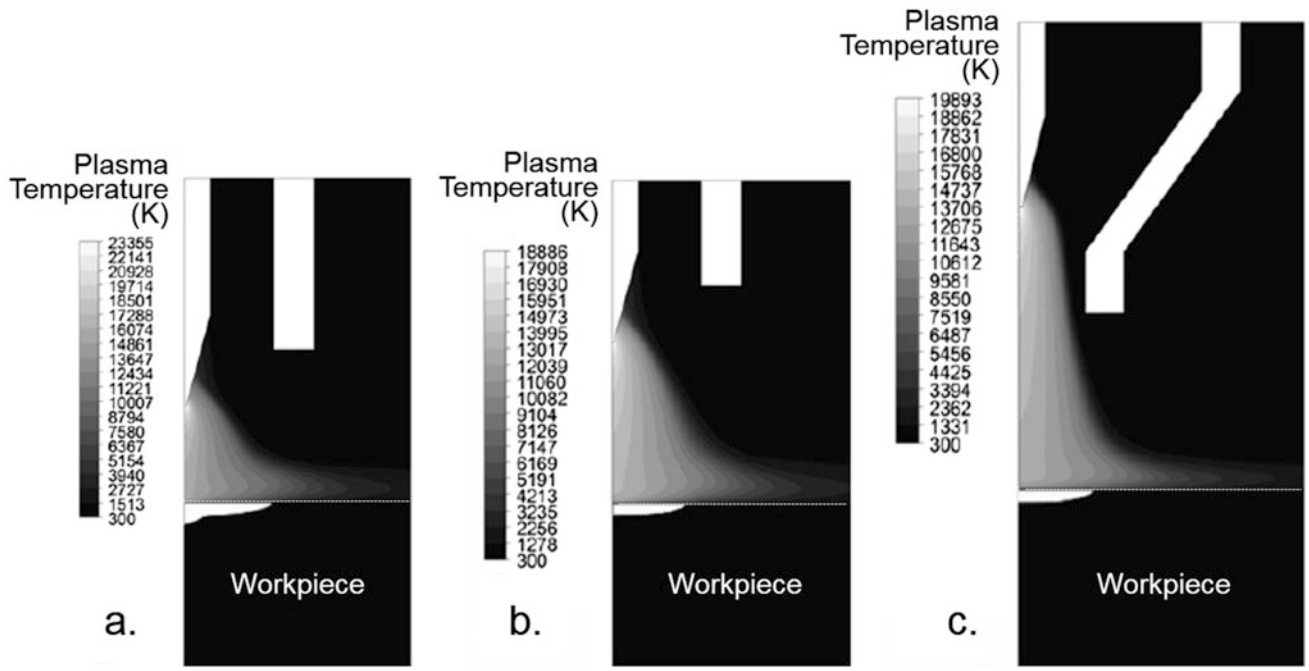

Fig. 12.26 Corresponding weld pool profiles and temperature fields in an argon arc plasma for the same geometrical parameters given in Fig. 12.24 for arc currents (**a**) I = 200A (**b**) and (**c**) I = 150A [Toropchin et al. (2014)]

ceramic nozzle shown in Fig 12.26c. The lower part of Fig. 12.26 shows the corresponding profile of the molten metal pool in the workpiece. The results are blown out for clarity in Fig. 12.27, for the case of 150 A arc using the ceramic nozzle (Fig. 12.25c). The results given in Fig. 12.27a and b also show respectively the corresponding flow vectors in the weld pool "with" and "without" inclusion of the Marangoni force in the calculation model. The markedly different weld depths in each of these two cases are related to basic material properties such as specific heat, electrical and thermal conductivity and model formulation. According to Toropchin et al. (2014), including the Marangoni effect

gives rise to a dependence of the direction of melt recirculation in the molten metal pool on the variation of surface tension of the melt with temperature. Comparing a material with falling surface tension characteristic, versus a material, such as mild steel, with a rising characteristic, reviles a significantly different weld pool profiles and circulation patterns of in the molten metal pool in each of these two cases as shown in Fig. 12.28.

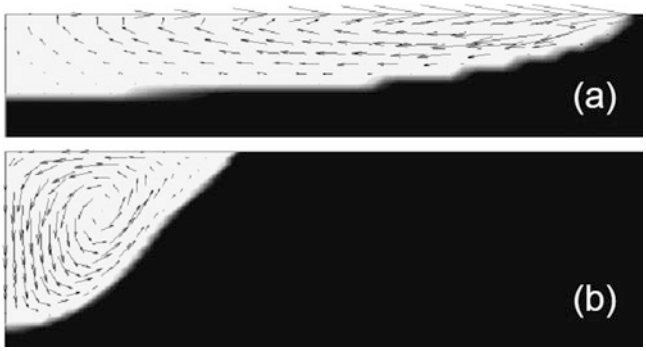

Fig. 12.27 Flow vectors in the weld pool for mild steel S235 at a current of 150A. (**a**) Computation including the Marangoni forces and (**b**) computation neglecting the Marangoni forces [Toropchin et al. (2014)]

It is important to point out that the weld pool profile formed in plasma arc welding depends on a large number of parameters, which includes the chemistry of the materials to be welded and that of the plasma and shield gases. The effect is clearly demonstrated experimentally by Tanaka and Lowke (2007) for the welding of stainless steel plates (SUS304) under essentially the same physical conditions with tungsten electrode 3.2 mm in diameter, distance of 5 mm between the electrode tip and the steel plate, and arc current of 150 A, at atmospheric pressure with argon as plasma gas. Photographs of the cross section of two stainless steel plates with sulfur contents of 40 and 220 ppm are given in Fig. 12.29. These show a significant difference in the corresponding weld pool profiles for each of these two plates depending on their sulfur content. The weld profile for the plates with 40 ppm sulfur being wide and shallow in sharp contrast to the profile obtained with the plates containing 220 ppm of sulfur in which the weld pool is narrow and deep.

Further support for the influence of the composition of the plasma and shield gases on the weld metal pool profile was provided by Tanaka and Lowke (2007). Micrographs given in Fig. 12.30 show typical cross sections of welds for stainless steel, conducted with an arc current of 150 A and arc gap of 3 mm, using Ar and He as plasma gases and a mixture of

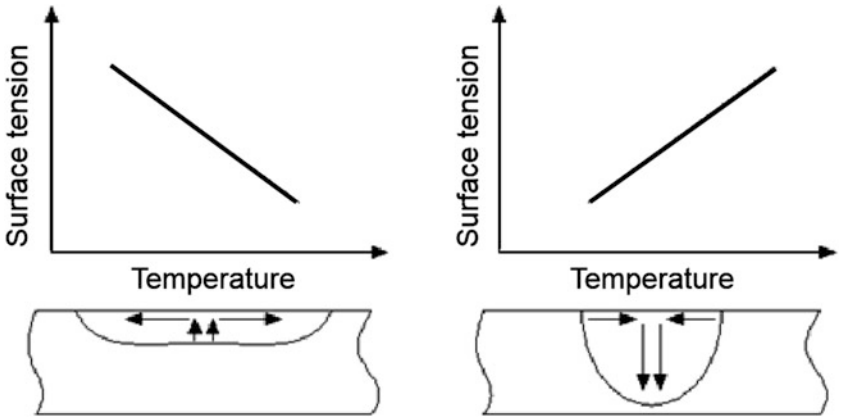

Fig. 12.28 Schematic illustration of convection in the weld pool driven by Marangoni force resulting from the temperature dependence of the surface tension [Toropchin et al. (2014)]

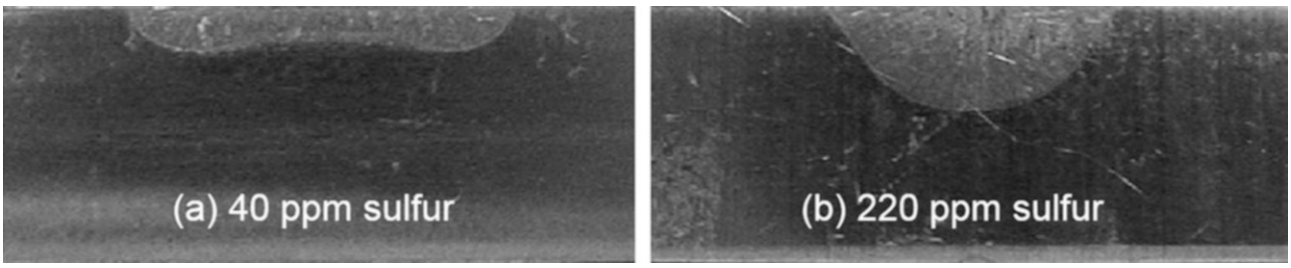

Fig. 12.29 Cross sections showing weld regions for stainless steel with different sulfur content, 150 A arcs with a 5 mm electrode separation at atmospheric pressure [Tanaka and Lowke (2007)]

Ar-CO_2 or Ar-10 vol.%H_2-CO_2 as sheath gas. The corresponding arc voltages varied with the plasma and shield gas composition being at 11.8 V for pure Ar while for an Ar arc shielded with CO_2 15 V, and 18.9 V for Ar-10 vol. %H_2-CO_2 shielded. These show the penetration depth for the argon plasma gas CO_2-shielded arc to be 4.9 mm (Fig. 12.30b) and 6.9 mm for an Ar + 10 vol.% H2 mixture as the inner nozzle gas CO2-shielded (Fig. 12.30c) while the depth for the argon arc is only 2.0 mm (Fig. 12.30a). The effect of CO_2 shielding is due to the better arc constriction, as predicted by calculations.

Tanaka and Lowke (2007) point out that mathematical modeling is a powerful tool for the understanding and control of the arc welding process provided that the model incorporates both the arc plasma as the heat source and the workpieces. The need for such an integration of these two distinct fields is due to "the close interaction between the electrode, the arc plasma and the weld pool, which constitute the welding process, and must be considered as a unified system." Murphy et al. (2009, 2010) further confirmed the necessity to include the arc plasma in the computational domain taking into account the influence of the metal vapors released from the molten metal pool on the transport and radiative properties of the plasma. The most important effect of the metal vapor is the increased electrical conductivity at low temperatures and the significant increase of radiation heat losses from the arc column, which leads to lower heat flux density and current density at the weld pool, implying a shallower weld pool. They pointed out that the product of specific heat and mass density is particularly important in determining the arc constriction and the weld pool depth.

A modeling study of the influence of the nature of the plasma gas, Ar or He, on the arc and the weld pool was reported by Yamamoto (2008). Figure 12.31 shows the

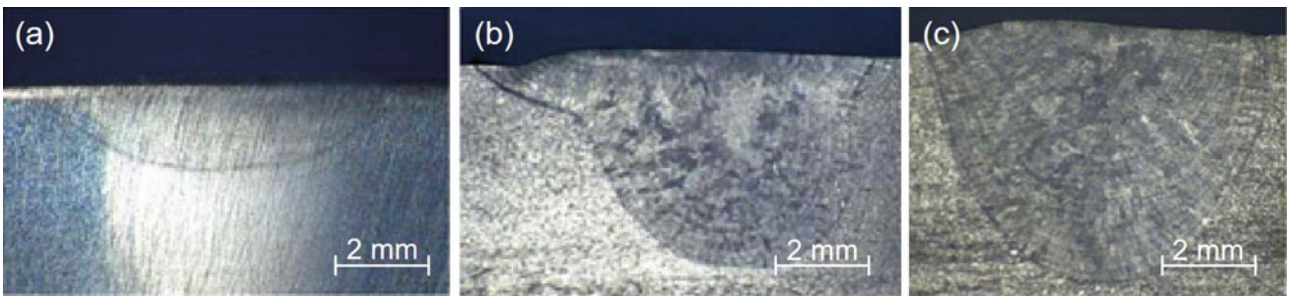

Fig. 12.30 Measured weld shape in stainless steel (SUS-304, 30 ppm sulfur) for an arc current = 120 A, arc gap =3 mm, welding speed =90 mm/min and different welding gases (**a**) Ar-TIG, (**b**) Ar + CO2, and (**c**) Ar + 10 vol.% H2 + CO2 [Tanaka and Lowke (2007)]

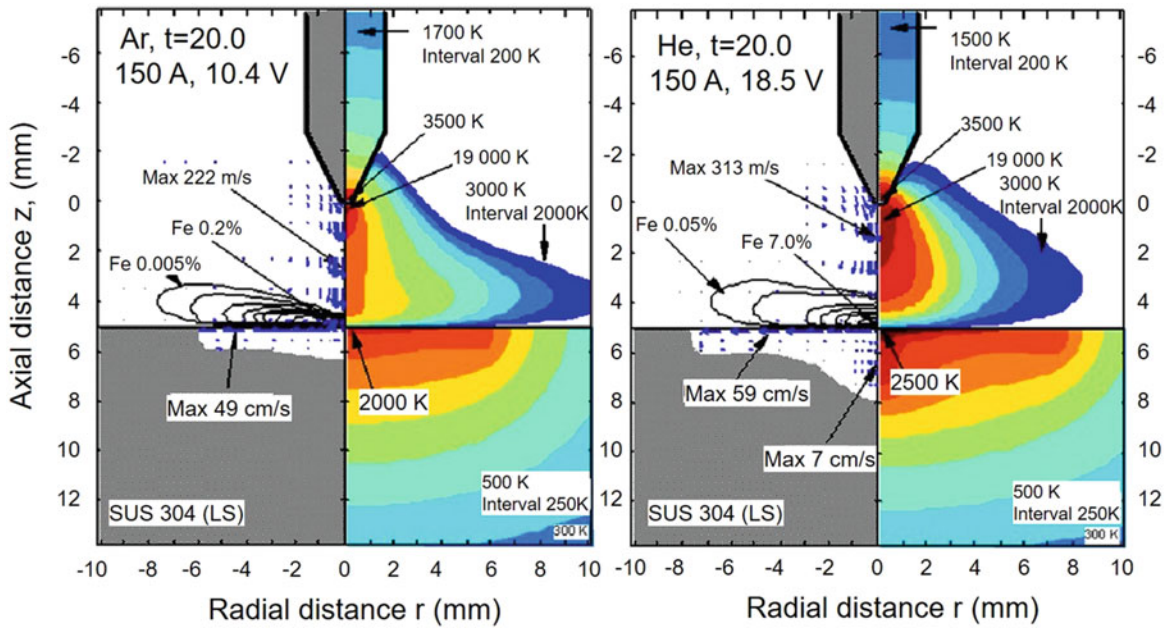

Fig. 12.31 Temperature fields (RHS) and iron vapor mole fraction fields and velocity vectors (LHS) in the arc and electrodes for 150 A arc in argon and helium at 100 kPa with a 304 stainless steel anode, after 20 s of operation. [Yamamoto (2008)]

temperatures, velocities, and iron vapor molar fractions (other components were not considered) in 150 A arc in argon and helium, with 304 stainless steel workpiece as anode. The temperature interval in the iso-contours for the plasma is 2000 K, while it is 200 K in the cathode, and 250 K in the anode. The concentration of the iron vapor released from the surface of the melt pool increases sharply with time following the initiation of the arc only to stabilize shortly after only 5 s. The maximum concentration of the iron vapor in the arc depends on the arc current and the nature of the plasma gas, reaching 0.2 vol. %, for an argon arc compared to 7.0 vol.% for the helium arc at the same arc current of 150 A. The effect is due to the higher melt pool temperature with a helium arc compared to that of an argon arc. Such high metallic vapor concentration levels can be detrimental to the welding process not only because of their influence on the plasma properties and the process energy efficiency but also because of the eventual homogenous condensation of the vapor in the colder regions of the flow forming a fine nanometer-sized fume which represent a serious health hazard to the operator [Tashiro et al. (2010)]. The use of active flux for deeper penetration can also modify the weld pool characteristics. Morisada et al. (2014) have proposed what they called "cap active" flux tungsten inert gas (CA-TIG) welding using atmospheric oxygen, to increase the penetration depth of a weld. Specially designed nozzle cap entrained air in the molten pool. The penetration depth for SUS304 stainless steel was increased by the reversal of the Marangoni convection due to the entrained oxygen, and it reached three times deeper than that of the conventional TIG welding. Authors point out that the effect of the entrained air on the mechanical properties of the joint formed by the CA-TIG welding is negligible, and the joint efficiency is high enough for conventional applications.

12.4.3.2 Melt Pool Modeling

According to Karanunakarani and Balasubramanian (2011) in conventional welding, fusion zones typically exhibit coarse columnar grains because of the prevailing thermal conditions during weld metal solidification. It often results in inferior weld mechanical properties and poor resistance to hot cracking. It is thus necessary to control solidification structure, temperatures, and thermal gradients in welds. This is especially the case when welding thin sheet materials with high thermal conductivity and diffusivity such as aluminum and magnesium alloys. Using pulsed current welding can solve the problem. When welding AA6351-T6 aluminum alloy joints pulsed current resulted in lower peak temperatures, lower magnitude of residual stresses and superior tensile properties is compared to constant current welding technique with the formation of finer grains. Razal Rose et al. (2012) studied the influence of pulse current, base current, pulse frequency, and pulse on time on tensile strength of the PC-TIG welded AZ61A magnesium. They observed that the effect of peak current and pulsing frequency initially increase the tensile properties which subsequently decreased irrespective of changes in base current and pulse on time. A maximum tensile strength of 199.5 MPa was obtained with the optimum welding parameters. Pulse current was more sensitive than the other parameters followed by pulsed on time, pulse frequency, and base current.

Modeling studies were also dedicated to the identification of the impact of substrate position on the final profile of the formed coating. The problem stems from the fact that PTA welding is presently restricted to substrates which are in a flat horizontal position. This means that damaged parts have to be dismounted to be processed. Furthermore, industry is interested in the development of strategies for PTA coating in constraint positions as complex three-dimensional (3-D) parts could be easily processed as well.

Photographs [Wilden et al. (2004)] of nickel coating on flat steel substrates obtained using PTA under "standard conditions" in horizontal and vertical orientations are given in Fig. 12.32. It can be noted that the weld obtained with the substrate in a horizontal position, Fig. 12.32a with an arc current of 80 A, powder feed rate of 20 g/min, and substrate displacement speed of 30 mm/s, is well defined with single weld beads clearly visible. In contrast, the weld obtained with the substrate in vertical position, Fig. 12.32b with the same conditions shows the molten metal flowing downward due to

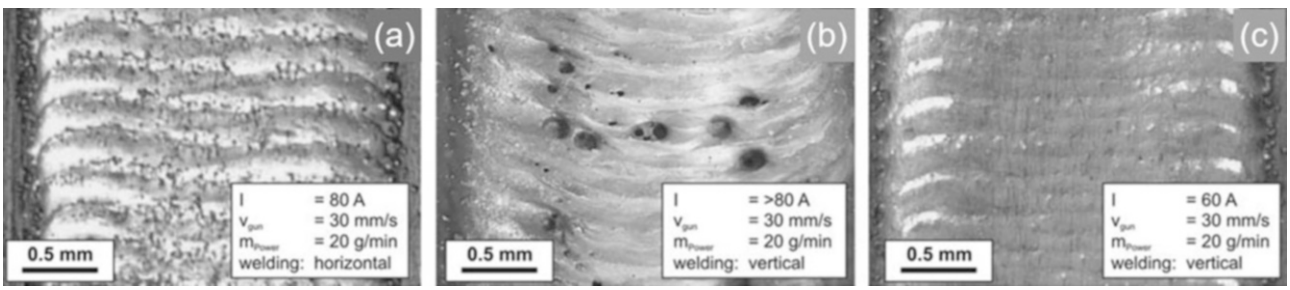

Fig. 12.32 Photographs of PTA welded nickel coating on steel substrate in different welding positions (**a**) horizontal, 80 A (**b**) vertical, 80 A (**c**) vertical, 60 A [Wilden et al. (2004)]

gravitation resulting in the formation of inhomogeneous coating with visible pores which was attributed by Wilden et al. (2004) to a too long solidification time. The reduction of the arc current from 80 A to 60 A seems to reduce such downward flow of the molten, leading to the formation of well-defined single overlapping weld beads as shown in Fig. 12.32c.

In an effort to better understand the problem and identify appropriate remedies that would allow for the use of the PTA technology in constraint positions, Wilden et al. (2006) developed a three-dimensional (3-D) model of the PTA process which they applied to the deposition of thin coatings (~500 μm) of Ni on steel with the substrate either in its conventional horizontal position or in a vertical orientation. Their model is based on the solution of the corresponding conservation equations, with the exception that the arc channel is simply represented by a 2–2.5 mm diameter channel with uniform heat dissipation, and no interaction with the pilot arc anode. The energy is transferred to the substrate and the feed material. The following operating parameters were used: pilot arc current, I_{pilot} = 10–50 A, plasma arc current, I_{arc} = 70–170 A, V_{pilot} = 20 V, arc voltage = 20 A, plasma gas flow rate = 1.5 slm (Ar), powder gas flow rate = 0.4 slm (Ar), powder feed rate 0.48–1.2 kg/h, and substrate velocity = 10–90 mm/s for 7 mm, with motion reversal following a step of 1 mm.

Typical simulation results obtained for a substrate in a horizontal position with a powder feed rate of 12 g/min, different arc powers and substrate speeds, are given in Fig. 12.33. These show that with a plasma arc power of 3.0 kW and a process velocity of 30 mm/s, Fig. 12.32a, a relatively flat surface is formed. If energy input is reduced to 2.4 kW and process speed is increased to 90 mm/s (reduced energy input per unit length), Fig. 12.33b, a rough surface with weld bead irregularities is observed.

Wilden et al. (2006) also investigated the effect of the substrate thickness on the molten pool formation during the PTA coating and its impact on the quality of the coating.

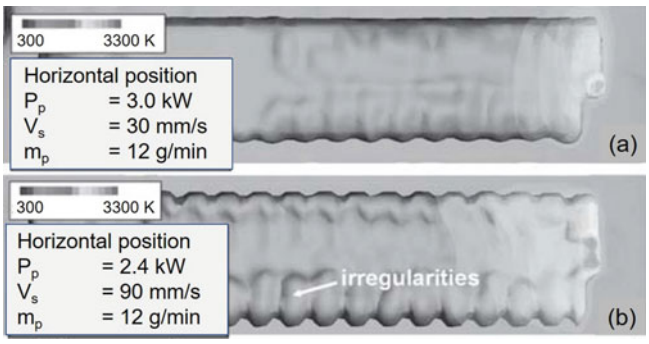

Fig. 12.33 Geometry of PTA welded Ni coating on a substrate. Temperature field (**a**) arc power 3.0 kW, process speed 30 mm/s; and (**b**) arc power 2.4 kW, process speed 90 mm/s [Wilden et al. (2006)]

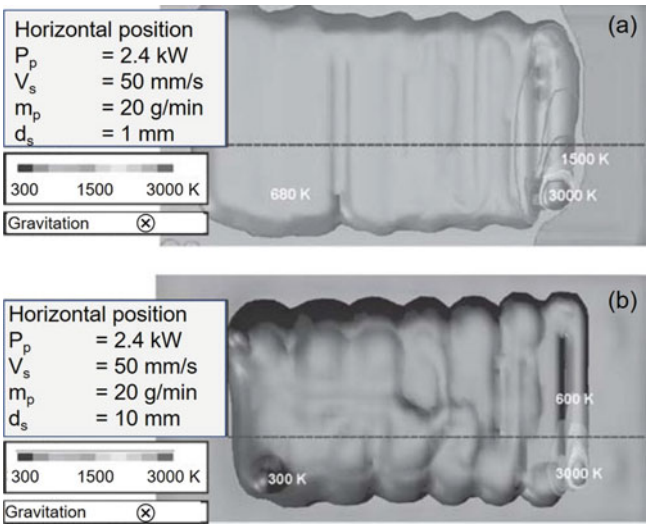

Fig. 12.34 Geometry of PTA welded Ni coating on a steel substrate in a horizontal position: (**a**) substrate thickness, 1 mm; (**b**) substrate thickness, 10 mm [Wilden et al. (2006)]

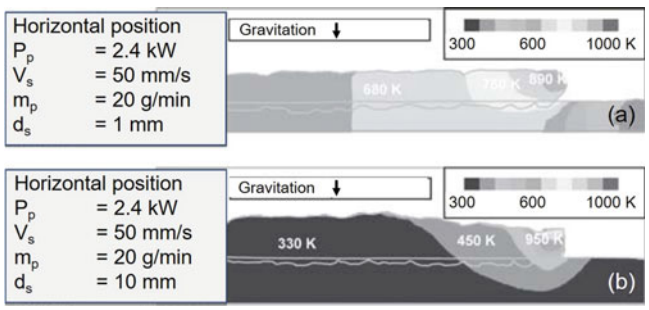

Fig. 12.35 Cross section of PTA welded Ni coating on a steel substrate in a horizontal position: (**a**) substrate thickness, 1 mm; (**b**) substrate thickness, 10 mm [Wilden et al. (2006)]

Results given in Figs. 12.34 and 12.35 were obtained for the deposition of a Ni coating on steel substrates of thickness d_s = 1 mm and 10 mm in a horizontal position, with Ni powder feed rates of 20 g/min, arc power of 2.4 kW, and substrate translation speed of 50 mm/s. The cross-sectional views given in Fig. 12.35 were made along the dotted line shown in Fig. 12.34 across the welded Ni coating. It may be noted that with a thin substrate, d_s = 1.0 mm, shown in Figs. 12 34a and 12.35a, significant heating of the substrate occurs during the coating process giving rise to the formation of a large melt pool which is difficult to handle. In contrast, the results obtained with the thicker substrate, d_s = 10.0 mm, shown in Figs. 12.34b and 12. 35b, the melt pool and the high temperature region are considerably less expanded than with the thin substrate which can be attributed to the considerably high heat dissipation capacity of the thick substrate.

The reduced coating temperature increases the viscosity and the surface tension and reduces the size of the melt pool

as well. The corresponding cross section (along the dashed line shown in Fig. 12.34) is given in Fig. 12.35. For the thinner substrate, Fig. 12.35a, coating and substrate temperature is reduced from about 1000 K near the melt pool to about 600 K in the cooled area. This is about 300 K higher than for the thick substrate, Fig. 12.35b. Additionally, the higher heat capacity and the lower coating temperature of the thicker substrate slightly reduce the material dilution in the weld bead.

Vertical welded coatings show modified properties compared to welding in flat horizontal position with identical parameters. During welding in constraint position, one must consider that coating geometry is smoother and molten material can flow downward in the direction of gravitation [Wilden et al. (2006)]. However, the power level and the deposition velocity must be adapted, generally reduced, when coating a substrate in a vertical position. Due to the flow of molten material, a better surface quality can be reached in vertical deposition, as illustrated in Fig. 12.36 representing coatings obtained in vertical spray positions with two different welding velocities.

Further modeling studies of the coating formation process were reported by Matthes et al. (2002) with the goal to identify the stress distributions in free standing shapes made by PTA. The heat input into the substrate was given as heat flux across circular area with Gaussian distribution. The size of the weld pool and the bead formation was calculated for linear motion of the torch with superimposed oscillatory movement with an amplitude of 28 mm and velocity of 7 mm/s, while the traverse velocity was 2 mm/s. The oscillation resulted in lower molten pool temperature but with larger area covered by the molten metal. Calculated temperature distributions of the substrate/coating surface were in good agreement with experimentally determined values. The stresses after solidification were tensile close to the bead and compressive farther away from it. The calculated stress values also agreed with the experimentally determined ones.

It should be noted that while many of these modeling studies have been performed without powder injection, they allow estimates of how the fundamental properties change with the process parameters. Powder deposition would likely enhance the heat transfer because the deposition of the molten material would transfer some of the arc power that would otherwise be lost to the torch.

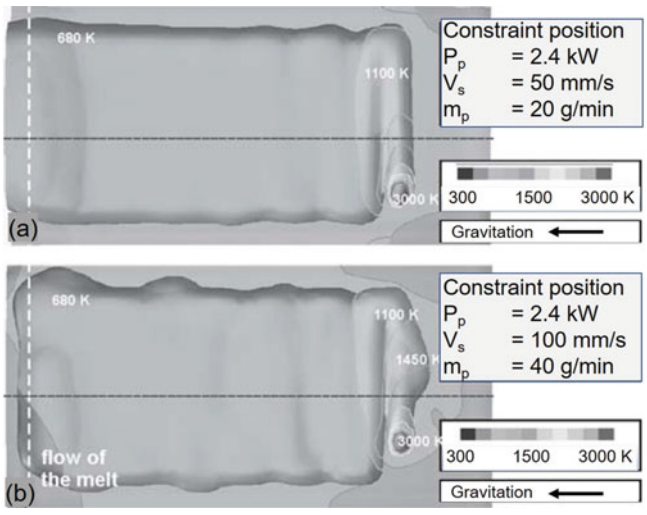

Fig. 12.36 Simulation of PTA welded Ni coating in vertical welding position with different process parameters. Temperature field (**a**) 2.4 kW, 50 mm/s; (**b**) 2.4 kW, 100 mm/s [Wilden et al. (2006)]

12.5 Coating Materials and Applications

The PTA process gives access to a large number of coating materials, various alloys, metal compounds and metal matrix composites, and there are continuously new coating materials being developed. Most applications of PTA coatings deposition technologies are for corrosion and wear resistant, taking full advantage of the superior adhesion and high density of the PTA coatings, and the possibility to select a wide range of materials and composite systems by mixing the appropriate powders. Wear is the problem, and it occurs in almost all industries where thermal sprayed coatings are used. In all cases, it is a progressive loss of material at the active surface due to the relative movement of another part or particles on this surface. The lifetime of the coating depends on its resistance to wear and its thickness, which can reach up to 10 mm with PTA coatings. Wear can also be linked to thermal fatigue initiating cracks generally propagating into the coating along carbide boundaries; these hard particles being generally used to reinforce the coating hardness and wear resistance. Such coatings are achieved using two types of powders: a metal powder close to the PTA nozzle exit and heated below their melting temperature and a ceramic one close to the molten bath to be included unmolten within the coating. Coatings have been developed for wear under different corrosive conditions, for abrasive wear, and for wear by erosion due to interaction with particulate matter.

It is important to point out that PTA coatings can be built to thicknesses of several millimeters with excellent high temperature stability, which is not always possible with other plasma spraying techniques. For example, d'Oliveira et al. (2002) characterized coatings of a cobalt-based alloy, deposited by PTA welding on an AISI 304 stainless steel substrate. Samples were subjected to temperature cycling at 1050 °C. As-deposited features and their stability to high temperature were studied; results were presented and compared with similar samples obtained by laser cladding. The performance of hard-faced material was evaluated by microstructure, chemical analysis, and microhardness measurements. For the processing conditions tested, results

showed that, for operating conditions that do not require elevated temperature, laser hard-facing showed the bests results, due to the refined solidification structure produced. However, for the high temperature tested, PTA deposits exhibited superior microstructural stability, whereas laser deposits undergo significant changes. High-temperature treatment led to changes on carbides morphology and also to precipitation, in the case of laser deposits.

Another important application is the restoration of worn parts to original dimensions. Frequently the restored parts have better corrosion and wear characteristics than the original ones [Ducos (1985)]. The reclamation of large parts such as extruder screw, vanes, turbine blades, engine valves (especially big diesel engines), and rail train car wheels are commonly carried out using standard PTA technology. Micro-PTA which meet requirements of the meso-sized fabrication are used for the repair of small parts and high value components.

The majority of the substrate materials used are steels or other ferro-alloys, although with the increase in use of lighter metals for reducing component weight, coatings on aluminum or magnesium alloys are becoming more important. Light metals, on the other hand, tend to have considerably higher thermal diffusivities (9.8×10^{-2} m^2/s for Al and 8.77×10^{-2} m^2/s for Mg) compared to that of steel AISI 1010 (1.88×10^{-5} m^2/s) resulting in a broad heating zone, which is not easy to control as the substrate temperature approaches its melting point.

PTA coatings are used in automotive industry, petroleum, chemical industries, and mining industries, where slurries are used. Micro-PTA coatings are also used with electrical and electronic industries, because very thick (up to 10 mm or more) copper coatings can be sprayed. When applied on powerful computer systems, they improve their cooling and achieve a good heat distribution.

12.5.1 Metals and Alloys

Plasma transferred arc (PTA) weld surfacing has attracted increasing attention for deposition of wear, corrosion, and heat resistance materials at high deposition rates and low heat input to the substrate [Hou et al. (2006)]. In general, coatings consist of a Fe-Cr or Fe-Cr-Ni alloys with the addition of either a refractory metal such as W, Mo, Nb, Ta, or B, Si, and C [DuMola and Heath (1997)]. The most widely used wear-resistant coatings are Fe-Cr-Mo-C (e.g., for equipment in the construction and mining industries) or Co-Cr-W-C for wear with better corrosion resistance (e.g., food processing knives, drills, valves). Stellite coatings of valve seats are also widely used. Alloys of Fe-Cr-V-C-B have excellent wear properties and are more economical than some of the cobalt or nickel-based alloys, with the hardness attributed to the formation of carbo-borides.

Other alloys that can form hard phases during spraying and solidification or after treatment are also used. For example, Fe-C-Cr-Cu coatings forming carbides upon spraying and ε-Cu phase upon treatment at 773 K for 35 h, or boride layers on AISI 1018 steel developed using the PTA alloying technique. Hou Q.Y. et al. (2006) have deposited by PTA (210–215 A) spherical particles (75–180 μm), with the chemical composition (C-1.4, Si-1.45, Cr-29.5, Fe-3, Ni-3, W-8.25, Mo-1, Co-Bal) on substrates 200 × 35 × 20 mm annealed low carbon steel plates containing 0.12 wt.% carbon and which have not been preheated before PTA treatment. They also studied aging effects on the structure and wear resistance of the cobalt-based PTA layer. They found that the As-welded coating consisted of a cobalt-based solid solution with face-centered cubic crystal structure and hexagonal (Cr, Fe)$7C_3$. Unfortunately, there were lots of stacking faults existing in the cobalt-based solid solution. After aging at 600 °C for 60 h, precipitates of other carbide $M_{23}C_6$ with face-centered cubic crystal structure were formed. While the precipitation of this carbide can in principle increase the hardness, their course microstructure and the change in the morphology of the coating led to the increase of the wear weight loss.

The addition of molybdenum (6 wt. %) on nickel-based alloy coatings obtained by PTA was studied by Hou Q.Y. et al. (2007). The morphology of Cr-rich carbides observed in the inter-dendritic region of the nickel-based alloy coating changed from plate-like to net-like, as well as the refinement of Ni-rich dendrites because of this addition. The weight fraction of Cr-rich carbides increased from 36 wt. % to 45 wt. %. The wear resistance of the modified nickel-based alloy coating increased by 47.2%. The microstructural change and phase contents variation were responsible for the improvement of the wear resistance.

Hou Q.Y. et al. (2007) deposited FeCrBSi alloy powders without and with 2–6 wt. % Mo on steel using plasma transferred arc (PTA). The results showed that the Mo-free coating consisted of γ (Fe, Ni), $M_7(C, B)_3$, and $(Fe, Cr)_2B$ phases. Adding Mo leads to the formation of $M_{23}(C, B)_6$, $Mo_2(B, C)$, and $Fe_3Mo_3(C, B)$ phases, in addition to the phases existed in the Mo-free coating. A hypoeutectic microstructure was seen in the Mo-free and 2 wt. % Mo-added coatings. Increasing Mo addition to 4 wt.% or 6 wt.%, a hypereutectic microstructure was obtained. The microstructure of the Mo-free coating was refined after adding 2–6 wt.% Mo. The finest microstructure was obtained in the 4 wt. % Mo-added coating. The thermal shock resistance of the Mo-free coating was improved after adding 2–6 wt.% Mo. The best abrasive wear resistance and thermal shock resistance were obtained in the 4 wt. % Mo-added coating.

Liu Y.-F. et al. (2006) deposited wear-resistant Fe_2TiSi reinforced composite coating with a microstructure consisting of fine Fe_2TiSi primary dendrites uniformly distributed in the super fine γ-Fe/Ti_5Si_3 eutectic matrix was in situ fabricated on a substrate of 0.20 wt. %C plain low carbon steel substrate by the plasma transferred arc (PTA) cladding process using Fe-Ti-Si-Cr powders blend as the precursor material. The mixed powder blend can be directly fed into the plasma. Wear-resistant Fe_2TiSi/γ-Fe/Ti_5Si_3 multi-phase composite coating was fabricated on the carbon steel substrate. Microstructure of the coating consisted of fine primary Fe_2TiSi dendrites uniformly distributed in the super fine γ-Fe/Ti_5Si_3 eutectic matrix. A small amount of Ti_2N course particles was scattered in some local area of the coating. The Fe_2TiSi/γ-Fe/Ti_5Si_3 composite coating has excellent abrasive and adhesive wear resistance under dry sliding wear test conditions at room temperature.

Guoqing et al. (2013) studied microstructure and wear properties of nickel-based surfacing deposited by PTA. The chemical composition of the Ni-based particles was composed of Fe 3.0.5, Cr 10.47, Si 3.87, C 0.48, B 2.35, and Ni bal. (wt. %). The coating on AISI 304 L substrate was obtained by using the PTAW process. The As-deposited coating was composed of Ni-rich γ (Ni, Fe) phase, Cr_7C_3, CrB, Cr_3C_2, $M_{23}C_6$, Ni_3B, and Ni_3Si. At the applied load of 120 N, the wear rate was almost twice than the rates under loads of 30 N and 70 N. The main wear mechanism varied with the wearing time and the applied load. At the initial stage of the wear test, the wear mechanism was abrasive wear under low load and adhesive wear under high load. After long-time wearing, the wear mechanisms were adhesive wear and oxidation wear under low load, and fatigue wear appeared under high load.

Liyanage et al. (2010 studied the influence of alloy chemistry on microstructure and properties in NiCrBSi overlay coatings deposited by plasma transferred arc welding. Two alloys with slightly different percentages of species were used. It was found that the hardness of a typical NiCrBSi alloy deposit was controlled not only by the number of Cr-rich particles present but also by the volume fraction of the inter-dendritic phase. The inter-dendritic phase was shown to exhibit high hardness of about 860 HV relative to the primary dendritic phase, which had a hardness of 405 HV. Since the volume fraction of the inter-dendritic phases is higher for the harder alloy (~55% in Alloy B), it significantly contributes to the overall properties of the deposit. Although there was only a minor increase in Cr, C, and B content in Alloy B, this led to a large increase in the number of Cr-particles from 1.5 to about 15 vol.% between the two alloys examined. Ternary phase diagrams suggest that the addition of Fe or Si will decrease the solubility of Cr in Ni; however no significant change Cr segregation was observed in the alloy compositions examined. It was also found that boron segregated to the inter-dendritic regions in both alloys and promoted the formation of Ni_3B and CrB. Microhardness testing revealed that the primary Ni dendrite, inter-dendritic, and Cr-particle phases had average hardness values of 405, 860, and 1200 HV, respectively. An increase in the volume fraction of hard eutectics and Cr-particles led to a substantial increase in hardness and wear resistance.

Ozel et al. (2008) coated NiTi powder mixture on the surface of an austenitic stainless steel (AISI 304) by plasma transferred arc (PTA). Thickness of coating increased with current density. No cracks or pores were detected in the interface. Higher arc current densities caused a coating layer poor in NiTi alloy. Secondary phases such as Cr_2Fe_7Ni, Fe_7Cr_2Ni and Ni_3Ti are also formed in the coating layer.

Sigolo et al. (2016) tested the wear resistance of coatings of boron-modified stainless steels deposited by PTA. The deposition was carried out on AISI 4140 steel substrate. Microstructural characterization revealed dendritic growth in both cases; however, the number of borides formed was quite different, around 14% for super-martensitic with 1 wt. % B and 32% for super-duplex with 3 wt.% B. Thermodynamic calculations were in accordance with the experimental results. In dry sand/rubber wheel, the volume loss of quenched and tempered AISI 4140 was superior to super-martensitic steel with 1 wt.% B; nonetheless it was comparable to super-duplex steel with 3 wt.% B. The formations of hard borides increased both the hardness and overall wear resistance of boron-modified stainless steels

Lu et al. (2011) produced functionally graded coatings by plasma transferred arc centrifugal cladding. The torch (320 A-40 to 50 V) was moved axially inside the rotating cylinder to be coated (80 mm in internal diameter with wall 5 mm thick). Fe–Cr–M–C (M = Mo, W) powders were selected as the powder to fabricate functionally graded coating on the internal walls of cylinders. Wear resistance of the graded coating could be improved by around 18 times compared with the plain cylindrical substrate.

[Zhao and Liu (2006)] manufactured structural Ni-based super alloy (GH163) by PTA on a carbon steel (A3) substrate. The deposited samples exhibited a fine and homogenous cellular dendrite structure with a stronger crystallographic orientation along <001> direction. After ageing treatment, γ′ phase and two types of metal carbides (i.e., MC and $M_{23}C_6$) with a size of 20–30 and 50–100 nm, respectively, precipitated. γ' phase was mainly located inside the grains and appeared perfectly coherent in relationship with γ matrix. On the other hand, metal carbides mainly precipitated at grain boundaries.

d'Oliveira et al. (2006) evaluated the effect of pulsed current on high carbon cobalt alloy deposited by PTA on carbon and stainless steel. Results showed that the use of pulsed current leads to a finer microstructure, higher

hardness, and lower dilution. The role of the substrate steel depended on the set of processing parameters used, but for a same set of parameters, it determined microstructural features of the coatings. Pulsed current processing resulted on finer and more homogenous solidification structures and lower dilution levels and as a consequence on coatings exhibiting higher hardness.

Iakovou et al. (2002) boride the surface of a tool steel using boron powder and PTA. It was shown that this method is an easy and effective technique in producing uniform alloyed layers with a thickness of about 1.5 mm and a hardness between 1000 and 1300 HV. The microstructure of the borided surfaces consists of primary Fe_2B-type borides and a eutectic mixture of borides and martensite. Some cracks were observed in the eutectic regions but they did not seem to critically affect the behavior of the coatings in sliding wear. The wear rate of pin on disc tests is primarily affected by the applied load, and it lies between 10^{-5} mm^3/m for low loads and 10^{-2} mm^3/m for high loads. Two distinct regimes of mild and severe wear were obtained separated by a critical load. Mild wear was due to the load supporting effect of borides, and severe wear was due to their breakage above a critical load. The wear rate was not significantly affected by the sliding velocity and was consistent with the friction coefficient. The friction coefficient varied from 0.13 to 0.23 and depended strongly on the oxidation status of the wear track. The sliding velocity affected the sliding distance where the coefficient of friction reached equilibrium.

[Kim et al. (2003)] Pin-on-disc sliding wear tests were conducted in molten Zn–0.18%Al (wt. %) bath at 470 ″C to evaluate the high temperature wear performance of cobalt-based alloys and their carbide composites processed by PTA weld-surfacing technique. The main results are as follows:

- Wear performances of Stellite 6 and Tribaloy 800 with carbide composite materials are not good when coupled with same materials although their hardnesses are higher and their microstructures are finer than those of Stellite 6 and Tribaloy 800.
- Wear test results from different materials combination show that as the hardness of the counterpart disk is increased, the wear rate of the Tribaloy 800 pin is usually increased.
- Although overall wear rates of both pin and disc are similar between Stellite 6 and Tribaloy 800, wear mechanism is quite different. While harder eutectic carbides are broken and detached in Stellite 6, softer matrix is preferentially damaged without pulling out of harder phases in Tribaloy 800 during the wear testing.

Pukasiewicz et al. (2014) studied cavitation wear induced by the collapse of vapor bubbles in a fluid (usually because of a localized pressure fluctuation) which leads to mass loss as a result of fatigue caused by the successive impacts generated by the collapse of bubbles near the surface of a material. They recalled that surface re-melting is an important technique for modifying the microstructure of thermally sprayed coatings as it reduces the porosity and promotes a metallurgical bond between substrate and coating. In their work, an Fe-Mn-Cr-Si alloy was deposited by arc spraying and then re-melted by a plasma-transferred arc process. The base metal was a soft martensitic stainless steel. The use of a lower mean current and a pulsed arc reduced the thickness of the heat-affected zone. In specimens re-melted with constant arc current, dendrites were aligned parallel to the path followed by the plasma torch; while in those re-melted with a pulsed plasma arc, the alignment of the microstructure was disrupted. The use of a higher peak current in pulsed-current plasma transferred arc re-melting reduced mass loss due to cavitation. Fe-Mn-Cr-Si coatings exhibited cavitation-induced hardening, with martensite formation during cavitation tests.

Bhargava et al. (2013) investigated the deposition of Inconel-625 using laser rapid manufacturing (LRM) and plasma transferred arc (PTA) deposition in individual and tandem mode. LRM has advantages in terms of dimensional accuracy, improved mechanical properties, finer process control, reduced heat input, and lower thermal distortion, while PTA scores more in terms of lower initial investment, lower running cost, and higher deposition rate. A number of samples were deposited with both processes at different parameters such as power, scan speed, and powder feed rate. They were subjected to tensile test, adhesion-cohesion test, impact test, and microhardness measurement. The results of individual tests showed the comparable mechanical properties with ±20% variation. The mixed dendritic-cellular and dendritic-columnar microstructures were respectively observed for LRM and PTA deposits with a distinct interface for the case of tandem deposition. The interface strength of tandem deposits was evaluated employing adhesion-cohesion test, and it was found to be (325 ± 35) MPa. The study confirmed the viability of LRM and PTA deposition in tandem for hybrid manufacturing. Figure 12.37a presents typical microstructure observed in LRM deposits of Inconel-625. The direction of dendrite growth was along the direction of deposition. Figure 12.37b presents the typical microstructure observed in PTA deposited Inconel-625 samples. For hybrid mode of material deposition, LRM and PTA processes were used to deposit material in successive tracks, and the interface was also studied. Figure 12.37c presents the microstructure of the deposit in tandem mode. Two distinct microstructures were observed in the regions deposited with different processes. The coarser columnar dendritic structure was observed in the region of PTA deposits, while mixed columnar and cellular dendrites were observed in the region of laser deposits. It was found that the maximum deposition rates

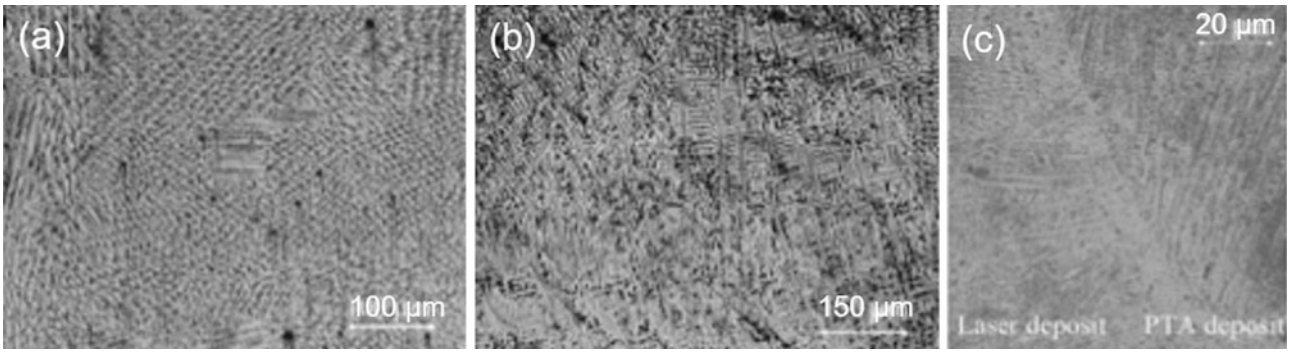

Fig. 12.37 Effect of the deposition technique on the microstructure of Inconel-625 deposited on steel substrate using (**a**) LRM, (**b**) PTA deposit, (**c**) LMR/PTA in tandem showing the interface between the two coatings. [Bhargava et al. (2013)]

were 12 g/min and 60 g/min for LRM and PTA process, respectively.

Tigrinho et al. (2007) studied the potential of PTA hardfacing beyond the surface welding of superalloys. This work evaluated low carbon steel surface modification by PTA deposition of fine WCoC carbides and mixtures of Fe powders and 5–35 wt% carbides. PTA processing allowed for the dissolution of carbides confirmed by X-ray diffraction, leading to homogeneous microstructures. Microstructures' morphology reaches typical dendritic solidification structure upon the WCoC content. Surface soundness depended on powder preparation and composition. Sound surfaces exhibiting hardness up to 700 HV were obtained for the 35 wt% WCoC powder mixture.

Reinaldo and D'Oliveira (2013) gathered microstructure data from the literature and analyzed Colmonoy 6 (NiCrSiB) which is a Ni-based alloy coating deposited by PTA hardfacing. This Ni-based alloy is recognized for its superior mechanical properties, attributed to the presence of a dispersion of hard carbides and borides, which is strongly dependent on processing technique. The aim of authors was to determine the influence of PTA deposition parameters and substrate chemical composition on NiCrSiB coating characteristics. Coatings were characterized in terms of their hardness, dilution, and microstructure, as well as mass loss during abrasive sliding wear tests. The results showed that coating performance is strongly dependent on the chemical composition of the substrate. Carbon steel substrate yielded coatings with greater wear resistance. Processing parameters also alter the performance of coatings with lower current and lower travel speeds resulting in reduced mass loss.

12.5.2 Composite Coatings Doped with Ceramics

There are fundamentally two approaches for obtaining a wear- and corrosion-resistant coating. In one approach, a metal alloy is deposited and during the cooling from the molten state hard phases or carbides precipitate. The other approach consists of adding carbides as hard phases into a suitable metal matrix. The addition of carbides will increase the abrasive and erosive wear resistance but may reduce the corrosion resistance. In most cases powder mixtures are used for the deposition, for example [Gallo et al. (2013)], blended powders of pure iron (~120 µm), carbon (~15 µm), titanium (~15 µm), and FeSi master alloy (~100 µm) and gray cast iron (FeSiMnC; ~125 µm). The powders were mixed thoroughly, dried at 150 °C for 1 h, and loaded into the hopper of a fluidized bed powder feeder. Powders with mean size around 150 µm can also be prepared and sprayed. Hou et al. (2015b) mixed the powders in a planetary ball mill, which were then made into a pasty mass in an agate mortar using a chemical binder. The obtained pasty mass was spread on a carbon steel plate to form prefabricated layers with thickness of about 3 mm, dried in an oven to vaporize the chemical binder before being processed by PTA surfacing to form thick coatings.

An example of such a coating on the tooth of an excavator is presented in Fig. 12.38a, with a cross section of the coating (Fig. 12.38b) showing a good dispersion of WC irregular particles (with no evidence of melting and spheroidizing).

Huang Z. et al. (2008) have deposited nickel-based alloy (C-0.6, Si-4.0, B-4.5, Cr-14, Fe-14.8, Ni-Bal) with 30 wt.% chromic carbide (Cr_3C_2) particles on Q235-carbon steel (including 0.12 wt.% C) substrate (200 × 35 × 20 mm^3) using PTA. They found that the γ(Ni, Fe), M7(C,B)3, Ni4B3, and (Cr,Fe)2B phases existed in the Cr_3C_2-free nickel-based alloy coating obtained by PTA process. The addition of 30 wt.% Cr_3C_2 particles led to the existing of Cr_3C_2 phase and the microstructure changing from hypoeutectic structure into hypereutectic structure. The average microhardness of the Cr_3C_2-free nickel-based alloy coating increased by 450–500 HV after the addition of 30 wt.% Cr_3C_2 particles. The partial dissolution of Cr_3C_2 particles led to the enrichment of carbon and chromium in the molten pool and hence caused the formation of more chromium-rich carbides after the solidification process.

Fig. 12.38 (**a**) PTA coated tooth of excavator with Ni base coating + WC (25 kg/h). (**b**) cross section of the coating (courtesy of Castolin)

Hou et al. (2005) studied the microstructure and wear characteristics of Co-Cr-W series cobalt-based alloys deposited by PTA. A cobalt-based solid solution with face-centered cubic crystal structure and hexagonal $(Cr,Fe)_7C_3$ was obtained. There were lots of stacking defaults existing in the cobalt-based solid solution. After aging at 600 °C for 60 h, the precipitation of carbide $M_{23}C_6$ increased the hardness, but unfortunately the course of the microstructure and the change of the morphology led to the increase of the wear weight loss.

Wear resistance has also been improved by adding alumina particles in the PTA deposit. Hou et al. (2011) deposited nickel-based alloys powders with and without nano-α-Al_2O_3 addition on Q235A low carbon steel using PTA. Results show that the typical hypoeutectic microstructure and the component segregation exist in the Al_2O_3-free coating consisting of γ (Ni, Fe), $(Fe, Cr)_7C_3$, and $(Fe, Cr)_2B$ phases. The addition 0.8 wt. % nano-Al_2O_3 particles does not change the hypoeutectic microstructure characteristics of the Al_2O_3-free coating, though it refines its microstructure and decreases its component segregation. The nano-Al_2O_3 particles are mainly tetragonal lattice (γ-Al_2O_3). The substructure of the Al_2O_3-free coating is mainly dislocation. Adding nano-Al_2O_3 particles promotes to form stacking faults and dislocation cell wall. The sliding wear resistance of the Al_2O_3-added coating is higher than that of the Al_2O_3-free coating.

Hou et al. (2015a) prefabricated W-based composite powders containing NbC, TiC, and VC. PTA then processed these powders to form thick W-NbC, W-TiC, and W–VC coatings on a low carbon steel (0.454 wt. %) substrate. The best ability to resist elastic strain-to-failure and the highest toughness were obtained with the W-VC coating.

Guoqing et al. (2013) deposited nickel-based alloy coating on AISI 304 L stainless steel substrate using plasma transferred arc welding (PTAW). Microstructure and tribological characteristics of the coating were studied. The as deposited microstructure mainly consisted of Ni-rich γ (Ni, Fe) phase, Cr_7C_3, CrB, Cr_3C_2, $M_{23}C_6$, Ni_3B, and Ni_3Si. Compared with that of the 304 L stainless steel substrate, the wear resistance of the coating was greatly improved. The wear test demonstrated that the wear mechanism depended on wearing time and applied load. When the wearing time was short, the wear mechanism was abrasive wear under low load and adhesive wear under high load. When the time was relatively long, the wear mechanisms were adhesive wear and oxidation wear under low load; fatigue wear appeared under high load.

Rokanopoulou et al. (2014) studied the use of the more thermodynamically stable ceramic, aluminum oxide, in order to reinforce the surface of the austenitic–ferritic steel SAF 2205 by PTA technique. The austenitic–ferritic microstructure was maintained, the Al_2O_3 reinforcement particles were finely distributed, and no other micro-constituents were found, leading to enhanced tribological properties, which is not the case when carbides are used for the reinforcement.

Rokanopoulou A. et al. (2016) deposited by PTA a powder mixture of Al_2O_3, TiS_2, and Fe. During solidification, Al_2O_3 forms and Al_2TiO_5 becomes thermodynamically stable and forms on the existing Al_2O_3 particles. As the melt cools further, the solubility of sulfur in molten steel decreases and the previously formed complex oxides spontaneously act as nucleation sites for sulfides, whereas Al_2TiO_5 is reduced to Al_2O_3. The Al_2O_3 reinforcement particles are surrounded by sulfides, and thus they have better wettability by the molten stainless steel and are less detachable compared without the addition of TiS_2. These sulfides also act as lubricants.

According to Deuis et al. (1997a) at the end of 1990s, PTA surfacing had already current commercial applications against wear with mostly metal coatings doped with ceramics, mainly TiC, WC, WC-W_2C, Cr_3C_2. The applications were for nuclear industry (fluid control), automobile (piston for tractor engine), power generation (steam turbine), chemical (ball valves), mining (slurry mixing paddles), polymers (extruder screw flights), sewage treatment (conveyors screws), cement (draft fan blades), steel making (basic oxygen furnace fume hood), and mining (liner plates, slurry paddles). Moreover, potential commercial applications are in automobile (engine components), mining (ore bucket

lining), plastics (extruder screw), petroleum/chemical (protection of wear/corrosion areas), aerospace (high-temperature components, dry sliding couple system)), and heavy industry (wear components). If the hardness and wear resistance are usually significantly improved by the addition of carbides, the carbides may decompose when they are too strongly heated, e.g., in the transferred arc or in a high-temperature molten metal pool. Special injection techniques can remedy this situation. Some dissolved carbides will form mixed carbide hard phases in the coating.

As one of the most popular carbide addition giving the highest hardness is tungsten carbide [Lugscheider and Ait-Mekideche (1991)], which can be added (a) in form of macro-crystalline WC, large-enough particles that undergo minimal decomposition (although too large particles tend to settle at the bottom of the weld pool); (b) in form of fused tungsten carbide (FTC), an eutectic mixture of WC/W2C; and (c) in form of sintered WC in a cobalt. Other carbides include TiC, VC, NbC, or mixed carbides (W,Ti)C [Saltzmann (1986)]. Different carbides are used with different matrix materials, e.g., (V,W)C, NbC, TiC with a Fe-Cr-C matrix, (W,Ti)C, and W_2C with a Co-Cr-W-C matrix. For example TiC-W-Cr powders formed complex structure comprising primary austenite, martensite, an eutectic of $(Fe, Cr)_7C_3$ carbide and austenite as well as the uniformly distributed un-melted TiC particles. Un-dissolved Cr_3C_2 particles and chromium-rich carbides enhanced the hardness and wear resistance of the nickel-based alloy with 30 wt. % Cr_3C_2 within a coating deposited by the PTA process [Huang Z. et al. (2008)]. Nanometer-sized Al_2O_3 particles in nickel-based alloy powders promoted the formation of stacking faults and dislocation cell wall. The sliding wear resistance of the coating with Al_2O_3 added was higher than that of the Al_2O_3-free coating [Shi et al. (2011)].

[Kim et al. (2002)] PTA deposited two Fe-based gas atomized powders, proposed to as metamorphic alloys (Armacor M and Armacor C). The microstructures of both of them were mainly composed of Fe-based solid solution and chromium boride precipitates. However, the hardness and the boride size of the Armacor M were higher by about 200 HV and four times larger than those of the Armacor C, respectively. Armacor M coating exhibited better wear performance than Armacor C one.

Liu et al. (2007) deposited by PTA wear-resistant Fe_2TiSi reinforced composite coating by using a cladding process with Fe-Ti-Si-Cr powders blend, the substrate being plain low carbon steel. Under dry sliding wear conditions at an ambient temperature, the PTA clad Fe_2TiSi/γ-Fe/Ti_5Si_3 composite coating exhibited excellent abrasive and adhesive wear resistance.

[Skarvelis P. and G. D. Papadimitriou (2009a)] used PTA to produce composite coatings based on co-melting of MoS2, TiC, and iron ingredients, in an attempt to obtain wear-resistant layers with self-lubricating properties. The wear tests performed with a pin-on-disk apparatus have shown that the coatings which were produced using both TiC and MoS_2 ingredients exhibited improved friction coefficients and lower wear rates in comparison to the steel substrate as well as to the composite containing TiC, but exempted from MoS_2.

Demian C. et al. (2016) deposited by PTA yttria stabilized zirconia (YSZ) filler with two different particle sizes into NiCrAlY (respectively, 10 and 20 vol. %) and metal matrix composite (MMC) to develop cermet coatings on medium carbon steel type AISI 1035 25 mm thick. The YSZ filler in a concentration of 20 vol.% into the NiCrAlY powder was the optimal choice. The mixtures were mechanically blended and dried at a temperature of about 120 °C for 24 h. The substrate surface was prepared by grinding and preheating in an open-air furnace at temperatures over 365 °C, increasing with the YSZ content. When using high currents of transferred arc, good metallurgical bonding between the coating and substrate were obtained in both cases. Finally, it was found out that cermet coatings including small particles of YSZ filler in a concentration of 20 vol.% into a NiCrAlY matrix were the optimal choice among all tested in the presented conditions.

Fisher et al. (2013) recall that it is common to apply tungsten carbide-based composite overlays to improve the reliability and extend service lives of equipment and components, for example, to remove bitumen from oil sands deposits. The performance of the applied overlays is largely dependent on the selection of the carbide type and the wear environment. Evaluated overlays containing macro-crystalline, angular eutectic, and spherical eutectic tungsten carbides are deposited by PTA. They used angular WC, angular WC/W_2C, and spherical WC/W_2C. The three overlays contained relatively homogeneous distributions of primary tungsten carbide particles in the nickel-based matrix alloys. As an example, Fig. 12.39 shows a micrograph of the sprayed 6030 M overlay. The carbides are well distributed, and there is little or no evidence of primary carbide dissolution.

- Eutectic (WC/W_2C) primary carbides are more susceptible to dissolution due to heat input upon deposition. The levels of secondary carbide formation for the mono-crystalline (WC)-containing 6030 M overlay were significantly lower.
- Abrasion by sands sized less than 350 μm (50 mesh) preferentially removed the matrix alloy in the MMC.
- The abrasion rates recorded by the WC-MMC were related to the size of the abrasive and the associated applied load. Increases in these two factors produced higher levels of mass loss due to primary carbide fracturing.

Gallo et al. (2014) studied the in situ synthesis of titanium carbides in iron alloys using PTA. They showed that it was possible to convert synthetic rutile (TiO_2) into TiC by a

reactive deposition process with a PTA technique. The TiC precursors, consisting of graphite (C) and synthetic rutile (TiO_2) in a 6:1 molar ratio, were easily introduced in the blend with iron powder up to a concentration of 30 wt.%. The addition of 1 wt.% of an alkali salt resulted in marked increases in the volume fraction of TiC precipitates in the overlays. They showed that silicon and manganese on the TiC precipitates had a significant effect on TiC size and morphology. However, an increase in the volume fraction of TiC required additional processing, more efficient ways to introduce the precursors and effective extraction of the gas produced in the reaction.

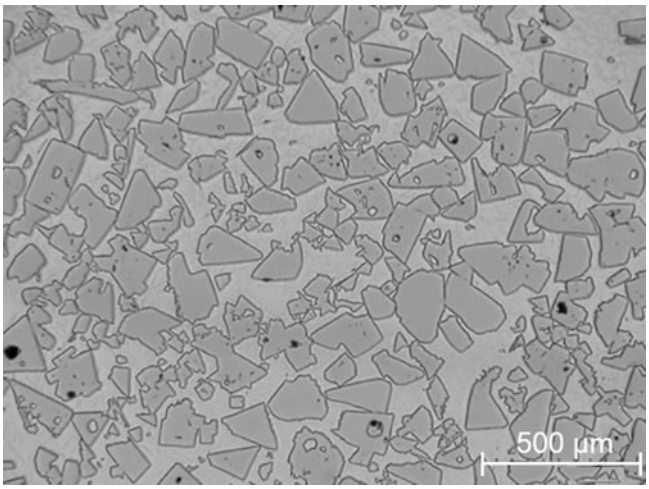

Fig. 12.39 Micrograph of the 6030 M overlay, showing the distribution of WC particles in the Ni-alloy matrix. Magnification 140x [Fisher et al. (2013)]

Gallo et al. (2014) evaluated the in situ synthesis of TiC-Fe composite overlays for low-cost TiO_2 precursors using PTA. Mild steel AISI 1020 was selected as a substrate with slabs 100 mm long, 32 mm wide, and 5 mm thick. Three different powder mixtures were used for the deposition: Fe + C + Ti, FeSi + C + Ti and FeSiMnC + Ti. Results showed that:

Fe-TiC composite overlays can be produced by in situ synthesis:

- The morphology of TiC precipitates was affected by the chemical composition of the iron matrix. Additions of silicon reduced the occurrence of script carbides and manganese hinders dendritic growth.
- The size and volume fraction of TiC precipitates in the FeSiMn matrix increased with increasing heat input and decreasing cooling rate. A coarsening and softening of the microstructure of the matrix accompanied this.
- The FeSiMn matrix promoted the precipitation of spheroidal or faceted TiC carbides, evenly distributed in the matrix, under a wide range of deposition conditions.

Figure 12.40 illustrates the typical microstructures observed in the overlays. Figure 12.40a corresponds to the pure Fe overlay, produced for reference purposes, and

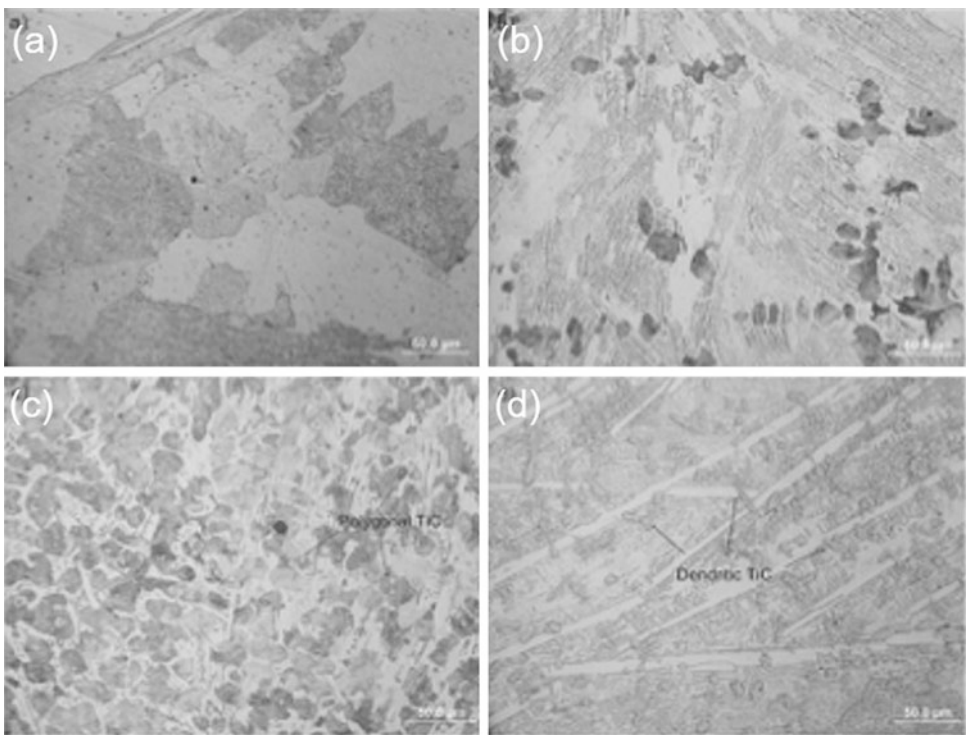

Fig. 12.40 Optical micrographs of overlays produced with (**a**) Fe, (**b**) Fe + C, (**c**) Fe + 20MM (TiO2 + C), and (**d**) Fe + 30MM (TiO2 + C) with alkali salt. MM mechanically mixed TiC precursors (TiO + C) [Gallo S. C. et al. (2014)]

exhibits the characteristic ferritic microstructure. Figure 12.40b shows the microstructure of the second overlay produced for reference purposes, which consisted of the pure Fe powder blended with 5 wt.% graphite. The carbon content of this specimen was equivalent to the carbon content of sample Fe + 10MM(TiO_2 + C). The microstructure of this overlay was typically martensitic-pearlitic, with a high-volume fraction of cementite (lighter phase in Fig. 12.40b). This reflects the high carbon content of the alloy resulting from the addition of graphite to the powder blend. The two reference samples provided a basis for the subsequent study. The typical microstructure of overlays produced with powder blends containing TiO_2 and graphite consisted of a pearlitic matrix with an even dispersion of precipitates. The addition of TiO_2 produced an apparent reduction in the carbon content of the iron matrix of the overlays, which becomes evident from the lower volume fraction of cementite in the typical microstructure of overlays produced with powder blends containing TiO_2 and graphite consisted of a pearlitic matrix with an even dispersion of precipitates. The addition of TiO_2 produced an apparent reduction in the carbon content of the iron matrix of the overlays, which becomes evident from the lower volume fraction of cementite in Fig. 12.40c and d.

Bourithis et al. (2002) produced coatings with boride, 1–1.5 mm thick, on AISI 1018 with different boron contents. The deposited powder contained C 4.1%, Cr 33.4%, Mo 12.5%, TiC 50% (wt %). The PTA alloying process was successful in producing MMC layers of 0.8–1 mm thickness on the surface of construction carbon steel. The microhardness of the alloyed surface was stable and attained values between 850 and 900 HV. The microstructure of the MMC layer consisted of a fine martensitic matrix with retained austenite and TiC carbides as reinforcing particles. The wear rate of the MMC is approximately 10^{-3} mm^3/m and that of the plain steel used as base metal is of the order of 10^{-2} to 10^{-1} mm^3/m, i.e., 10–100 times greater. The wear mechanism of the alloyed surface depends on the operating conditions. The dominant wear mechanism for low sliding speeds is plastic deformation. At higher sliding speeds an oxidation mechanism predominates. In particular a transition from mild to severe oxidation is observed when the applied load exceeds a certain value (between 29.4 and 39.2 N).

Liu et al. (2006) used Fe-Cr-C-Ni powder blends to deposit PTA coatings on steel substrate (0.45 wt.%.C). Results showed that the composite coating consisted of primary $(Cr,Fe)_7C_3$ as the reinforcing phase and interdendritic $(CrFe)_7C_3/\gamma Fe$ eutectics as the matrix. The composite coating was metallurgically bonded to the substrate. The $(CrFe)_7C_3$ carbide reinforced composite coating has high hardness (around 440 HV) and excellent wear resistance under dry sliding wear test conditions, the worn surface of the carbide reinforced composite coating being smooth with only slight scratches.

Werry et al. (2016) studied multiscale-structured composite coatings by plasma-transferred arc for nuclear applications. PTA coatings of nickel-based alloys reinforced with alumina particles were deposited on 316 L stainless steel substrates. Metallic and alumina powders were oven dried at 80 °C for 5 h. Then, they were mixed into a stirrer with attrition balls (Ø 0.6 mm) for 12 h and sieved through 400 μm mesh sieve to remove the attrition balls and the largest alumina agglomerates. Under the conditions of this study, the addition of alumina particles resulted in a refinement of coating microstructure and the improvement of their resistance to abrasive wear. However, it does not bring about any change in coating micro-hardness.

Hung et al. (2006) used the PTA technique to overlay NbC reinforcing particles on the surface of commercially pure Ti in order to investigate the microstructural features of the over-layer and the interface between the over-layer and base metal by changing the overlaying current. The results indicated that the matrix phase of the over-layer was α-Ti containing about 10 at.% Nb and 1 at.% C. NbC and precipitated TiC produced by dissolved NbC reacted with Ti dispersed in the matrix. The microstructure of the cross-section of the over-layer (from surface to base metal), which was composed of α-Ti, can be separated into three layers: an upper over-layer with TiC, a middle over-layer with TiC and NbC, and a lower over-layer (interfacial layer and Heat Affected Zone, HAZ). Due to solidification beginning at the interface and the effect of dilution, the TiC in the interfacial layer was finer. Owing to faster solidification under low-current conditions, the TiC particles were finer than under high-current conditions. Also, dendritic TiC under a low-current in the upper over-layer was also finer than under a high current. Meanwhile, TiC precipitate that resulted from heterogeneous nucleation and Gibbs' free energy was also found around NbC. This NbC diffusion layer between TiC and NbC may have been βNb_2C phase.

Yuan and Li (2014) studied the fabrication of high-volume fraction (HVF) M_7C_3 (M = Cr, Fe) reinforced Fe-based composite coating on ASTM A36 steel plate using plasma transferred arc (PTA) welding. The results showed that the volume fraction of carbide M_7C_3 was more than 60%, and the relative wear resistance of the coating tested on a block-on-ring dry sliding tester at constant load (100 N) and variable loads (from 100 to 300 N) respectively was about 9 and 14 times higher than that of non-reinforced α-Fe coating. In addition, under constant load condition the friction coefficients (FCs) of two coatings increased first and then decreased with increasing sliding distance. However, under variable loads' condition, the FCs of non-reinforced α-Fe based coating increased gradually, while that of HVF M7C3 reinforced coating decreased as the load exceeded 220 N. The worn surface of non-reinforced α-Fe based coating was easily deformed and grooved, while that of the HVF

M7C3 reinforced coating was difficult to be deformed and grooved. Carbide Cr_3C_2 can act as substrate for the nucleation of M_7C_3. The mass loss and FCs of HVF M_7C_3 reinforced coating are lower than that of non-reinforced α-Fe coating under the conditions of constant and variable loads dry sliding wear. The main wear mechanism of HVF M_7C_3 reinforced coatings is micro-cutting, abrasive wear, and oxidation wear. Micro-cracks and spalling pits formed on the worn surfaces of carbide M_7C_3 particles as the loads increased from 100 to 300 N. The α-Fe matrix can prevent cracks extending in the coating and no M7C3 particle has been pulled out the matrix due to its long rod shape and high interface binding force derived from the in situ reaction.

Werry et al. (2016) studied the replacement in nuclear plants of hard-facing Stellite, a cobalt-based alloy, on parts of the piping system in connection with the reactor that has been investigated since the late 1960s. Various Fe-based or Ni-based alloys, Co-free or with a low content of Co, have been developed but with mechanical properties generally lower than that of Stellite. The fourth-generation nuclear plants impose additional or more stringent requirements for hard-facing materials. Plasma transferred arc (PTA) coatings of cobalt-free nickel-based alloys with the addition of sub-micrometric or micrometric alumina particles are thought to be a potential solution for tribological applications in the primary system of sodium-cooled fast reactors. In this study, PTA coatings of nickel-based alloys reinforced with alumina particles were deposited on 316 L stainless steel substrates. Under the conditions of this study, the addition of alumina particles resulted in a refinement of coating microstructure and the improvement of their resistance to abrasive wear. However, it does not bring about any change in coating microhardness.

Shi et al. (2012) subjected TiC-Cr overlay formed by plasma transferred arc to tempering treatments at 473, 673, and 873 K for 2 h, respectively. Microstructure investigation by SEM and TEM, microhardness, and fatigue test were performed on As-deposited condition and after tempering. Evolution of microstructure as well as its relationship with microhardness and fatigue property of coating was described. The results suggest that both microhardness and fatigue strength could be improved by tempering at 473 K; however, further elevation of the temperature directs degradation.

12.5.3 Slurry Erosive Wear

When comparing the influence of dry and slurry erosion on HVOF coatings, it was shown that erosion rates in dry particle impact were about three orders of magnitude higher than those in slurry systems. This difference probably reflects the real erodent target impact velocities, which are mitigated in the slurry test by the water medium [Hawthorne et al. (1999)]. The erosion occurred dominantly by spalling of splats from the lamellar interfaces, spalling resulting from the propagation of cracks parallel to the interfaces between the lamellae exposed at the surface and underlying coating. The carbide particle size and content in the coating influenced significantly the erosion performance of Cr_3C_2-NiCr coatings.

Santa et al. (2009) studied in laboratory the slurry and cavitation erosion resistance of six thermal spray coatings and compared to that of an uncoated martensitic stainless steel. Nickel, chromium oxide and tungsten carbide coatings were applied by oxy fuel powder (OFP) process and chromium and tungsten carbide coatings were obtained by high-velocity oxy fuel (HVOF) process. The results showed that the slurry erosion resistance of the steel can be improved up to 16 times by the application of the thermally sprayed coatings. On the other hand, none of the coated specimens showed better cavitation resistance than the uncoated steel in the experiments.

Flores et al. (2009a) studied the erosion–corrosion behavior of two tungsten carbide (WC)- metal matrix composites (MMCs) PTA deposited. Two variations of the NiCrBSi matrix with different concentration of chromium (Cr), carbon (C), and boron (B) were evaluated with and without reinforcing hard phase. The erosion–corrosion behavior was evaluated as a function of sand concentration and temperature. To determine the influence of the mechanical degradation, the study was conducted using 1 and 5 wt.% sand concentrations. Important microstructural differences were identified between the two MMCs. Elongated precipitates rich in W and Cr were identified near the WC grains and in the matrix phase of the WC-hard overlay. Needle-like precipitates with a lower concentration of W were identified in the WC-soft overlay. For both MMCs the α-Ni phase and silicide were present in the matrix phase. The addition of WC dramatically improved the erosion–corrosion resistance of the matrix-only overlays by almost 70% when 20 °C and 1 wt.% sand loading were used. At 20 °C and 1 wt. %, sand loading erosion had a predominant impact over corrosion in the erosion–corrosion degradation mechanisms. The effects of corrosion were more evident at 65 °C and 1 wt. % solid loading. A higher degradation of the matrix phase, due to corrosion effects, left the WC grains unprotected and their degradation was more pronounced. The matrix microhardness and precipitates distribution played an important role in the erosion–corrosion resistance of the MMCs. In the zone where low impact angles were predominant, the elongated precipitates provided a better protection against sand erosion to the matrix of the WC-hard overlay compared to the protection provided by the needle-like precipitates of the WC-soft overlay.

Flores et al. (2009b) investigated the microstructure and erosion–corrosion behavior of a Fe-Cr-C overlay (FeCrC–matrix) produced by plasma transferred arc welding (PTA)

and its metal matrix composite (FeCrC–MMC). The latter was obtained by the addition of 65 wt.% of tungsten carbide. The erosion–corrosion tests (ECTs) were carried out using a submerged impinging jet. At 20 °C the FeCrC–matrix overlay showed micro-cutting and micro-plowing degradation processes followed by plastic flow. At 65 °C it suffered a higher degradation due to the selective dissolution of the dendritic structure by corrosion attack.

The removal of the matrix phase in the FeCrC–MMC was mainly by an extrusion process due to the erosive effects of the sand particles. Under the conditions of 10 g/l and 20 °C and at medium to low impact angles, the presence of intermetallic phases distributed in the ductile matrix had a beneficial effect on the erosion–corrosion resistance of the FeCrC–MMC overlay. When the severity of the erosive conditions was increased, the mechanical degradation dominated the erosion–corrosion process. At 65 °C the FeCrC–MMC overlay suffered severe corrosion attack; the effect of temperature in the corrosion behavior of the overlay under erosion–corrosion conditions was significantly higher than the effect of the sand concentration.

[Gatto et al. (2004)] analyzed the influence of PTA as a thermal treatment on the base material. They showed that structural modifications, with the generation of three different zones (melted zone, HAZ, unaffected zone), depend most on the physical effect of heat transfer and almost not on the alloys. Sample observation showed the process to be ruled mostly by physical than by chemical phenomena (for the same geometrical configuration, identical results were obtained for different materials). Optimized process parameters were found to be the same for all the deposited alloys, varying only as a function of the geometrical configuration. It was proved that the quality of the deposition was strongly determined by an optimal reciprocal positioning and movement between the torch and the part to be coated, especially for critical geometries. Specimen characterization through liquid penetration inspection, optical and scanning electron microscopy, and microhardness tests proved that process parameter optimization depends only on the geometrical configuration and not on the deposited alloy.

12.5.4 Reclamation and Resurfacing

The effects of wear and corrosion can only be retarded, but not be stopped forever and wear parts must be replaced or resurfaced. It is the same for undersize parts due to manufacturing error. The ability to apply coatings by thermal spraying with a broad spectrum of thickness, finish and composition requirements makes the different thermal spray processes ideal solutions to resurface components, avoiding their costly replacement. Restoration is performed either with the same material as the base metal or with a more corrosion- and/or wear-resistant material. However, it is better to choose coatings that can be machined. In a wide range of industrial applications, thermal coatings are used to renew components by restoring their specified dimensions and matching and sometimes improving their original performance. Very often it is possible to design a coating that meets the functional requirements of the component, and moreover offers better resistance to corrosion, oxidation, and mechanical wear than the original product. Of course, the cost of the resurfacing must be lower than that of a new part (a fraction of it). For example, this technique is particularly used for roller faces and journals, dryer drums for papermaking, pump seals (shafts and sleeves), pump housings, compressor rods, rotary airlocks and feeders, and conveyer screws [Davis J.R. Publisher (2004), Tucker R. C., Jr. Ed. (2013)].

Alberti et al. (2016) have defined the additive manufacturing, where PTA is also used. It is a process used to fabricate and repair parts that have a complex geometry or need to be functionally graded. The technique involves depositing multiple layers to produce the component. The success of the procedure depends on the deposition technique used, the parameters selected, and the alloy deposited. The deposition conditions, such as temperature and protective atmosphere, determine whether cracking and oxidation of the deposited layers occur. In their study the authors presented the potential of plasma transferred arc to produce thin walls by additive manufacturing. Two nickel-based alloys were used on an Ni-based substrate: a γ' precipitation-hardened alloy and a solid-solution-hardened alloy. During the study, the processing parameters required to produce a thin wall with each alloy were determined, and the use of preheating at 300 °C was analyzed. The results showed that the chemical composition of the alloy being processed and preheating influences the geometry of the wall. A fine dendritic solidification structure exhibiting epitaxial growth between layers was observed. The precipitation-hardened alloy showed banding of a γ' precipitate-rich region that caused oscillations in the hardness. Dilution with the substrate was the main factor affecting the hardness profile of the wall processed with the Ni-based solid solution alloy, which did not change following post-deposition heat treatment. This study has shown that sound thin walls can be successfully processed by additive manufacturing using plasma transferred arc.

Lü et al. (2013) remanufactured by PTA the thrust of engine cylinder body. The Ni15 alloy was deposited on the thrust face of the body in order to recover its dimension. In addition, the remanufacturing forming with Fe-based, Inconel 625 alloy was studied. The microstructure and hardness of the As-deposited materials were investigated. In order to control the deforming of the formed parts, the PTA current must be controlled. When the PTA current was limited to 30 A, it was called micro-plasma arc. Ni_{15} alloy was

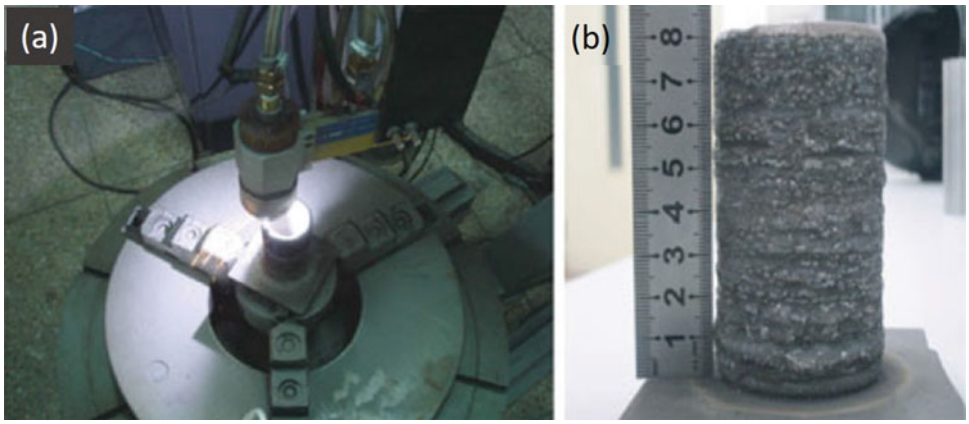

Fig. 12.41 Micro-plasma arc direct metal forming (**a**) process and (**b**) rough part [Lü Y.-H.et al. (2013)]

deposited on the thrust face of the body in order to recover its dimension. In addition, the remanufacturing

forming with Fe-based, Inconel 625 alloy was studied. The microstructure and hardness of the as-deposited materials were investigated. Figure 12.40 shows the micro-plasma arc direct metal forming process (see Fig. 12.41a) and the rough part (see Fig. 12.41b). Microhardness measurements were carried out on the transverse and longitudinal cross sections of the As-deposited Inconel 625 material. Results revealed microhardness on the transverse cross section in the range of 260–285 $HV_{0.2}$ with an obvious fluctuation.

Tigrinho et al. (2007) evaluated low carbon steel surface modification by PTA deposition of fine WCoC carbides and mixtures of Fe powders and 5–35 wt% carbides. PTA processing allowed for the dissolution of carbides confirmed by X-ray diffraction, leading to homogeneous microstructures. Sound surfaces exhibiting hardness up to 700 HV were obtained. Surfaces modified by melting Fe–35 wt% WCoC powder mixtures exhibited a typical solidification structure with a ferrite dendrites and an inter-dendritic Fe/Carbide eutectic. Increasing dilution with the steel substrate altered phase distribution and surface hardness. Surfaces modified with Fe–5 wt. % WCoC powder mixtures resulted in a slight increase hardness compared to the base steel.

According to Jhavar et al. (2014), micro-plasma transferred arc (μ-PTA) deposition process has potential to meet requirements of the meso-sized fabrication and repair of the high value components. The overall objective was to repair and/or remanufacture the defective dies and molds. An experimental setup was developed to deposit 300 μm diameter wire of AISI P20 tool steel on the substrate of the same material which is one of the most commonly used ones for making the dies and molds used for various applications. The μ-PTA deposition process was found to be capable of fabricating straight walls having total wall width of 2.45 mm and effective wall width of 2.11 mm. The deposition efficiency was found to be 87% for the maximum deposition rate of 42 g/h. The deposited wall was free from cracks, porosity, and inclusions.

Jhavar et al. (2016) deployed an automatic micro-plasma deposition setup to deposit a wire of 300 μm of AISI P20 tool steel on the substrate of same material for the potential application in remanufacturing of the die and mold surface. Bead-on-plate trials were conducted to deposit single bead geometry at various processing parameters. A set of parameters leading to reproducible regular and smooth single bead geometry were identified and used to prepare a thin wall for mechanical testing. In their study, plasma power of 500 W, travel speed of 80 mm/min, and wire feed rate of 1275 mm/min producing optimum measurable values for deposition width, height, aspect ratio, percent dilution, and contact angle of 1.7 mm, 0.7 mm, 2.42, 3.4%, and 74, respectively, were used to produce multi-bead and multilayer depositions. The study opens the avenue for the deployment of PTA deposition for dies and molds repair/remanufacturing.

Zhao et al. (2016), to improve the tribological properties of automobile stamping dies, synthesized Cu-rich particulate composite coatings via PTA alloying of copper on ferritic nodular cast iron substrates. The plasma transferred arc heat input had an important effect on the synthesis of composite coatings. At a low heat input of 202 J/mm, a double-layer structure with both a Cu-rich layer and a Fe-rich layer was observed. As the heat input increased, the volume of the Cu-rich layer significantly decreased because the Cu is further mixed into Fe-rich layer. When the heat input was increased to 260 J/mm, a single Cu-rich particulate composite coating was synthesized in the molten pool. Microstructural analysis revealed that Fe-rich particles were embedded in the Cu-rich matrix, while Cu-rich particles were embedded in the Fe-rich matrix, which consisted predominantly of residual austenite, acicular martensite, and inter-dendritic eutectic

carbides. The microhardness of the Cu-rich particulate composite coatings was measured, which was much higher than that of the untreated substrate material but lower than that of the remolten layer without the Cu additive. Sliding wear tests are carried out on the composite coatings at room temperature (RT) and 773 K. The results exhibited a much better wear resistance of the composite coating compared to the untreated material. The Cu-rich particles contained in the composite coatings played an important role in the antifriction properties, which was attributed to the formation of protective Cu films on the friction surface.

12.6 Summary and Conclusions

Among the global family of surface modification technologies, plasma transferred arc (PTA) coating is closer to plasma arc welding (PAW), metal inert gas (MIG), and tungsten inert gas (TIG) welding than conventional wire arc or DC plasma spraying. One of the unique features of PTA coating is that the substrate is actively serves as one of the arc electrodes, resulting in high heat transfer rates, the local melting of the substrate, and the fusion of the coating material to the substrate. The direct consequence of such a coating route is the formation of a good metallurgical bond of the coating to the substrate, very high coating density, and the possibility to generate thick coatings (up to 10 mm). The major drawback is the limited ability to coat complex shapes, the high level of residual stress, and the requirement of metallurgical compatibility between substrate and coating. There are numerous reports of successful uses of PTA deposited coatings for reducing wear and corrosion and rebuilding metallic components in almost every industry where thick coatings are of advantage. This process has led to a number of developments of new materials combinations in metallurgy and in composites, and it is expected that this trend will continue. In this chapter a review is presented of basic concepts at play in the technology, arc stabilization mechanism, and the importance of the choice of the proper plasma gas and its impact on the coating properties. Following a discussion of basic design features of PTA systems, a review is presented of the effect of process parameter changes on the coating properties. Attention is given to the concept of "dilution" which is a measure of the ratio of the area where the substrate and coating materials are mixed, to the total area in which the coating material appears as defined in Fig. 12.2. Typical rang of operating conditions for three scales of PTA operation are given: micro-PTA, regular PTA, and high-power PTA in Table 12.1 together with the impact of the effect of process parameter values on coating properties, Table 12.2.

Attention is also given to the important area of process modifications and adaptations. In this section a brief discussion is presented on different approaches undertaken in order to expand on the potential use of the technology including such topic as coating nitriding, modulation of deposition parameters, pulsed arc additive manufacturing, high energy PTA, and the operation of PTA in reverse polarity mode. Gas and particle dynamics in PTA coating operations is discussed next providing examples of typical temperatures fields in the arc column and the molten metal pool formed locally in the substrate where the coating material is injected and heat flux to the substrate. Results of process modeling studies are discussed including the relatively important area of the effect of substrate position, horizontal or vertical on the shape of the formed coating bead, and ns of controlling it which is of vital importance for industrial utilization of the technology for coating applications in constrained conditions. Finally, a brief review is presented of coating materials in the range of industrial applications of the technology which mostly in the areas of wear and corrosion protection as well as for the rebuilding of worn-up parts to their original dimensions.

Nomenclature

Units are indicated in parentheses; when no units are indicated, the parameter is dimensionless.

Latin Alphabet

A_{conv} – Area over which the convective heat transfer takes place (m^2)
A – Area where coating material is not mixed with the substrate (m^2)
B – Area where substrate and coating material are mixed (m^2)
c_p – Specific heat at constant pressure (J/kg.K)
d_z – Torch-to-substrate (anode) distance (m)
de – Equivalent diameter of current path (m)
D – Dilution
D – Arc attachment spot diameter (m)
E – Electric field (V/m)
E_i – Ionization potential of the plasma gas (eV)
I – Arc current (A)
I_{arc} – Arc current (A)
I_{pilot} – Pilot arc current (A)
j_e – Electrons current density (A/m^2)
j_i – Ions current density (A/m^2)
k – Constriction parameter (cm^{-2})
k_B – Boltzmann constant (1.38 10^{-23} J/K)
$\dot{m}_p$ – Powder feed rate (kg/s)
$\dot{m}_{gas}$ – Plasma gas feed rate (kg/s)
q_a – Heat flux received by the anode (W/m^2)
q_e – The electron enthalpy flux (W/m^2)
q_m – Maximum heat flux (W/m^2)
$q(r)$ – Substrate heat flux (W/m^2)
Q_{an} – Heat transfer to the anode (W)
Q_{con} – Conduction heat transfer (W)
Q_{sub} – Total heat transfer to the substrate (W)
Q_{melt} – Power involved in melting steel (W)
Q_{oxy} – Power released from iron oxidation (W)
Q_R – The heat transfer by radiation (W/m^2)
r – Distance in the radial direction (m)
r_e – Arc radius (m)

T_e – Electrons temperature (K)
T_h – Heavy species temperature (K)
v – Specific velocity (m/s)
v_{tras} – Substrate translation speed (m/s)
V – Arc voltage (V)
V_{pilot} – *Pilot arc* voltage (V)
z – Distance in the axial direction (m)

Greek Alphabet

α – Fraction of the electrical power transferred to the anode by convection and radiation
δ – Melted layer thickness (m)
Φ_a – The work function of the anode material (eV)
κ – Thermal conductivity (W/m K)
ρ – Mass density (kg/m^3)
$\overline{\sigma_{ac}}$ – eEectrical conductivity of argon averaged over the arc cross section (A/V.m)
Δz – Distances between the cathode tip and the anode (m)

References

Alberti, E.A., B.M.P. Bueno, and A.S.C.M. D'Oliveira. 2016. Additive manufacturing using plasma transferred arc. *International Journal of Advanced Manufacturing Technology* 83: 1861–1871.

Bach, F.-W., and J. Zühlsdorf. 1999. Plasma powder welding under raised pressure environment, Proc. UTSC., Düsseldorf, Germany, 1999, eds. E. Lugscheider and P. Kammer (Pub.) DVS, Düsseldorf, Germany, pp 757–760.

Bini, R., M. Monno, and M.I. Boulos. 2007. Effect of cathode nozzle geometry and process parameters on the energy distribution for an argon transferred arc. *Plasma Chemistry and Plasma Processing* 27: 359–380.

Bhargava, P., C.P. Paul, C.H. Premsingh, S.K. Mishra, Atul Kumar, D. C. Nagpure, G. Singh, and L.M. Kukreja. 2013. Tandem rapid manufacturing of Inconel-625 using laser assisted and plasma transferred arc depositions. *Advanced Manufacturing* 1: 305–313.

Bouaifi, B., A. Gebert, and H. Heinze. 1993. Plasma-Pulver-Auftragschweiβungen zum Verschleiβschutz abrasiv beanspruchter Bauteile mit Kantenbelastung. *Schweissen und Schneiden* 45: 506–509.

Bouaifi, B., F. Schreiber, J. Göllner, and S. Schulze. 1996. Eigenschaften und Beständigkeit von Plasma-Pulver-Auftragschweißungen aus hartstoffverstärkten. *CrNiMoN-legierten Duplex-Stählen in DVS-Berichte* 175: 425–428.

Bouaifi, B., A. Ait-Mekideche, A. Gebert, and D. Wocilka. 2001. Nutzung von stickstoffhaltigen Hochtemperaturplasmen zum reaktiven beschichten mittels Plasmaauftragschweiβen. *Schweissen und Schneiden* 53: 478–482.

Bourithis, L., S. Papaefthymiou, and G.D. Papadimitriou. 2002. Plasma transferred arc boriding of a low carbon steel: Microstructure and wear properties. *Applied Surface Science* 200: 203–218.

Camélia, Demian, Alain Denoirjean, Lech Pawłowski, Paule Denoirjean, and Rachida El Ouardi. 2016. Microstructural investigations of NiCrAlY + Y_2O_3 stabilized ZrO_2 cermet coatings deposited by plasma transferred arc (PTA). *Surface & Coatings Technology* 300: 104–109.

Colombo, V., A. Concetti, E. Ghedini, and S. Dallavalle. 2011. Design oriented simulation for plasma arc cutting consumables and experimental validation of results. *Plasma Sources Science and Technology* 20: 035010 (10pp).

Davis, J.R., ed. 2004. *Handbook of thermal spray technology*. Materials Park: ASM international.

Deuis, R.L., J.V. Bee, and C. Subramanian. 1997a. Investigation of interfacial structures of plasma transferred arc deposited Aluminum based composites by transmission Electron microscopy. *Scripta Materialia* 31 (6): 721–727.

Deuis, R.L., J.M. Yellup, and C. Subramanian. 1998. Metal-matrix composite coatings by PTA surfacing. *Composites Science and Technology* 58: 299–309.

Dilthey, U., J. Ellermeier, P. Gladkij, and A.V. Pavlenko. 1993. Kombiniertes Plasma-Pulver-Auftragschweissen. *Schweissen und Schneiden* 45 (5): 241–244.

Dilthey, U., L. Kabatnik, E. Lugscheider, K. Schlimbach, and G. Langer. 1999. Möglichkeiten zur Steigerung der Oberflächenfestigkeit bei Aluminiumlegierungen mit Plasma-Pulver-Schweiβverfahren (Improving of the Wear Resistance of Aluminum Alloys by Plasma Transferred Arc Welding). *Mat.-wiss. u. Werkstofttech* 30 (11): 697–702.

Dilthey, U., S. Kondapalli, B. Balashow, and F. Riedel. 2008. Improving wear resistance of aluminium alloys by developing FTC and TiC based composite coatings using plasma powered arc welding process. *Surface Engineering* 24 (1): 75–80.

D'Oliveira, C.M., R.S. Paredes, and R.L. Santos. 2005. Pulsed current plasma transferred arc hardfacing. *Materials Processing Technology* 171: 167–174.

Ducos, M. 1985. Applications industrielles des plasmas d'arc de faible puissance et des plasmas inductifs, Rechargement par plasma à arc transferré, in Les Plasmas dans l'industrie, (Pub.). Dopée/85, EDF France (in French).

DuMola, R.J., and G. R. Heath. 1997. New Developments in the Plasma Transferred Arc Process, Proc. UTSC-1997, Indianapolis, IN, (ed.) C. C. Berndt (Pub.) ASM International, Materials Park, OH, pp 427–434.

DuPont, J.N. 1998. On optimization of the powder plasma arc surfacing process. *Metallugical and Materials Transactions, B* 29B: 932–934.

Ebert, L., S. Thurner, and S. Neyka. 2009. Beeinflussung der Hartstoffverteilung beim Plasma-Pulver-Auftragschweiβen, Influencing the distribution of reinforcing particles in plasma transfer arc welding. *Mat.-wiss u. Werkstofttech* 40 (12): 878–881.

Eddie, P. 2011. *Plasma cutting handbook*, (Pub.) HP books 1569 Penguin group, NY

Eliot, D. 1991. Technologie et spécificité du découpage par plasma dans "les plasmas dans l'industrie" (Pub.) Dopée Avon, France, 229–241 (in French).

Etemadi, K. 1982. Investigation of high-current arcs by computer-controlled plasma spectroscopy, PhD Thesis, University of Minnesota, Mn, USA

Evrard, M., and B. Blanchet. 1970. Etudes des plasmas d'arc du point de vue du soudage. *Soudages et Techniques Connexes* 7: 261–298. (in French).

Fisher, G., T. Wolfe, and K. Meszaros. 2013. The effects of carbide characteristics on the performance of tungsten carbide-based composite overlays, deposited by plasma-transferred arc welding. *Journal of Thermal Spray Technology* 22 (5): 764–771.

Flores, J.F., A. Neville, N. Kapur, and A. Gnanavelu. 2009a. An experimental study of the erosion–corrosion behavior of plasma transferred arc MMCs. *Wear* 267: 213–222.

———. 2009b. Erosion–corrosion degradation mechanisms of Fe–Cr–C and WC–Fe–Cr–C PTA overlays in concentrated slurries. *Wear* 267: 1811–1820.

Freton, P., J.J. Gonzalez, F. Camy Peyret, and A. Gleizes. 2003. Complementary experimental and theoretical approaches to the determination of the plasma characteristics in a cutting plasma torch. *Journal of Physics D: Applied Physics* 36: 1269–1283.

Gallo, S.C., N. Alam, and R. O'Donnell. 2013. In-situ synthesis of titanium carbides in iron alloys using plasma transferred arc welding. *Surface & Coatings Technology* 225: 79–84.

Gallo, S., C.N. Alam, and R.O. Donnell. 2014. In situ synthesis of TiC-Fe composite overlays from low cost TiO2 precursors using plasma transferred arc deposition. *Journal of Thermal Spray Technology* 23 (3): 551–556.

Gatto, A., E. Bassoli, and M. Fornari. 2004. Plasma transferred arc deposition of powdered high-performance alloys: Process parameters optimization as a function of alloy and geometrical configuration. *Surface & Coatings Technology* 187: 265–271.

Gebert, A., and B. Bouaifi. 2005. *Oberflächenschutz durch Auftragschweißen*, Moderne Beschichtungsverfahren. Wiley

Gebert, A., D. Wocilka, B. Bouaifi, and M. Schütz. 2002. Wear and corrosion prevention at light metals by means of welding methods, Proc. ITSC-2002, Essen, Germany, ed. E. Lugscheider (Pub.) DVS, Düsseldorf, Germany, pp 268–272.

Guoqing, R., M. Monno, and M.I. Boulos. 2007. Effect of cathode nozzle geometry and process parameters on the energy distribution for an argon transferred arc. *Plasma Chemistry and Plasma Processing* 27: 359–380

Guoqing, C., F. Xuesong, W. Yanhui, L. Shan, and Z. Wenlong. 2013. Microstructure and wear properties of nickel-based surfacing deposited by plasma transferred arc welding. *Surface & Coatings Technology* 228: S276–S282.

Hallen, H., E. Lugscheider, and A. Ait-Mekideche. 1991. Plasma Transferred Arc Surfacing with High Deposition Rates, Proc. of the 4th. NTSC-1991, Pittsburgh, PA, ed. T. Bernecki (Pub.) ASM International, Materials Park, OH, pp 537–539.

Hallen, H., H. Mathesius, A. Ait-Mekideche, F. Hettiger, U. Morkramer, and E. Lugscheider. 1992. New Applications for High Power PTA Surfacing in the Steel Industry, Proc. ITSC-1992 Orlando, Florida, ed. C. C. Berndt (Pub.) ASM International, Materials Park, OH, pp 899–902.

Hawthorne, H.M., B. Arsenault, J.P. Immarigeon, J.G. Legoux, and V. R. Parameswaran. 1999. Comparison of slurry and dry erosion behavior of some HVOF thermal sprayed coatings. *Wear* 225–229: 825–834.

Heberlein, J., J. Mentel, and E. Pfender. 2007. The anode region of electric arcs – A survey. *Journal of Physics D: Applied Physics* 43: 023001.

Heberlein, J. 2007. Observations on thermionic cathode erosion, 1st Inter. Round Table on Thermal Plasmas (Sharm El Sheikh, Egypt, January 2007).

Hou, Q.Y., J.S. Gao, and F. Zhou. 2005. Microstructure and wear characteristics of cobalt-based alloy deposited by plasma transferred arc weld surfacing. *Surface & Coatings Technology* 194: 238–243.

———. 2006. Microstructure and properties of Fe–C–Cr–Cu coating deposited by plasma transferred arc process. *Surface & Coatings Technology* 201: 3685–3690.

Hou, Q.Y., Y.Z. He, Q.A. Zhang, and J.S. Gao. 2007. Influence of molybdenum on the microstructure and wear resistance of nickel-based alloy coating obtained by plasma transferred arc process. *Materials and Design* 28: 1982–1987.

Hou, Q.Y., Z. Huang, and J.T. Wang. 2011. Influence of nano-Al2O3 particles on the microstructure and wear resistance of the nickel-based alloy coating deposited by plasma transferred arc overlay welding. *Surface & Coatings Technology* 205: 2806–2812.

Hou, Q.Y., L.M. Luo, Z.Y. Huang, P. Wang, T.T. Ding, and Y.C. Wu. 2015a. Comparison of three kinds of MC-type carbide modified thick W coatings fabricated by plasma transferred arc surfacing. *Surface & Coatings Technology* 283: 52–60.

Hou, Q.Y., T.T. Ding, Z.Y. Huang, P. Wang, L.M. Luo, and Y.C. Wu. 2015b. Microstructure and properties of mixed Cu–Sn and Fe-based alloys without or with molybdenum addition processed by plasma transferred arc. *Surface & Coatings Technology* 283: 184–193.

Hou, Q.Y. 2013a. Influence of molybdenum on the microstructure and properties of a FeCrBSi alloy coating deposited by plasma transferred arc hardfacing. *Surface & Coatings Technology* 225: 11–20.

———. 2013b. Microstructure and wear resistance of steel matrix composite coating reinforced by multiple ceramic particulates using SHS reaction of Al–TiO2–B2O3 system during plasma transferred arc overlay welding. *Surface & Coatings Technology* 226: 113–122.

Hsu, K.C., K. Etemadi, and E. Pfender. 1983. Study of the free-burning high-intensity argon arc. *Journal of Applied Physics* 54 (3): 1293–1301.

Hung, F.-Y., Z.-Y. Yan, L.-H. Chen, and T.-S. Lui. 2006. Microstructural characteristics of PTA-overlayed NbC on pure Ti. *Surface & Coatings Technology* 200: 6881–6887.

Huang Zhenyi , Qingyu Hou, Ping Wang (2008) Microstructure and properties of Cr3C2-modified nickel-based alloy coating deposited by plasma transferred arc process, Surface & Coatings Technology, 202, 2993-2999

Jenista, J., J. Heberlein, and E. Pfender. 1997. Numerical model of the anode region of high-current electric arcs. *IEEE Transactions on Plasma Science* 25 (5): 883–890.

Jenista, J., J. Heberlein, and E. Pfender. 1997a. Model for anode heat transfer from an electric arc, Proc. 4th Inter. Thermal Plasma Processes Conference, Athens, Greece, 1997, ed. P. Fauchais Begell House Inc., New York, NY, pp 805–815.

———. 1997b. Numerical model of the anode region of high-current electric arcs. *IEEE Transactions on Plasma Science* 25 (5): 883–890.

Jhavar, S., N.K. Jain, and C.P. Pau. 2014. Development of micro-plasma transferred arc (PTA) wire deposition process for additive layer manufacturing applications. *Journal of Materials Processing Technology* 214: 1102–1110.

Jhavar, S., C.P. Paul, and N.K. Jain. 2016. Micro-plasma transferred arc additive manufacturing for die and Mold surface remanufacturing. *JOM* 68 (7): 1801–1809.

Just, C., E. Badisch, and J. Wosik. 2010. Influence of welding current on carbide/matrix interface properties in MMCs. *Journal of Materials Processing Technology* 210: 408–414.

Kammer, P.A., M. Weinstein, and R. J. DuMola. 1991. Characteristics and applications for composite wear-resistant overlays, Proc. 4th. NTSC-1991, Pittsburgh, PA, ed. T. Bernecki (Pub.) ASM International, Materials Park, OH, pp 513–518.

Karanunakarani, N., and V. Balasubramanian. 2011. Effect of pulsed current on temperature distribution, weld bead profiles and characteristics of gas tungsten arc welded aluminum alloy joints. *Transactions of the Nonferrous Metals Society of China* 21: 278–286.

Kavka, T., O. Chumak, J. Sonsky, M. Heinrich, T. Stehrer, and H. Pauser. 2013. Experimental study of anode processes in plasma arc cutting. *Journal of Physics D: Applied Physics* 46 (2013): 065202 (11pp).

Kim, H.-J., B.-H. Yoon, and C.-H. Lee. 2002. Wear performance of the Fe-based alloy coatings produced by plasma transferred arc weld-surfacing process. *Wear* 249 (2002): 846–852.

———. 2003. Sliding wear performance in molten Zn–Al bath of cobalt-based over-layers produced by plasma-transferred arc weld-surfacing. *Wear* 254: 408–414.

lakovou, R., L. Bourithis, and G. Papadimitriou. 2002. Synthesis of boride coatings on steel using plasma transferred arc (PTA) process and its wear performance. *Wear* 252: 1007–1015.

Lakshminarayanan, A.K., V. Balasubramanian, R. Varahamoorthy, and S. Babu. 2008. Predicting the dilution of plasma transferred arc hardfacing of stellite on carbon steel using response surface methodology. *Metals and Materials International* 14 (6): 779–789.

Lewis, G.K., and E. Schlienger. 2000. Practical considerations and capabilities for laser assisted direct metal deposition. *Materials & Design* 21 (4): 417–423.

Leylavergne, M., H. Valetoux, J. F. Coudert, P. Fauchais, and V. Leroux. 1998. Comparison of the behaviour of copper, cast iron and aluminum alloy substrates heated by a plasma transferred arc,

in Proc. 15th ITSC-1998, Nice, France, ed. C. Coddet (Pub.) ASM International, Materials Park, OH, pp 489–495.

Li, G., C. Zhang, M. Gao, and X. Zeng. 2014. Role of arc mode in laser-metal active gas arc hybrid welding of mild steel. *Materials and Design* 61: 239–250.

Lin, J.J., Y.H. Lv, Y.X. Liu, B.S. Xu, Z. Sun, Z.G. Li, and Y.X. Wu. 2016. Microstructural evolution and mechanical properties of Ti-6Al-4V wall deposited by pulsed plasma arc additive manufacturing. *Materials and Design* 102: 30–40.

Liu, Y.-F., Z.-Y. Xia, J.-M. Han, G.-L. Zhang, and S.-Z. Yang. 2006. Microstructure and wear behavior of (Cr,Fe)7C3 reinforced composite coating produced by plasma transferred arc weld-surfacing process. *Surface & Coatings Technology* 201: 863–867.

Liu, Y.-F., X.-B. Liu, X.-Y. Xu, and S.-Z. Yang. 2007. Microstructure and dry sliding wear behavior of Fe2TiSi /γ-Fe/Ti5Si3 composite coating fabricated by plasma transferred arc cladding process. *Surface & Coatings Technology* 205: 814–819.

Lu, F., H. Li, Q. Ji, R. Zeng, S. Wang, J. Chi, M. Li, L. Chai, and H. Xu. 2011. Characteristics of the functionally graded coating fabricated by plasma transferred arc centrifugal cladding. *Surface & Coatings Technology* 205: 4441–4446.

Lü, Y.-H., Y.-X. Liu, F.-J. Xu, and B.-S. Xu. 2013. Plasma transferred arc forming technology for remanufacture. *Advanced Manufacturing* 1: 187–190.

Lindland, D., and G. Shubert. 1988. Method for applying a weld bead to a thin section of a substrate. *US Patent*: 4,739,146.

Lowke, J.J., R. Morrow, and J. Haidar. 1997. A simplified unified theory of arcs and their electrodes. *Journal of Physics D: Applied Physics* 30: 2033–2042.

Lowke, J.J., M. Tanaka, and M. Ushio. 2005. Mechanisms giving increased weld depth due to a flux. *Journal of Physics D: Applied Physics* 38 (18): 3438–3445.

Lugscheider, E., and A. Ait-Mekideche. 1991. Advances in PTA surfacing. In *Proceedings of the fourth thermal spray conference Pittsburgh, PA*, ed. C.C. Berndt, 529–535. Materials Park: ASM International.

Lugscheider, E., G. Langer, K. Schlimbach, U. Dilthey, and L. Kabatnik. 1999. Possibilites for improving wear-properties of Aluminum-alloys by plasma powder welding process. In *Proceedings of the UTSC, Düsseldorf, Germany*, ed. E. Lugscheider and P. Kammer, 410–413. Düsseldorf: DVS.

Matthes, K.-J., and K. Alaluss. 1996. Formgebendes Plasma-Pulverauftragschweissen mit Impulslichtbogen unter Beachtung minimaler Verformung. *Schweissen und Schneiden* 48 (9): 668–672.

Matthes, K.-J., K. Alaluss, and F. Riedel. 2002. Nutzung der Finite-Elemente-Methode zur Optimierung des formgebenden Pulver-Plasmaauftragschweissens für die Herstellung hoch beanspruchbarer Umformwerkzeuge. *Schweissen und Schneiden* 54 (4): 178–184.

Menart, J. A. 1996. Theoretical and experimental investigations of radiative and total heat transfer in thermal plasmas, Ph.D. Thesis, University of Minnesota, Mn, USA

Morisada, Y.I., H. Fujii, and N. Xukun. 2014. Development of simplified active flux tungsten inert gas welding for deep penetration. *Materials and Design* 54: 526–530.

Murphy, A.B., M. Tanaka, S. Tashiro, T. Sato, and J.J. Lowke. 2009. A computational investigation of the effectiveness of different shielding gas mixtures for arc welding. *Journal of Physics D: Applied Physics* 42: 115205(14pp).

Murphy, A.B. 2010. The effects of metal vapor in arc welding. *Journal of Physics D: Applied Physics* 43: 434001(31pp).

Murphy, A.B., M. Tanaka, K. Yamamoto, S. Tashiro, J.J. Lowke, and K. Ostrikov. 2010. Modelling of arc welding: The importance of including the arc plasma in the computational domain. *Vacuum* 85: 579–584.

Nemchinsky, V.A., and M.S. Showalter. 2003. Cathode erosion rate in high-pressure arcs influence of swirling gas flow. *Journal of Physics D: Applied Physics* 36: 704–712.

Nemchinsky, V.A. 2005. Anode layer in a high-current arc in atmospheric pressure nitrogen. *Journal of Physics D: Applied Physics* 38 (2005): 4082–4089.

Nemchinsky, V.A., and W.S. Severance. 2006. What we know and what we do not know about plasma arc cutting. *Journal of Physics D: Applied Physics* 39: R423–R438.

Nemchinsky, V. 2012. Cathode erosion in a high-pressure high-current arc: Calculations for tungsten cathode in a free-burning argon arc. *Journal of Physics D: Applied Physics* 45: 135201(8pp).

Nestor, O.H. 1962. Heat intensity and current density distributions at the anode of high current, inert gas arcs. *Journal of Applied Physics* 33 (5): 1638–1648.

d'Oliveira, A.S.C.M., R. Vilar, and C.G. Feder. 2002. High temperature behavior of plasma transferred arc and laser co-based alloy coatings. *Applied Surface Science* 201: 154–160.

d'Oliveira, A.S.C.M., R.S.C. Paredes, and R.L.C. Santos. 2006. Pulsed current plasma transferred arc hard-facing. *Journal of Materials Processing Technology* 171: 167–174.

Ozel, S., B. Kurt, I. Somunkiran, and N. Orhan. 2008. Microstructural characteristic of NiTi coating on stainless steel by plasma transferred arc process. *Surface & Coatings Technology* 202: 3633–3637.

Peters, J., J. Heberlein, and J. Lindsay. 2007. *S*pectroscopic diagnostics in a highly constricted oxygen arc. *Journal of Physics D: Applied Physics* 40: 3960–3971.

Proner, A., J.P. Dacquet, and R. Rouanet. 1997a. In *The plasma high energy: A new hardfacing technique*, ed. P. Fauchais, 787–794. New York: Begell House, Inc.

Proner, A., M. Ducos, and J.P. Dacquet. 1997b. Process for coating of hardfacing a part by means of a plasma tranferred arc. *US Patent US*: 5,624,717.

Pukasiewicz, A.G.M., P.R.C. Alcover Jr., A.R. Capra, and R.S.C. Paredes. 2014. Influence of plasma Remelting on the microstructure and cavitation resistance of arc-sprayed Fe-Mn-Cr-Si alloy. *Journal of Thermal Spray Technology* 23 (1–2): 51–59.

Razal, Rose A., K. Manisekar, V. Balasubramanian, and S. Rajakumar. 2012. Prediction and optimization of pulsed current tungsten inert gas welding parameters to attain maximum tensile strength in AZ61A magnesium alloy. *Materials and Design* 37 (2012): 334–348.

Reinaldo, P.R., and A.S.C.M. D'Oliveira. 2013. Coatings deposited by plasma transferred arc on different steel substrates. *Journal of Materials Engineering and Performance* 22 (2): 590–597.

Rokanopoulou, A., P. Skarvelis, and G.D. Papadimitriou. 2014. Microstructure and wear properties of the surface of 2205 duplex stainless steel reinforced with Al2O3 particles by the plasma transferred arc technique. *Surface & Coatings Technology* 254: 376–381.

———. 2016. Improvement of the tribological properties of Al_2O_3 reinforced duplex stainless steel MMC coating by the addition of TiS2 powder. *Surface & Coatings Technology* 289: 144–149.

Saltzmann G.A., T.A. Wertz, and I.L. Friedman. 1989. Method for refurbishing cast gas turbine engine components and refurbished component, US Patent 4,878,953.

Saltzman, G., and P. Sahoo. 1991. Applications of Plasma Arc Weld Surfacing in Turbine Engines, Proc. Proceedings of the Fourth National Thermal Spray Conference, Pittsburgh, PA, 1991 (ed.) C. C. Berndt (Pub.) ASM International, Materials Park, OH, pp 541–548

Santa, J.F., L.A. Espitia, J.A. Blanco, S.A. Romo, and A. Toro. 2009. Slurry and cavitation erosion resistance of thermal spray coatings. *Wear* 267: 160–167.

Schnick, M., U. Füssel, M. Hertel, A. Spille-Kohoff, and A.B. Murphy. 2010. Metal vapour causes a central minimum in arc temperature in gas–metal arc welding through increased radiative emission. *Journal of Physics D: Applied Physics* 43: 022001(5pp).

Schreiber, F., and D. Krefeld. 2002. Mobile plasma powder hand deposition welding: practice experience, Proc. Intern. Thermal Spray

Conference 2002, Essen, Germany, 4–6 March, 2002, ed. E. Lugscheider (Pub.) DVS, Düsseldorf, Germany, pp 273–277

Shi, K., S. Hu, and H. Zheng. 2011. Microstructure and fatigue properties of plasma transferred arc alloying TiC-W-Cr on gray cast iron. *Surface & Coatings Technology* 206: 1211–1217.

Shi, K., S. Hu, and L. Liang. 2012. Effect of tempering treatment on microstructure and fatigue life of TiC–Cr overlay, produced by plasma transferred arc alloying. *Journal of Materials Science* 47: 720–729.

Sigolo, E., J. Soyama, G. Zepon, C.S. Kiminami, W.J. Botta, and C. Bolfarini. 2016. Wear resistant coatings of boron-modified stainless steels deposited by plasma transferred arc. *Surface & Coatings Technology* 302: 255–264.

Shubert, G.C. 1987. Welding apparatus method for depositing wear surfacing material and a substrate having a weld bead thereon. *US Patent*: 4,689,463.

Skarvelis, P., and G.D. Papadimitriou. 2009. Plasma transferred arc composite coatings with self -lubricating properties, based on Fe and Ti sulfides: Microstructure and tribological behavior. *Surface & Coatings Technology* 203: 1384–11394.

Sung, J.K. 2009. Fluid dynamic instabilities in plasma arc cutting, (Pub.) University of Minnesota, 127 pages

Tanaka, M., and J.J. Lowke. 2007. Topical review, predictions of weld pool profiles using plasma physics. *Journal of Physics D: Applied Physics* 40: R1–R23.

Tashiro, S., T. Zeniya, K. Yamamoto, M. Tanaka, K. Nakata, A.B. Murphy, E. Yamamoto, K. Yamazaki, and K. Suzuki. 2010. Numerical analysis of fume formation mechanism in arc welding. *Journal of Physics D: Applied Physics* 43: 434012(12pp).

Tigrinho, J.J., A. Sofia, and C.M. d'Oliveira. 2007. Plasma transferred arc surface modification of a low carbon steel. *Journal of Materials Science* 42 (17): 7554–7557.

Toropchin, A., V. Frolov, A.V. Pipa, R. Kozakov, and D. Uhrlandt. 2014. Influence of the arc plasma parameters on the weld pool profile in TIG welding. *Journal of Physics: Conference Series* 550: 012004.

Tucker, R.C., Jr., ed. 2013. *ASM handbook Vol. 5A thermal spray technology*. Materials Park: ASM international.

Valetoux, H. 1998. Experimental approach of the phenomena implied in transferred arc plasma cutting. Contribution to the study of instabilities and thermal transfer, (in French) Ph.D. Thesis, University of Limoges, France.

Werry, A., C. Chazelas, A. Denoirjean, S. Valette, A. Vardelle, and E. Meillot. 2016. Multi-scale-structured composite coatings by plasma-transferred arc for nuclear applications. *Journal of Thermal Spray Technology* 25 (1–2): 375–383.

Wang, H., W. Jiang, M. Valant, and R. Kovacevic. 2003. Microplasma powder deposition as a new solid freeform fabrication process. *Proceedings of the Institution of Mechanical Engineers, Part B: Journal of Engineering Manufacture* 217: 1641–1650.

Wang, W., S.Q. Qian, and X.Y. Zhou. 2009. Microstructure and properties of TiN/Ni composite coating prepared by plasma transferred arc scanning process. *Transactions of the Nonferrous Metals Society of China* 19: 1180–1184.

Wassermann, R., J. Quaas, J.-C. Chalard, L. Noel, and H.-T. Steine. 1978. Installation for surfacing using plasma-arc welding. *US Patent*: 4,125,754.

Wilden, J., J. P. Bergmann, H. Frank, S. Pinzl, and F. Schrieber. 2004. Thin plasma-transferred-arc welded coatings – An alternative to thermally sprayed coatings? Proc. ITSC-2004, Osaka, Japan, ed. A. Ohmori (Pub.) ASM International, Materials Park, OH, pp 556–561.

Wilden, J., J.P. Bergmann, and H. Frank. 2006. Plasma transferred arc welding-modeling and experimental optimization. *Journal of Thermal Spray Technology* 15 (4): 779–784.

Wu, C.S., L. Wang, W.J. Ren, and X.Y. Zhang. 2014. Plasma arc welding: Process, sensing, control and modeling. *Journal of Manufacturing Processes* 16: 74–85.

Yamamoto, K., M. Tanaka, S. Tashiro, K. Nakata, K. Yamazaki, E. Yamamoto, K. Suzuki, and A.B. Murphy. 2008. Metal vapor behavior in thermal plasma of gas tungsten arcs during welding. *Science and Technology of Welding and Joining* 13: 566–572.

Yang, G., and J. Heberlein. 2008. Anode heat transfer by electron current and electron conduction in an atmospheric pressure argon arc. Proc. Intern. Conf. Electrical Contacts, Saint Malo, France, 2008, ed. N. B. Jemmaa (Pub.) Universite de Rennes, France pp 313–316.

Yang, G., and J. Heberlein. 2008. Anode heat transfer by electron current and electron conduction in an atmospheric pressure argon arc. In *Proceedings of the international conference on electrical contacts, Saint Malo, France*, ed. N.B. Jemmaa, 313–316. Rennes: Universite de Rennes.

Young, R.M, Y. P. Chyou, E. Fleck, and E. Pfender. 1983. An experimental arc plasma reactor for the synthesis of refractory materials, Proc. ISPC-6, Montreal, Quebec, 1983, eds. M. I. Boulos and R. J. Munz (Pub.) IUPAC, pp 211–218

Yuan, Y., and Z. Li. 2014. Microstructure and wear performance of high-volume fraction carbide M_7C_3 reinforced Fe-based composite coating fabricated by plasma transferred arc welding. *Journal of Wuhan University of Technology. Materials Science Edition* 29 (5): 1028–1035.

Zhao, W., and L. Liu. 2006. Structural characterization of Ni-based superalloy manufactured by plasma transferred arc-assisted deposition. *Surface & Coatings Technology* 201: 1783–1787.

Zhao, H., J. Li, Z. Zheng, A. Wang, D. Zeng, and Y. Miao. 2016. The microstructures and tribological properties of composite coatings formed via PTA surface alloying of copper on nodular cast iron. *Surface & Coatings Technology* 286: 303–312.

Zhenyi, Huang, Qingyu Hou, and Ping Wang. 2008. Microstructure and properties of Cr_3C_2-modified nickel-based alloy coating deposited by plasma transferred arc process. *Surface & Coatings Technology* 202: 2993–2999.